ARGON-OXYGEN DECARBURIZATION OF HIGH MANGANESE STEELS

ARGON-OXYGEN DECARBURIZATION OF HIGH MANGANESE STEELS

By

ALIYEH RAFIEI, B.SC., M.SC.

A Thesis

Submitted to the School of Graduate Studies

in Partial Fulfillment of the Requirements

for the Degree

Doctor of Philosophy

McMaster University

DOCTOR OF PHILOSOPHY (2021) McMaster University

(Materials Engineering) Hamilton, Ontario

Title: Argon-Oxygen Decarburization of High Manganese Steels

Author: Aliyeh Rafiei, M.Sc. (Sharif University of Technology)

Supervisors: Professor Kenneth S. Coley & Professor Gordon A. Irons

Number of pages: XVII-190

Abstract

Manganese is an essential alloying element in the 2nd and 3rd generation of Advanced High Strength steels (AHSS) containing 5 to 25% manganese. A combination of excellent strength and ductility makes these grades of steel attractive for the automotive industry. To produce these steels to meet metallurgical requirements the main concern for the steelmakers is to decrease the carbon concentration as low as 0.1% while suppressing the excessive manganese losses at high temperatures. Argon Oxygen Decarburization (AOD) is a promising candidate for the refining of high manganese steels.

This work has studied the kinetics of decarburization and manganese losses during the argon oxygen bubbling into a wide range of iron-manganese-carbon alloys. It was shown that decreasing the initial carbon content increased the manganese loss. In the competition between manganese and carbon for oxygen, alloys with lower initial manganese concentrations consumed a higher portion of oxygen for decarburization. This behavior was not expected by thermodynamics and the results did not support the concept of the critical carbon content either. It was demonstrated that for lower range carbon ($\leq 0.42\%$) alloys, the total manganese loss can be explained by considering multiple mechanisms in parallel; oxide formation (MnO) and vapor formation (Mn (g)), and formation of Manganese mist by evaporation-condensation (Mn (l)). The evaporation-condensation mechanism was proposed with the assumption that the heat generated from MnO and CO formation increases the temperature at the surface of the bubble which facilitates the

evaporation of manganese at a high vapor pressure. Consequently, manganese vapor condenses as fine droplets at the lower temperature inside the bubble.

Although dilution of oxygen with argon increased the efficiency of oxygen for decarburization as expected from the mechanism of the AOD process, manganese loss did not stop completely at higher argon concentrations in the gas mixture. Therefore, the bubble and melt do not fully equilibrate with respect to Mn and C.

For high carbon alloys (1%), there was excess oxygen after accounting for CO and MnO formation. According to mass balance and thermodynamic calculations, and assuming manganese loss by evaporation was negligible it was shown that oxygen was distributed amongst MnO, FeO, CO, and CO_2.

It was demonstrated that increasing temperature resulted in the higher manganese loss as a mist and by simple evaporation due to the increased vapor pressure and less manganese loss by oxidation. Furthermore, it was found that the rate of decarburization increased with increasing temperature due to more partitioning of oxygen to carbon than manganese.

In addition, it was found that the variations of depth of lance submergence did not affect the rate of decarburization or manganese loss. This means that the reactions occur within such a short time that prolonged time after the reaction is completed does not lead to a repartitioning of the species.

This thesis is lovingly dedicated to my mother.

Acknowledgments

I have had the privilege to study under the supervision of Dr. Ken Coley, and Dr. Gordon Irons for the past six years. I would like to express my sincere gratitude to them for their continuous support, patience, and guidance through my Ph.D. Special thanks to Dr. Coley for being a great leader rather than a boss and for all I have learned from him. He was prepared to sit and listen to my problems and always made me feel as my work is unique and interesting. His willingness to offer me so much of his time and knowledge is the major reason this thesis was completed. I would like to take this opportunity to thank Dr. Irons. The completion of this thesis would not have been possible without his insights, knowledge, and encouragement. In difficult days of my experimental work, I remind myself what he told me in one of our meetings: “Tell yourself you are young and smart, and you can do it!”.

I would like to thank Dr. Neslihan Dogan as a member of my supervisory committee for her helpfulness and kind supports. Thanks go to Dr. Tony Petric for his time for useful discussions in thermodynamics and FactSage.

I would like to thank McMaster Steel Research Centre, and its industrial partners, and Natural Sciences Engineering Research Council, and McMaster University for the financial support.

I wish to thank the Department of Materials Science and Engineering for providing a cooperative academic environment. Special thanks to Xiaogang Li, Doug Culley, and Ed McCaffery for the technical assistance at the Materials Science and Engineering

laboratories. I would like to thank the administrative team at the Department of Materials Science and Engineering, McMaster University. I wish to express my appreciation to Mary-Anne Bechamp for her constant support.

I was very fortunate to work with amazing people in the McMaster Process Metallurgy group throughout my Ph.D. journey. I am extremely thankful to Dr. Kezhuan Gu and Dr. Brian Jamieson for their help to set up the furnace and solve its problems whenever it was needed. I would like to thank Dr. Yousef Tabatabaei for lots of valuable discussions in kinetics and thermodynamics. Thanks to Michelia Alba and Dr. Mukesh Sharma for their friendship and support during these years. Thanks to Dr. Ameya Kadlokar, Dr. Muhammad Nabeel, Keyan Miao, Jayasree Biswas, Mohammed Karodia, Angshuman Podder for their support.

Last but not least, I would like to thank my parents and my sister Atefeh for their endless support and love that have sustained me throughout my life. Thank you for always believing in me and pushing me to try harder. Finally, thanks to God for providing me the opportunity to step into the excellent world of science and accomplish this thesis.

Table of Contents

List of Figures

List of Tables

Abbreviations and Symbols

AOD	Argon oxygen decarburization
BOF	Basic oxygen furnace
EAF	Electric arc furnace
MOR	Manganese Oxygen refining
A	Surface area of gas bubble (cm^2)
a	Raoultian activity
C	Mole concentration (mol/cm^3)
C_p	Molar heat capacity of steel at constant pressure (J/Kmol)
D_i	Diffusion coefficient of species i in liquid phase (cm^2/s)
D_{i-j}	Interdiffusivity of species i and j in gas phase (cm^2/s)
J_i	Flux of transported species (mol/cm^2s)
K	Reaction equilibrium constant
k_i	Mass transfer coefficient of species i (cm/s)
M_i	Molar mass of species i (g/mol)
n_i	Number of moles of species i (mol)
P	Total pressure in bubble (atm)
p_i	Partial pressure of species i in gas phase (atm)
Q	Gas flow rate (Nml/min)
R	Gas constant (cm^3atm/Kmol)
T	Temperature (K)

W	Weight of steel
[wt% i]	Concentration, in mass percent, of species in liquid phase
X_i	Mole fraction of species i
β	Vaporization coefficient
$\eta_{O_2}^{dec}$	Efficiency of oxygen for decarburization (%)
δ	Thickness of the gas-phase diffusion layer (cm)
γ	Raoultian activity coefficient

Chapter 1

1 Introduction

1.1 Research Background

Manganese is an essential constituent of Advanced High Strength Steels (AHSS). Twinning-Induced Plasticity (TWIP) and Transformation-induced plasticity (TRIP) steels contain 4-30% manganese which is remarkably higher than manganese content in the commercial grades [1–3]. There has been an increasing interest in the development of the third generation of AHSS with improved strength and ductility properties compared to the first generation AHSS, while lowering the production cost compared to the second generation AHSS with less manganese concentration in the range of 4-10% [4,5]. These unique features make 3rd generation AHSS attractive for a wide range of applications in the automotive and structural sectors. [6,7] In particular, 3rd generation AHSS are of great importance for the automotive industry. Recent trends of strengthened environmental regulations and safety have driven automotive companies to apply high strength steels for light weighting of vehicles and reducing gas emissions [8]. Steelmakers are facing pressure to respond to this growing demand with the development of new generations of AHSS.

These grades of steels have been the subject of interest for many researchers for their microstructure and mechanical properties [9,10]. In contrast, published data about the processing of them are scarce. Argon Oxygen Decarburization (AOD) is proposed as a potential candidate to produce high manganese steels with desired low carbon concentrations in a similar manner to stainless steelmaking [11]. Manganese losses by

evaporation and oxidation could be compensated with the addition of reductants such as ferrosilicon in the reduction stage of AOD. The pilot plant data shows that the yield of manganese in this method could be more than 92% [12].

1.2 Objectives of this Study

The primary objective of this study is to develop a deep understanding of the kinetics and mechanisms of decarburization and manganese losses from high manganese steel in the Ar-O_2 bubbling process. The detailed objectives of the current research are listed as follows:

1. To obtain quantitative data for the decarburization and demanganization for different initial carbon and manganese contents at a constant temperature. To propose a mechanism to explain the manganese losses that work both thermodynamically and kinetically. To compare the behavior of manganese with chromium in AOD processing of stainless steels.
2. To obtain quantitative data for the decarburization and demanganization under various gas flow rates and gas compositions.
3. To obtain quantitative data for the decarburization and demanganization for various temperatures, depth of nozzle submergence, and alloy compositions. To study the competition between carbon and manganese for oxygen during the process. To compare the behavior of carbon and manganese in the experiments with the thermodynamic prediction.

1.3 Thesis Outline

Chapter 1. Introduction. This chapter provides the general introduction to the research, and the motivation for this study, and defining the research objectives and structure of this thesis.

Chapter 2. Literature Review. This chapter reviews the related literature about the fundamentals of AOD process, thermodynamics of decarburization in AOD process, and oxygen refining of high manganese steels.

Chapter 3. "Argon–Oxygen Decarburization of High-Manganese Steels: Effect of Alloy Composition" This chapter presents the results of laboratory studies on the effect of alloy composition on decarburization and manganese losses from Fe-Mn-C alloys during Ar-O_2 bubbling. This research aims to investigate the competition between carbon and manganese for oxidation. Assuming the products of reactions are CO and MnO, the combination of loss as manganese oxide and vapor are not enough to justify the total manganese loss. It was demonstrated both thermodynamically and kinetically that the excess manganese loss occurs by the evaporation of manganese at the surface of the bubble and condensation into liquid manganese mist inside the bubble. The driving force for this mechanism was the temperature gradience between the surface and interior of the bubble which was a consequence of exothermic oxidation of carbon and manganese.

Chapter 4. "Kinetics of Decarburization and Manganese Loss from Fe-15Mn-1C Alloys by Bubbling of Argon-Oxygen Gas Mixtures" The purpose of this chapter is to study the

competition between carbon and manganese for oxidation at higher carbon contents compared to those studied in the previous chapter. Moreover, the effect of the total gas flow rate and oxygen concentration in the gas mixture on decarburization and manganese losses, are investigated. This chapter aims to understand if the AOD mechanism by the argon dilution effect can be applied to high manganese steels in the same way as stainless steel. The experimental results showed that the experiments with the lowest O_2 concentration were the most efficient in terms of oxygen utilization for the decarburization.

Moreover, the overall rates of decarburization and demanganization increased with the gas flow rate and oxygen in the gas mixture. The oxygen supply rate is ultimately rate determining but the ratio of manganese loss to decarburization is controlled by the relative mass transport of Mn and C in the metal. The ratio of the mass transfer coefficients for C and Mn in the liquid were estimated using an approach where the ratios of losses were equal to the ratio of fluxes in the liquid. It was found that the mass transfer coefficient of manganese from the experimental results was 3 times smaller than that of carbon in molten Fe-C alloy. This is consistent with the smaller diffusivity of Mn in liquid Fe. Based on the mass transfer coefficients, the reaction times were estimated to about 1% of the residence time of the bubble in the liquid and there was not complete thermodynamic equilibrium with the bubble in the melt. Furthermore, it was speculated that the manganese loss was in the form of MnO dust rather than slag inside the bubble. As any slag would be capable of being reduced back to the melt. However, there was no evidence from experiments for that phenomenon.

Note: While chapters 3, 4, and 5 are pre-publication copies of papers submitted to peer-reviewed journals an additional information section was added to chapter 4 to show the steps used in the calculations of interfacial values of C and Mn, number of moles of CO, CO_2, MnO, and FeO, and the ratio of mass transfer coefficients of Mn/C.

Chapter 5. "Argon Oxygen Decarburization of High Manganese Steels: Effect of Temperature, Alloy Composition, and Submergence Depth" This chapter aims to provide a broader insight into the behavior of manganese and carbon under different experimental conditions. It was shown that the rate of decarburization increased at the expense of manganese losses at higher temperatures. The results showed that the concentration of manganese and carbon versus time were not affected by the depth of submergence. This indicated that the time for the reaction of manganese and carbon with oxygen is much shorter than the residence time of the bubble in the liquid. This finding agreed with the previous chapter's results.

Chapter 6: Concluding Remarks. This chapter summarizes findings from the previous chapter, draws some general conclusions, and proposes some further work to address the remaining questions.

Chapter 2

2 Literature review

2.1 AOD Process

Following the observation of the effect of argon dilution on oxygen decarburization by Krivsky in 1954, the Linde Argon Oxygen Decarburization (AOD) process was invented [13] and commercialized in the early 1970s. Since then, it has been the most efficient and reliable method for the refining of stainless and specialty steels [14,15]. The EAF-AOD duplex process consists of melting scrap and raw materials in an Electric Arc Furnace (EAF) and thereafter decarburization and secondary refining of the melt in the AOD converter [16,17]. This allows using a broad range of materials such as inexpensive high-carbon ferrochromium and green scrap used to increase the chromium content, both in the furnace and the converter [17–21]. Figure 2.1 shows the schematic of an AOD converter with side tuyere and top blowing lance. A mixture of Ar-O_2 is injected into steel through several sidewall tuyeres located near the bottom of the converter. Simultaneously, pure oxygen (or mixed with inert gas) is blown into the bath through a top lance to maximize oxygen delivery into the steel [22,23]. The molten metal in the AOD converter is stirred strongly and encounters circulatory motions because of bottom gas injection as shown in Figure 2.1. Therefore, melt temperature and composition is homogeneous and the rate of reactions is enhanced.[24]

The AOD process is divided into two stages of decarburization and reduction/desulfurization [25]. In order to reduce the cost, Ar can be replaced by N_2 for the

early stages of the process [14,26]. However, using Ar is essential during the last stage of decarburization and reduction stage to eliminate the pickup of nitrogen [27]. However, for some grades of stainless steels, Ar is replaced with nitrogen to improve the mechanical properties [26,28]. Each stage of AOD process is discussed in detail in the following sections.

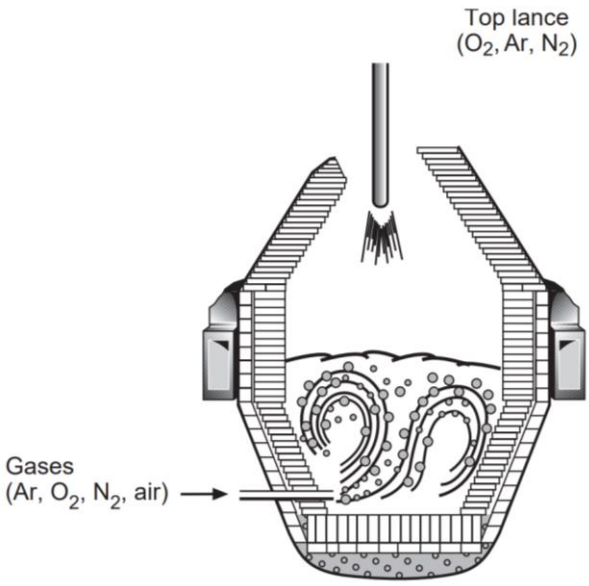

Figure 2.1 Schematic of AOD converter [16].

2.1.1 Decarburization Stage

Oxygen injected through side tuyeres reacts with the dissolved Cr ad C in bath according to the reaction 2.1, and reaction 2.2 [14,29]. Oxidation of Fe is neglected as FeO is an intermediate product of refining and it is instantly reduced by C and Cr [30,31].

$$C + \frac{1}{2}O_2 = CO \quad (2.1)$$

$$2Cr + \frac{3}{2}O_2 = Cr_2O_3 \quad (2.2)$$

The Cr_2O_3 particles are adsorbed on the surface of bubbles containing CO and Ar (or N_2) and ascend in the bath with gas bubbles. The dissolved carbon in the bath is transferred to the surface of bubbles and decarburization takes place according to reaction 2.3. Hence, some of the chromium is recovered back into melt [31,32].

$$Cr_2O_3 + 3C = 2Cr + 3CO \quad (2.3)$$

The direction of reaction (2.3 is significantly affected by the temperature and gas composition. Through dilution of CO with Ar the partial pressure of CO in the gas bubble is lowered, resulting in enhanced decarburization and minimized oxidation of chromium[33]. Prior to the work by Krivsky [13], Richardson *et al*. [34] experimentally established the equilibrium correlation of carbon and chromium in stainless steel refining with CO-CO_2 gas mixtures. As seen from their finding in Figure 2.2, decarburization to low levels of carbon can be carried out without excessive loss of chromium at a higher temperature and lower partial pressure of CO.

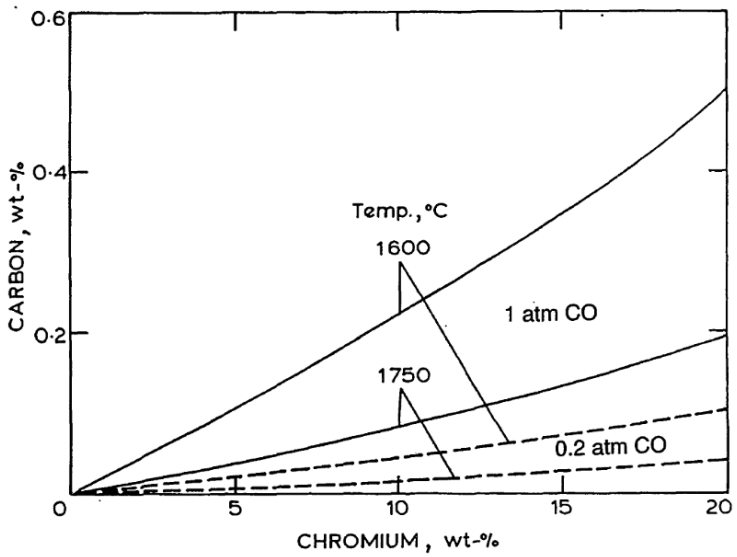

Figure 2.2. Percentage of carbon in equilibrium with chromium at designated temperatures and CO pressures; reprinted with permission [32].

Figure 2.3 shows an example of a blowing procedure for the refining of the stainless steel grade 304 in a 120-ton AOD vessel [35]. During the Main blow (first 11 minutes), the process gas is composed of about 90% oxygen which is supplied from tuyeres and a top lance. As the carbon decreases in the bath to very low concentrations, its activity drops rapidly, which makes chromium oxidation increasingly favorable. For this reason, the ratio of oxygen to inert gas is lowered in a stepwise manner with time in three stages of dynamic blowing (until 38 minutes). In this manner, carbon oxidizes in preference over chromium in the bath [20,21,36–38].

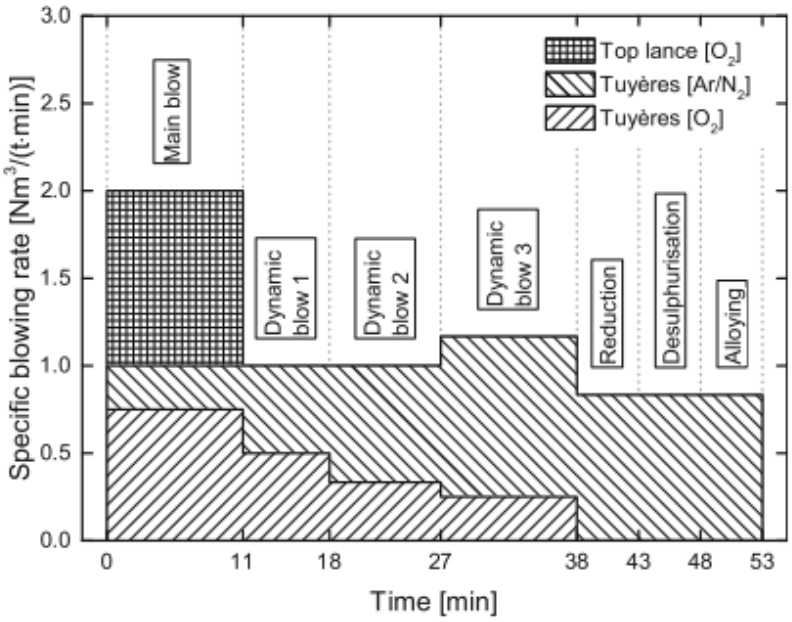

Figure 2.3 An example of blowing pattern for a 120-ton AOD converter; reprinted with permission [35].

Figure 2.4 shows typical variations of temperature and alloying elements in the bath with time for an AOD converter. The bath temperature increases sharply from 1550 to 1700°C because of the heat released from the oxidation of alloying elements such as Si, Mn, Cr, and C. [18,28]. However, it remains roughly constant between 1700 to I720°C as a consequence of adding coolant such as lime or ferrous alloys to protect the converter's refractories from damage [39,40].

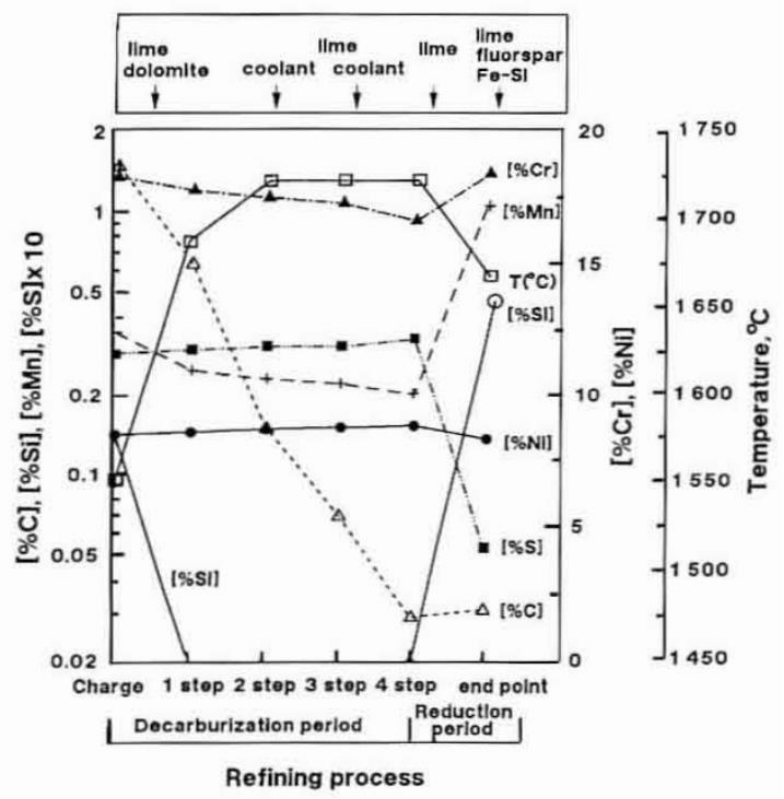

Figure 2.4 Temperature and composition of melt with time for an AOD converter; reprinted with permission [39].

2.1.2 Reduction/Desulfurization Stage

In the reduction stage, argon is injected through the side tuyeres for typically 5 [35] (to 17 [41]) minutes (as shown in Figure 2.3) to vigorously stir the melt. The reductant such as ferrosilicon and aluminum are added to reduce chromium oxide from slag back into the melt [39,42]. The reduction of Cr_2O_3 in slag by Fe-Si is according to reaction 2.4 [41]:

$$2Cr_2O_3 + 3Si = 3SiO_2 + 4Cr \qquad 2.4$$

Figure 2.4 shows that bath temperature dropped by 50°C in the reduction stage because of adding flux, reducing agents, and argon for stirring. The purpose of adding fluxes is to adjust the viscosity and basicity of slag. The viscosity of slag increases with Cr_2O_3 [43], this makes it excessively viscous by the end of the decarburization stage. Song *et al.* [39] recommended keeping slag basicity $\left(\frac{\%CaO}{\%SiO_2}\right)$ above 2 for optimum recovery of chromium from slag and for desulfurization. Additionally, to increase the fluidity of slag, the melt temperature should be higher than 1670℃.

The general ionic desulfurization reaction can be written as Equation 2.5 [28]. A highly basic slag, a well-deoxidized bath with low oxygen potential, and high temperature are the requirement for effective sulfur removal from the melt. Another important factor is good slag-metal mixing which is achieved by argon stirring during this stage.

$$(O)^{2-} + [S] = +[O] + (S)^{2-} \quad (2.5)$$

2.2 Processing of Stainless Steel

2.2.1 Effect of Cr Concentration

Barnhardt [44] investigated the parallel oxidation of carbon and chromium during air bubbling into Fe-Cr-C alloys containing 0.3% C and 0, 10, 15, and 20% Cr in an induction stirred furnace. The working temperature was 1873 K. Air was injected into steel at the flow rate of 300 ml/min (S.T.P). He found that above a critical carbon concentration, decarburization followed a linear trend regardless of initial chromium concentration. Once a critical carbon point was reached, carbon deviated from the linearity depending on the

chromium concentration. The rate of decarburization increased with lowering the initial chromium concentration (Figure 2.5). The critical carbon was not a fixed value and varied between 0.1 to 0.2%C depending on the chromium content. The corresponding chromium contents of melt with time are shown in Figure 2.6. As seen, initially there was no chromium loss. However, below the critical carbon content, oxidation of chromium started. The rate controlling step at high carbon concentrations was the supply of oxygen, and it switched to the diffusion of carbon to the gas-metal interface at lower carbon contents.

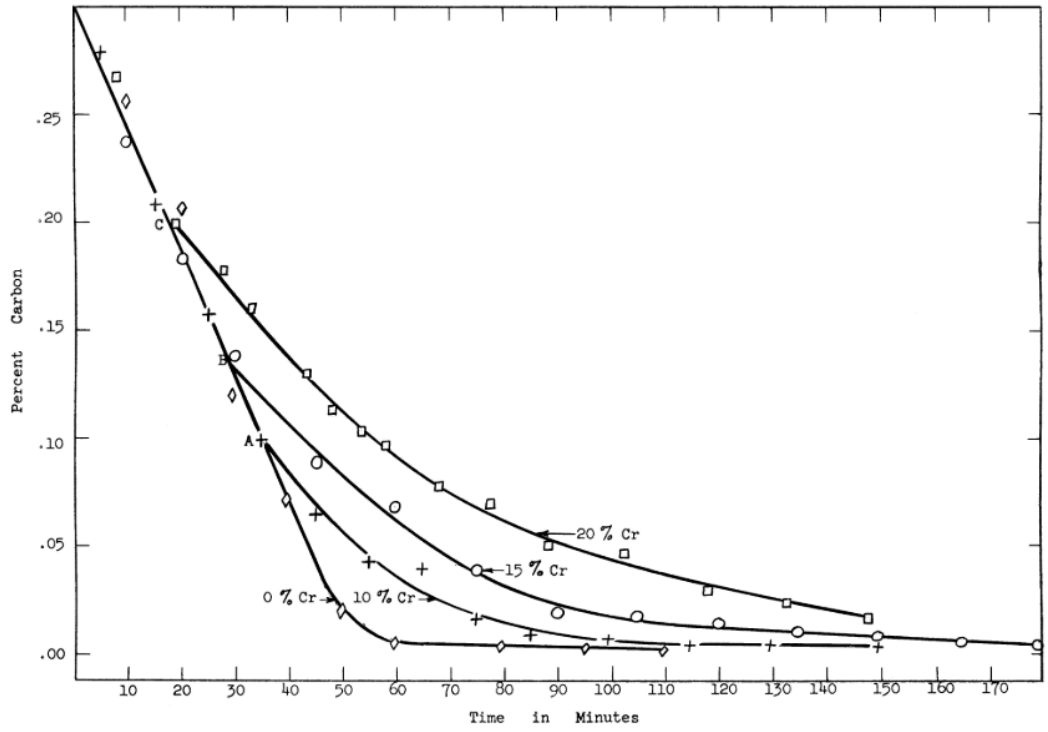

Figure 2.5. Carbon concentration versus time during air bubbling, gas flow rate= 300 ml/min, T=1873 K, variable: chromium concentration; reprinted with permission [44].

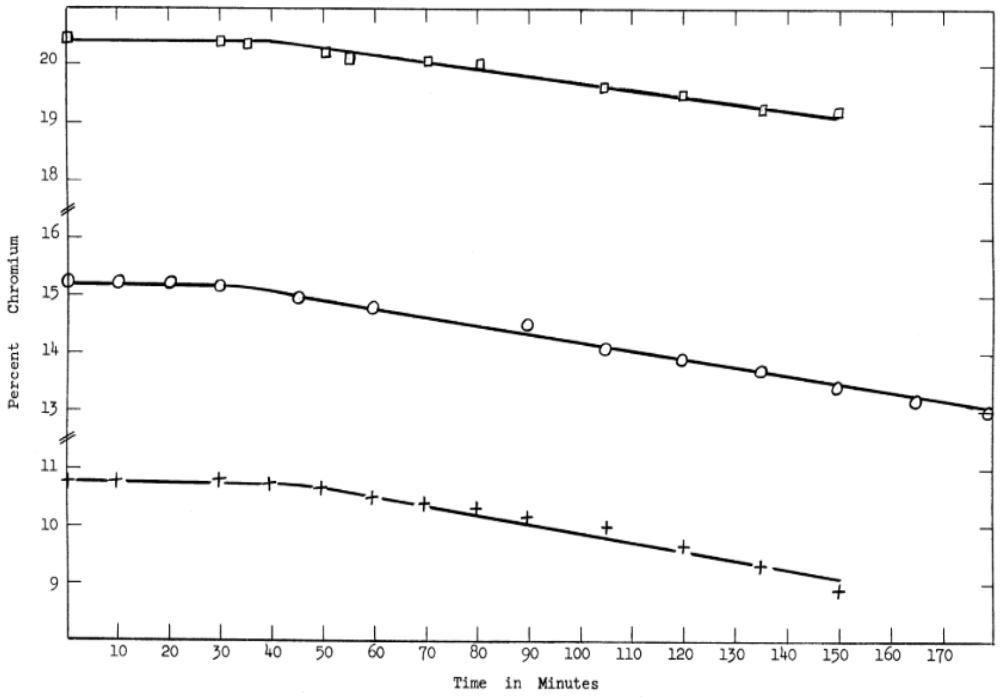

Figure 2.6 Chromium concentration versus time during air bubbling, gas flow rate= 300 ml/min, T=1873 K, variable: chromium concentration; reprinted with permission [44].

2.2.2 Effect of Temperature

Healy *et al.* [45] established the correlation between the total oxidation loss of chromium, manganese, and iron from stainless steel heats with respect to the initial charge during the oxidation period. These workers showed the significance of temperature in minimizing metallic loss by oxidation (Figure 2.7). However, extremely high temperatures or operating at prolong high temperature should be avoided because it imposes severe damages to the refractories [45–47].

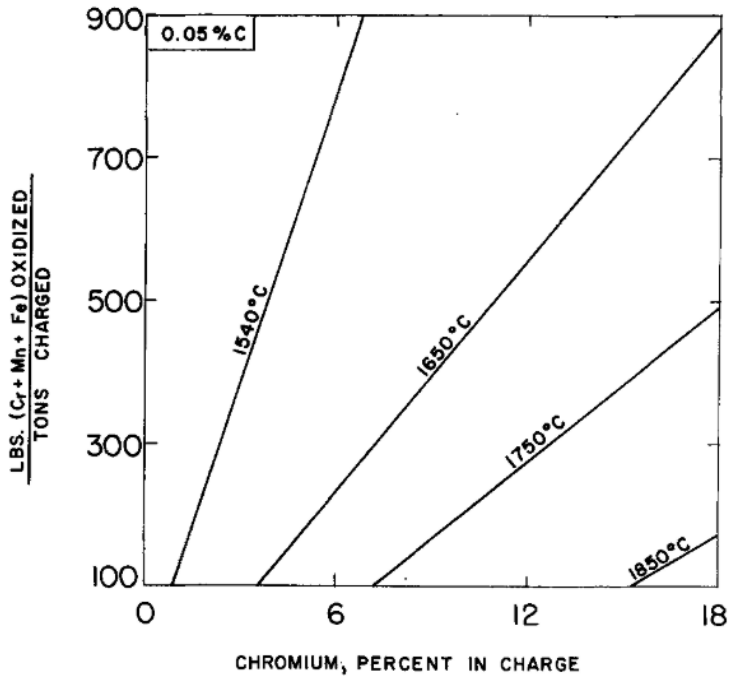

Figure 2.7 Correlation between metallic oxidation and chromium in charge during oxygen blowing, variable: temperature; reprinted with permission [45].

2.2.3 Effect of Gas Composition

Fruehan [26] performed Ar-O_2 bubbling into a shallow bath (7.5 cm) of stainless steel. His results showed that the rate of oxidation of chromium was faster than decarburization. Also, the ratios of chromium to carbon oxidation were the same as their concentration ratios. This was the basis of an assumption for his reaction model for the AOD [31]. He proposed that the injected oxygen in the vicinity of the tuyeres was mainly consumed for the oxidation of chromium and Cr_2O_3 was reduced by carbon while rising with the argon bubble in the bath according to reaction 2.3. Also, he assumed that the rate of decarburization was controlled

by mass transfer of carbon in the liquid phase. The predicted rate of decarburization of Fe-10%Cr-1.2%C alloy at 1948 K by this model is shown

in Figure 2.8. These data were validated by good agreement with two industrial heats. As seen, the rate of decarburization increased with increasing O_2/Ar ratio from 3:1 to 6:1. At high carbon concentration, most of the oxygen was utilized for the decarburization, and chromium loss to slag was either small or zero. However, below the critical carbon content (0.2%), the decreasing O_2/Ar ratio promoted decarburization. The critical carbon concentration is the point where chromium loss starts and the rate controlling step switches from the rate of oxygen supply to the rate of transfer of carbon to the gas/metal interface [48,49].

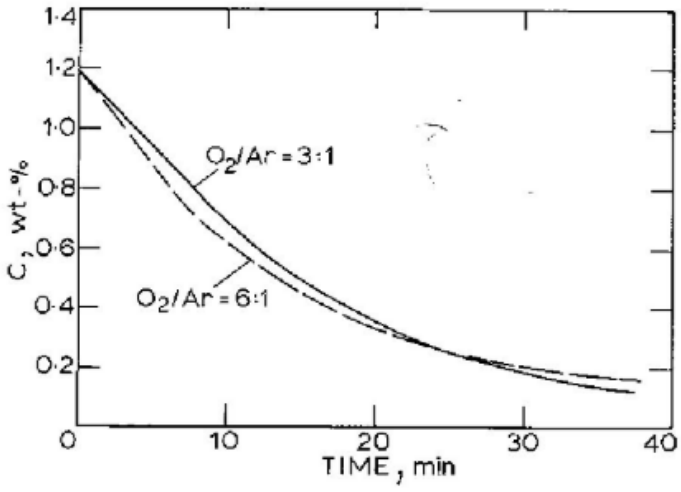

Figure 2.8. Rate of decarburization for stainless steel grade 409; reprinted with permission [31].

Figure 2.9 shows Fruehan's results for the prediction of decarburization and chromium loss from stainless steel grade 409 at various gas compositions for the final stage blow with less than 0.2% carbon. As observed, increasing argon in the gas mixture improved the rate of

decarburization and decreased chromium oxidation. The proper O_2/Ar ratio for the refining process depends on evaluating the cost of argon versus ferrosilicon which is used in the reduction stage to reclaim chromium from slag [31].

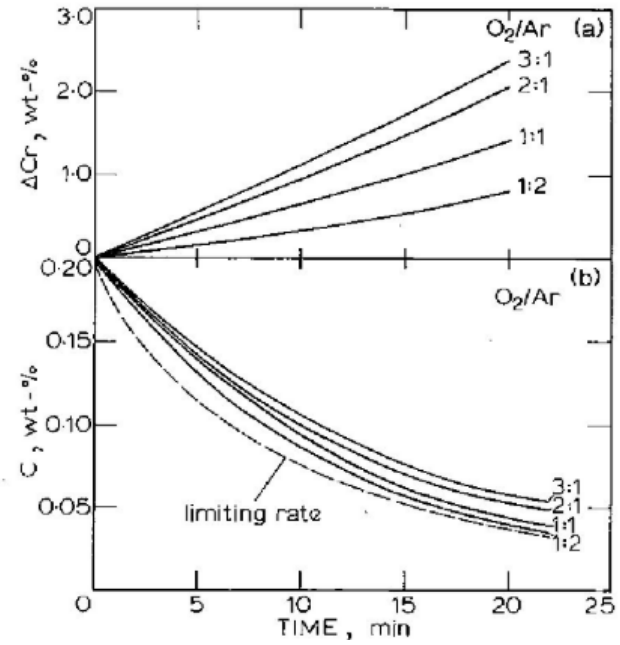

Figure 2.9. Effect of gas composition on decarburization and chromium loss from stainless steel grade 409; reprinted with permission [31].

2.2.4 Effect of Bath Depth

With similar assumptions to Fruehan's model, Ohno *et al.*[50] developed an AOD model that considered the change in bubble size during its rise in the bath. Figure 2.10 (a-c) shows the ratio of the partial pressure of CO to that of equilibrium in Ar bubbles $\left(\frac{p_{CO}}{p_{CO_e}}\right)$ (at bath surface as a function of bath depth (distance from tuyeres to the surface of the bath) at 1650 ℃ for the initial bubble size of 5, 10, and 2.5 cm, respectively. O_2/Ar ratio was 1:1. Figure

2.10 (a) shows that $\frac{\mathrm{pco}}{\mathrm{pco_e}}$ in Ar bubble for the initial diameter of 5 cm increased sharply for depths lower than 50 cm. However, depths more than 50 cm made no differences in $\frac{\mathrm{pco}}{\mathrm{pco_e}}$. As seen in Figure 2.10 (b), bath depth had a more significant effect on bubbles with larger initial diameters (10 cm). Therefore, they recommended that for larger bubbles to deepen the bath as much as possible. They further stated that for the conditions that depth of 50 cm or less is inevitable, the bubble size must be reduced through redesigning the system, for instance using nozzles with smaller diameters.

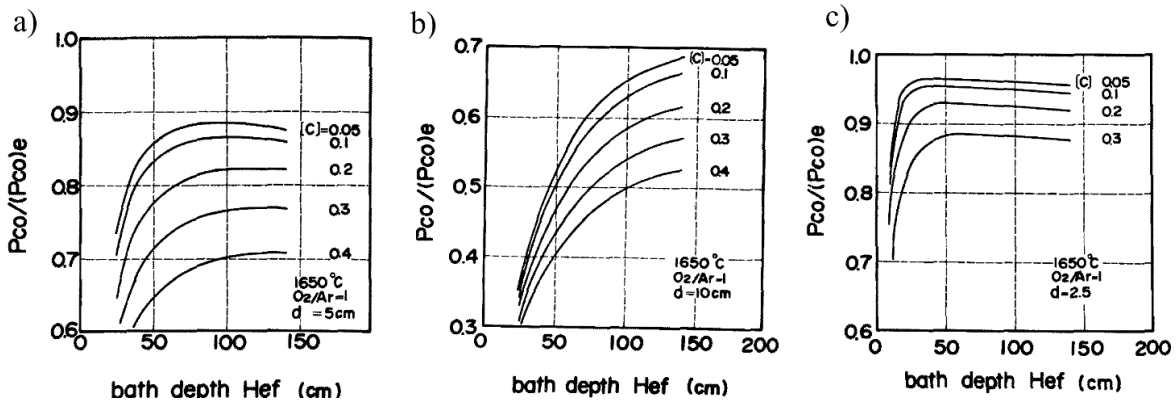

Figure 2.10 $\frac{p_{CO}}{p_{CO_e}}$ in Ar bubbles at bath surface versus effective bath depth (distance from tuyeres to the surface of molten steel), initial bubble diameters are a) 5, b) 10, and c) 2.5 cm; reprinted with permission [50].

Krivsky [13] was the first who recognized for efficient decarburization in the AOD process, argon must be injected sufficiently deep in the melt to be dispersed thoroughly. Later, this finding was confirmed in Fruehan [26] and Saccomano *et al.* [51]. In Fruehan's work (explained in Section 2.2.3), the depth of the bath above the nozzle was 7.5 cm, and bubble ascending time was not enough for the reduction of chromium oxide by carbon to proceed

significantly. Kobayashi *et al.* [52] suggested a mechanism for the decarburization of stainless steel by Ar-O_2 bubble during its rise in the bath as shown in Figure 2.11. Due to the high oxygen potential in the region I, immediately after the Ar-O_2 bubble hit the molten steel, chromium and carbon oxidized simultaneously. As the bubble rose in the melt, oxygen potential decreased and most of chromium oxide in the bubble was reduced back into the melt by carbon in region II. Finally, direct decarburization occurred in region III, they called it the dominant oxidation phase. By this mechanism, they pointed to the importance of the immersion depth in decarburization by Ar-O_2 gas bubbles as a condition for shifting to the dominant oxidation phase.

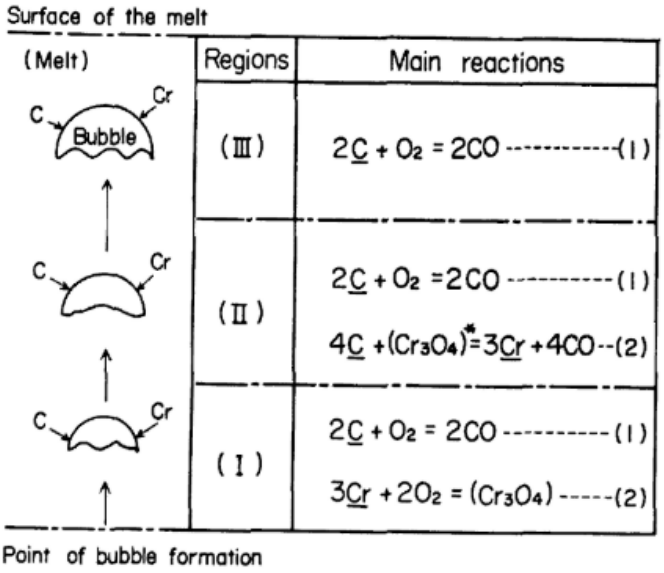

Figure 2.11 Schematic of decarburization by Ar-O_2 gas bubbles while rising in the bath; reprinted with permission [52].

2.2.5 Effect of Blowing Method

Figure 2.12 shows the rate of decarburization as a function of carbon concentration for top blowing, bottom blowing, and combined blowing in a 100 kg furnace from the work of Tsujino *et al*.[53] The total oxygen flow rate for each blowing mode was 100 Nl/min. The ratio of top to bottom blown oxygen was 1:1 in combined blowing. The solid symbols show the zones where oxidation of chromium has occurred and the amount of Cr_2O_3 in slag has increased. The rate of decarburization improved in the order of top blowing, bottom blowing, to the combined blowing. Furthermore, in the same order the carbon concentration at which oxidation of chromium started, decreased. The observation of slag while blowing gas showed that slag had been solidified. In the top blowing configuration, the solidified Cr_2O_3 covered the surface of the bath and impeded the top-blown oxygen from reaching and reacting with the steel. These researchers reported that the hot spot temperature in top blowing and combined blowing was 2350℃ using a radiation thermometry method. The examination of hot spot samples using optical microscopy and electron-probe microanalyzer (EPMA) demonstrated the presence of chromium oxides. Thereby, it was verified that the hot spot had an extremely high temperature and created a high oxygen zone. The concentration of oxygen in the hot spot was found to be reduced significantly by combined blowing. Furthermore, they found that combined blowing was beneficial because of the vigorously stirred melt in bottom blowing enhanced the oxygen transfer from the hot spot which led to higher rates of decarburization. Additionally, the reduction of Cr_2O_3 by carbon at the hot spot was promoted.

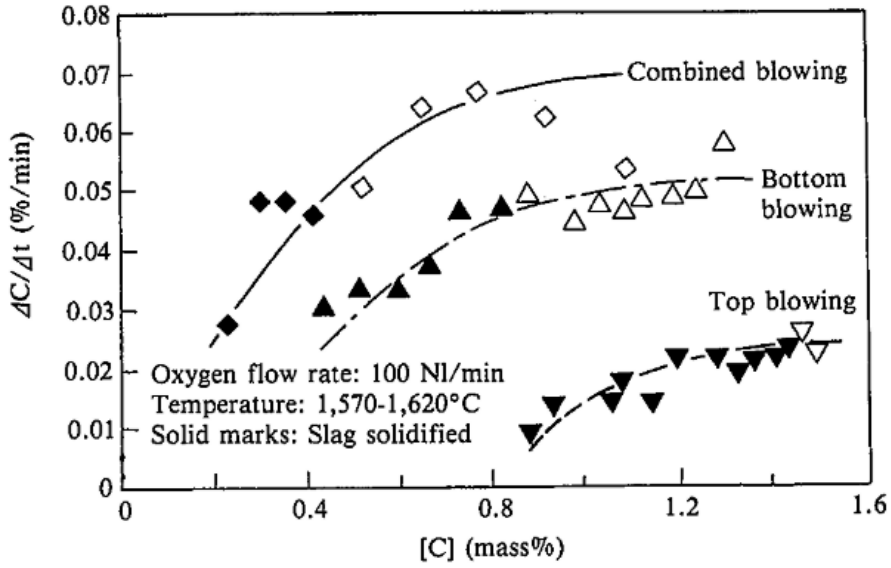

Figure 2.12. Rate of decarburization versus carbon concentration of stainless steel in a 100-kg furnace for top, bottom, and combined blowing; reprinted with permission [53].

2.3 High Manganese Steels

2.3.1 Reactions in Argon-Oxygen Decarburization Process

The oxidation reactions of carbon and manganese dissolved in the molten high manganese steel and iron as the matrix of steel with injected oxygen take place according to Equations 2.1 and 2.6 through 2.8.

$$C + \frac{1}{2}O_2 = CO \qquad \Delta G_1^0 = -117562 - 84.2T \text{ [54]} \qquad (2.1)$$

$$C + O_2 = CO_2 \qquad \Delta G_6^0 = -396360 - 0.11T \text{ [54]} \qquad (2.6)$$

$$Mn + \frac{1}{2}O_2 = MnO \qquad \Delta G_7^0 = -405728 + 87.6T \text{ [54]} \qquad (2.7)$$

$$Fe + \frac{1}{2}O_2 = FeO \qquad \Delta G_8^0 = -243051 + 50.7T \text{ [54]} \qquad (2.8)$$

The evaporation reaction of manganese is expressed by Equation 2.9:

$$Mn(l) = Mn\ (g) \qquad \Delta G_9^0 = 238892.3 - 103.95T\ [54] \qquad (2.9)$$

The other potential reactions in this system can be written by combining Equations 2.7 and 2.8 with Equations 2.1 and 2.6:

$$MnO + C = Mn + CO \qquad \Delta G_{10}^0 = 288166 - 171.8T\ [54] \qquad (2.10)$$

$$Mn + CO_2 = MnO + CO \qquad \Delta G_{11}^0 = -126928 + 3.5T\ [54] \qquad (2.11)$$

$$FeO + C = Fe + CO \qquad \Delta G_{12}^0 = 125489 - 134.9T\ [54] \qquad (2.12)$$

$$Fe + CO_2 = FeO + CO \qquad \Delta G_{13}^0 = 35748 - 33.4T\ [54] \qquad (2.13)$$

The carbon concentration in Fe-Mn-C melt can be determined by the thermodynamics of reaction 2.10. Assuming that the activity of MnO is equal to 1, the activity of carbon can be expressed as a function of the partial pressure of CO, the activity of manganese in the melt as follows:

$$a_C = \frac{p_{CO} a_{Mn}}{K_{10}} = p_{CO} a_{Mn} \exp\left(\frac{34660}{T} - 20.7\right) \qquad (2.14)$$

K_{10} is the equilibrium constant for Equation 2.10 and a function of temperature. Olsen *et al*. [55] calculated the equilibrium carbon concentration of 80Mn-15Fe-5C alloy versus temperature for various partial pressures of CO using FactSage. As shown in Figure 2.13, in the case of manganese oxygen refining (MOR) where the p_{CO}=1 atm, carbon concentration of 1.1% could be achieved at 1800℃. However, this high temperature results in excessive manganese evaporation [56]. According to Dresler [57], the evaporative

manganese loss from 80Mn-1C ferromanganese at 1840℃ was estimated to be 3.5% due to the high vapor pressure of manganese (0.215 atm). Hence, it was suggested to keep the processing temperature less than 1800℃. To obtain the lower carbon contents in alloy without unwanted manganese loss, argon could be used to dilute CO [55,57].

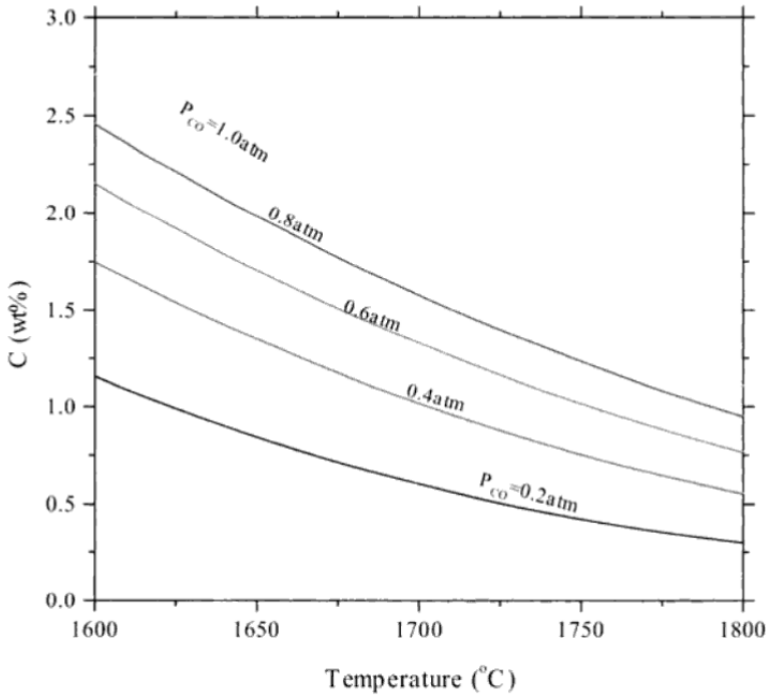

Figure 2.13 The equilibrium carbon concentration versus temperature for 80Mn-15Fe-5C, variable: partial pressure of CO, reprinted with permission [55].

2.3.2 Activity of Carbon and Manganese in Liquid Fe-Mn-C System

The thermodynamic properties and phase equilibria of Fe-Mn-C have been studied broadly, both experimentally and theoretically [57–63]. A few of these studies are reviewed here which are the most relevant to the present work in terms of temperature range and alloy composition.

Dresler [57,64] derived a thermodynamic model to predict the equilibrium concentration of manganese, carbon, and silicon during oxygen refining of ferromanganese alloys. His model predicts the carbon and manganese activities over a wide range of temperatures from 1350 to 1700°C and a wide range of composition of iron-manganese-carbon alloys. The assessment of the activities of manganese and carbon were performed by applying the Wagnerian Taylor series expansion with the mole fraction coordinate. The interaction coefficients were taken from the work of previous researchers [65,66]. For carbon activity, data for the dilute solution and saturated carbon employed in his model. And for the medium-range carbon, he conducted experiments with 500 g of ferromanganese containing 1 to 4% carbon at temperatures of 1500 to 1650℃. For the purpose of oxygen refining, he added Mn_3O_4 to melt and carried out experiments under an argon atmosphere. Figure 2.14 shows the predicted activity of manganese for a wide range of composition in his work.

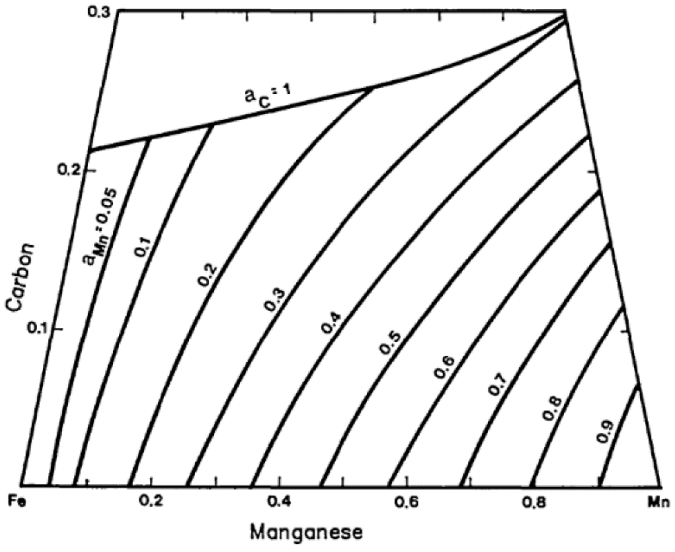

Figure 2.14 Activity map of Mn in molten Fe-Mn-C system at 1600℃ with respect to pure liquid Mn, reprinted with permission [57].

It was said that as the reduction reaction of MnO by carbon (Equation 2.10) is governing the oxygen refining of ferromanganese, therefore the equilibrium constant for this reaction can be written as [57]:

$$\ln\left(\frac{a_{Mn}\, p_{CO}}{a_C a_{MnO}}\right) = 16.28 - \frac{25800}{T} \qquad (2.15)$$

Dresler [57] assumed that the activity of MnO is unity in all of his experiments. Also, manganese vapor dilutes CO where total pressure is 1 atm.

$$p_{CO} = 1 - p_{Mn} \qquad (2.16)$$

Then he used Equation 2.17 [67] to correlate the vapor pressure of manganese and it concentration.

$$\ln\left(\frac{p_{Mn}}{a_{Mn}}\right) = 37.67 - 3.021\ln T - \frac{33430}{T} \qquad (2.17)$$

By combining Equations 2.15 to 2.17, he found the activity of carbon as a function of manganese concentration and vapor pressure, and temperature. The solution to this model for carbon concentration was in good agreement with his experimental findings for 25 to 74%Mn alloys. It was reported that the model was validated against plant data in a 10-t Q-BOP at a higher temperature (1875°C), with good agreement. However, the accuracy of the model in predicting activities was more satisfactory for the medium-range carbon contents [57].

Figure 2.15 illustrates the variation of carbon with manganese in the presence of saturated MnO slag at 1750 ℃ in Dresler's [57] model. This figure shows the minimum carbon

concentration that can be obtained for each manganese concentration during the oxygen refining process. He showed that at a composition of 80%Mn, 1.38%C, oxygen potential is 2.8×10^{-12} atm. Any further decarburization to lower carbon contents requires blowing more oxygen. Therefore, oxygen potential will increase which leads to more manganese oxidation. As seen in Figure 2.15, for decarburization with carbon levels lower than 1.5%, every 0.2% decarburization will lead to a 10% Mn loss which is not economical. Hence, he suggested the use of argon to dilute blown oxygen to avoid unwanted manganese loss.

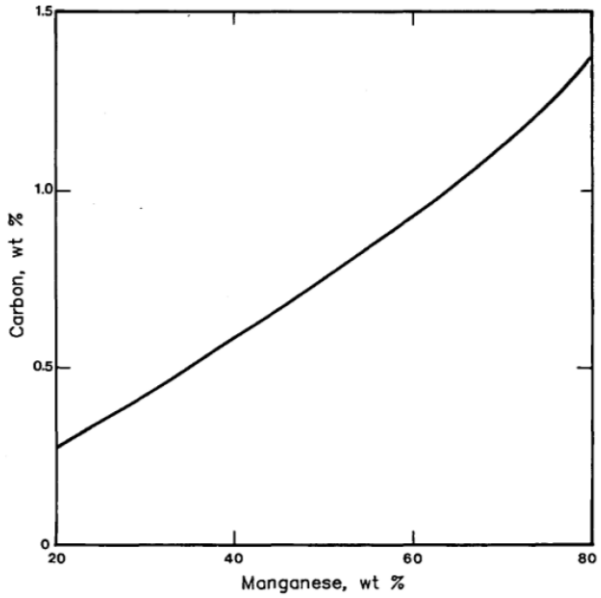

Figure 2.15 The carbon versus manganese concentration with the presence of MnO saturated slag, T=1750℃, reprinted with permission [57].

Although Dresler's assessment could adequately describe the thermodynamic properties of the Fe-Mn-C system. However, the results were only verified with one plant data.

Furthermore, there was only agreement for the activity coefficient of Mn for one composition (21%Mn and 2.3%C) with the work of Schenk *et al*. [62] and Lee *et al.* [63]. Chipman [68] proposed the lattice site ratio model to determine the activity of the interstitial atoms in alloys as the fraction of sites that are occupied by a component (filled to unfilled sites) as a concentration parameter. Unlike the solid crystal structure, in liquids, there is no long-range atomic order. Therefore, the lattice for the liquid system does not mean the same for the solid structures. However, there exists a short-range atomic order in liquid similar to that of solid alloys [61]. Lee [61] developed a model to describe the activity coefficient of manganese and carbon in the liquid iron-manganese-carbon system using the lattice site ratios [68]. These can be expressed as follows:

$$\ln\gamma_C(Fe-Mn-C) = \left(-3.334+\frac{2717.54}{T}\right)+\left(2.1101+\frac{8743.6}{T}\right)X_C+ \left(10.957+\frac{3269.7}{T}\right)X_C^2+1.3304X_{Fe}+\left(2.6346-\frac{496.54}{T}\right)X_{Fe}X_C \quad (2.18)$$

$$\ln\gamma_{Mn}(Fe-Mn-C) = \left(-0.4822+\frac{576.7}{T}\right)X_C+\left(5.1498-\frac{10842}{T}\right)X_C^2+ \left(-25.821+\frac{8289.7}{T}\right)X_C^3-4943.8\,X_C^4\,X_{Fe}^5 \quad (2.19)$$

where γ_C, γ_{Mn} , and T are the activity coefficients of carbon, manganese, and melt temperature. X_C, X_{Mn}, X_{Fe} are the mole fractions of carbon, manganese, and iron.

Figure 2.16 shows the activity coefficient of carbon for carbon saturation in the liquid Fe-Mn-C ternary system calculated by Lee's [61] lattice site ratio model. These activities are determined by considering the solubility of carbon in the Fe-Mn-C system. Although they

were in agreement with the experimental results of previous researchers [68,69] at 1673 and 1773 K, the calculated activity coefficients at 1563 and 1963 K deviated from the experimental results. This discrepancy was due to the same variation in the experimentally determined carbon solubility at these two temperatures.

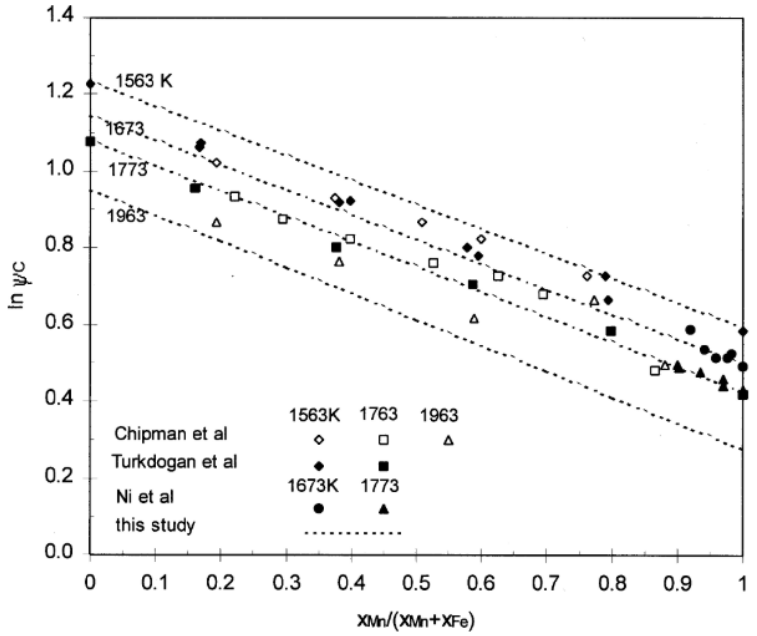

Figure 2.16 Activity coefficient of carbon versus lattice site ratio in Fe-Mn-C calculated by Lee, reprinted with permission [61].

Figure 2.17 shows the calculated activities of Mn in Lee's model [61] by Equation 2.19 for a wide range of Mn and C compositions between the temperature of 1736 and 1823 K. The results (displayed as curves) agreed reasonably compared with the experimental data from Enokido *et al.* [70]. Data for low manganese range and high carbon (mole fractions higher than 0.05) did not agree with Lee's model [61] at 1773 and 1823 K. This discrepancy was

attributed to the determination of the activity of manganese based on the analysis of silver alloy in equilibrium with iron-carbon-manganese alloy [61].

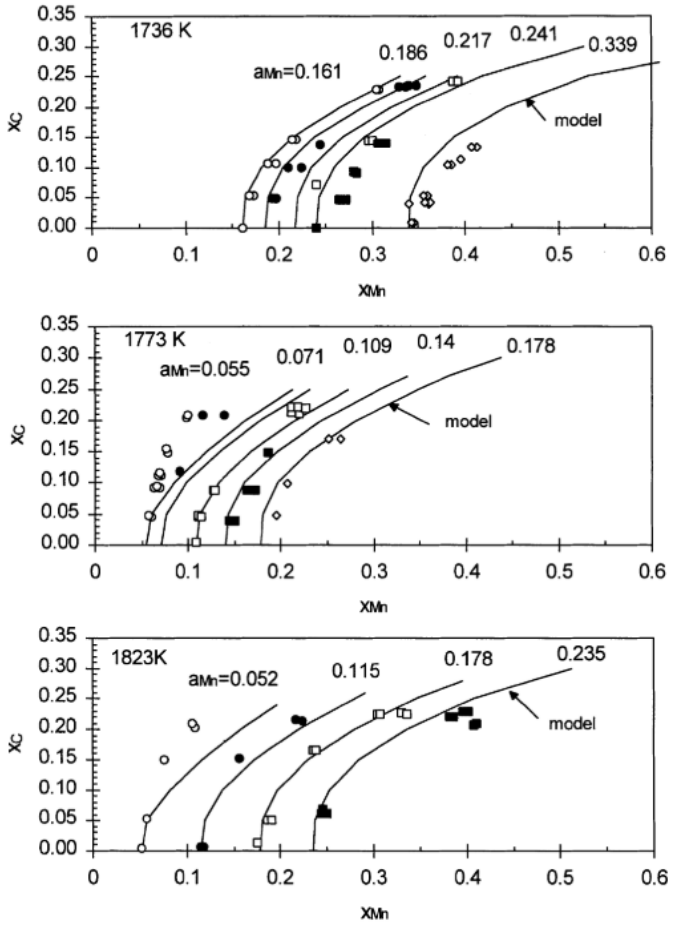

Figure 2.17 The comparison of the predicted activity of manganese in molten Fe-Mn-C system by Lee's model and data by Enokido *et al.* [70], reprinted with permission [61].

As discussed above, there are many thermodynamic assessments for Fe-Mn-C in past studies, however, many of them are developed for the lower temperatures or they are not verified experimentally. For this reason, the activities of carbon and manganese in this work are calculated using Lee's model [61], because the model was verified well with

experimental data for the range of carbon ($X_C < 0.05$) and manganese ($X_{Mn} = 0.1$ to 0.25) which is interested in this work.

2.3.3 Processing of High Manganese Steels

Manganese oxygen refining (MOR) with a similar concept to the basic oxygen furnace (BOF) allows the production of medium and low carbon ferromanganese by blowing oxygen through a lance or bottom tuyeres into high carbon ferromanganese [56]. As explained in the previous section, the final carbon concentration could be as low as 1% if the temperature is increased to 1800℃ (Figure 2.13). However, this results in excessive manganese losses by oxidation and evaporation up to 8% [71]. To decarburize ferromanganese to lower levels, it is essential to use argon to dilute the blown oxygen. There are several possible routes for the production of high manganese steels. For example, blast furnace-basic oxygen furnace (BF-BOF), electric arc furnace-argon/vacuum oxygen decarburization (EAF-AOD/VOD), and Direct reduction-EAF-AOD/VOD [11]. Analogous to the production of stainless steel, EAF-AOD/VOD is a potential candidate for the processing of high manganese steels (Figure 2.18). In this method scrap and ferrosilicon and/or silicomanganese are melted in an electric arc furnace (EAF) and the carbon concentration is decreased in an AOD converter or VOD (rout b). During the reduction stage, Fe-Si and Si-Mn are added to reduce MnO in the slag and bring Mn back into steel. It should be noted that the reduced pressures in argon lead to enhanced manganese evaporation. Therefore, if very low carbon content in the final composition is not required,

most of process can be done in the EAF as long as low carbon scrap and ferroalloys are added. Therefore, rout “a” make the processing route shorter.

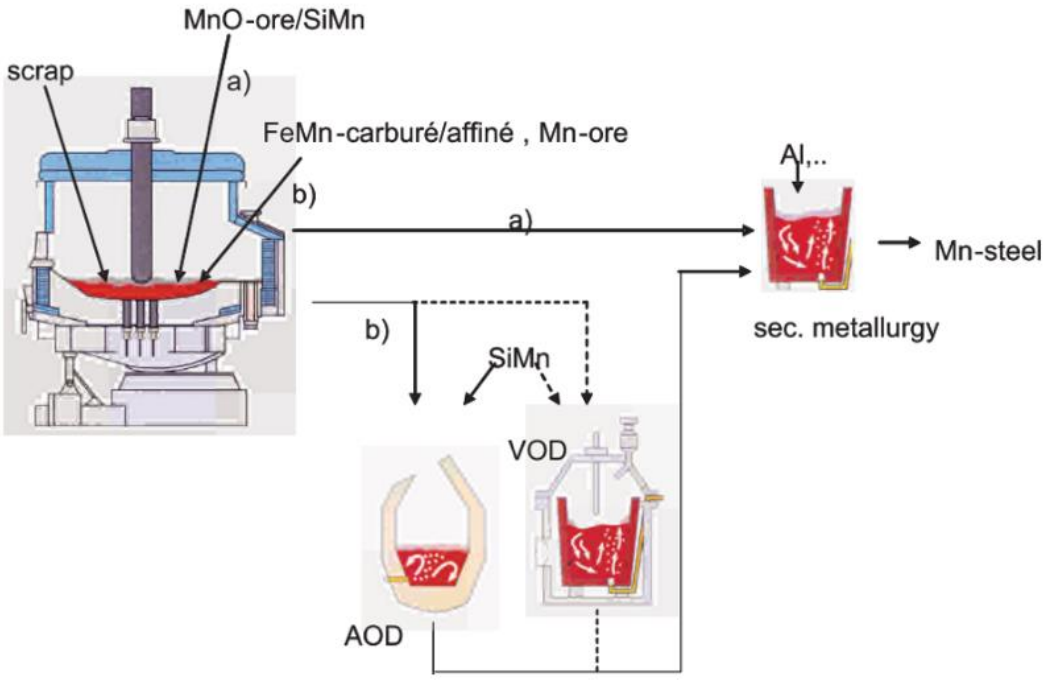

Figure 2.18 EAF-AOD/VOD rout to produce high manganese steels; reprinted with permission [11].

2.3.4 Effect of Temperature and Gas Composition

You *et al*. [72,73] studied the Ar-O_2 bubbling into 130 g of Fe-75Mn-6C alloys in the temperature 1350 to 1550 ℃. The total flow rate was 100 Ncm^3/min and the oxygen mixing ratio (the fraction of oxygen in the gas mixture) varied between 0.14 to 0.79. Figure 2.19 (a) shows the variation of carbon concentration in the melt with time for different oxygen concentrations and temperatures. At 1350℃, carbon concentration increased with time for high oxygen concentrations in the gas mixture. But for oxygen mixing ratios of 0.14 and

0.27 carbon decreased linearly with time. They explained that the increase in carbon content at higher oxygen mixing ratios and lower temperatures is because of the preferential oxidation of manganese compared to carbon. For the proposed mechanism to function in the way shown for 1350 C in Figure 2.19 (a) there must have been sufficient manganese loss to account for the mass change of 10% of the melt. However, at temperatures above 1400℃ carbon content of melt decreased consistently with time, and the rate of decarburization increased with temperature and decreasing oxygen mixing ratio. The dependency of the rate of decarburization on the oxygen mixing ratio was explained by the reduction reaction of manganese oxide with carbon (reaction 2.10). You *et al*. [73] explained that p_{CO} reduced because of the argon dilution effect, resulting in higher rates of decarburization as shown in Figure 2.19 (a). They also related the increase in the rate of decarburization with temperature due to the increasing equilibrium constant (K_{10}). These workers showed that oxygen utilization for the decarburization decreased with higher oxygen in the gas mixture and decreasing temperature. As indicated in Figure 2.19 (b), the oxygen mixing ratio of 0.47 and temperature of 1550℃ with 60% oxygen utilization for the decarburization was the most efficient condition in their experiments for the refining of high carbon ferromanganese.

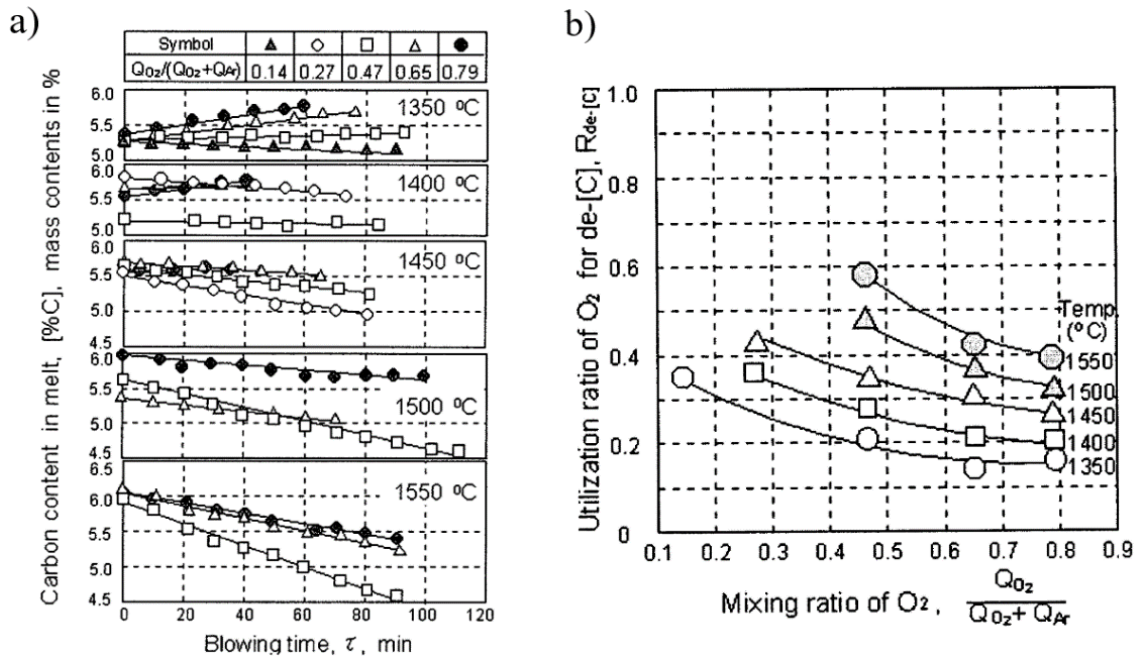

Figure 2.19 a) Carbon concentration in melt versus time, and b) Utilization of oxygen for decarburization versus the mixing ratio of oxygen, variable: melt temperature; reprinted with permission [72].

The results of manganese with processing time were not provided by You *et al.* [72,73]. However, the normalized amount of manganese loss for the initial manganese content versus that of carbon was given for 1400℃, as shown in Figure 2.20. Increasing temperature and oxygen concentration in gas led to higher manganese losses. Based on their observations, they recommended to keep the oxygen mixing ratio as low as possible and temperature at the highest in the early stages of the blow to decarburize ferromanganese efficiently and diminish the manganese loss by oxidation. In their study, there was no further information about the mechanism of manganese loss and they only pointed to oxidation loss.

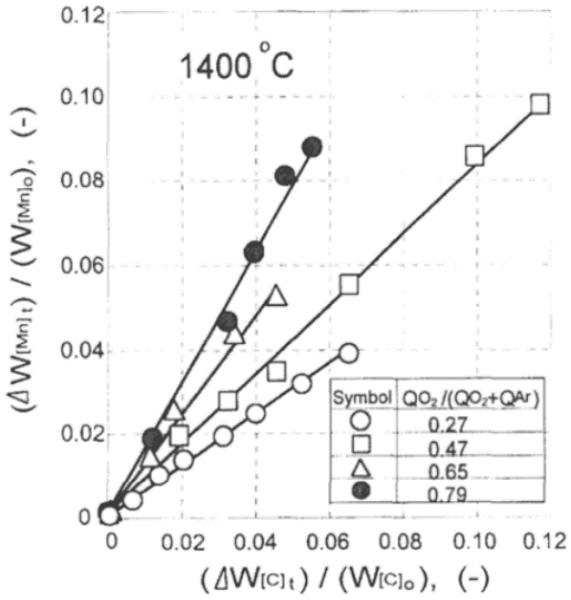

Figure 2.20 The normalized manganese loss versus normalized decarburization at 1400℃; reprinted with permission [73].

2.3.5 Manganese Losses by Evaporation and Oxidation

In further work by You *et al*.[74] decarburization and manganese losses from high carbon ferromanganese (Fe-74Mn-6.8C) in a trial 1.8-ton AOD converter were investigated. Oxygen was blown onto the surface of the melt at a flow rate of 0.8 Nm^3/min per ton of hot metal for 30 minutes. A mixture of $Ar+O_2$ at the total flow rate of 1.5 Nm^3/min per ton of hot metal was injected through three bottom tuyeres. Every 20 minutes from the start of the process, the oxygen mixing ratio (fraction of oxygen in the gas mixture) in bottom tuyeres decreased in a stepwise manner from 0.7, 0.6, 0.35, to 0.15. During the process, lime, dolomite, and fluorspar were added to form slag. During the reduction stage, ferrosilicon and/or silicomanganese were added to reclaim manganese from slag back into the melt while Ar was injected through bottom tuyeres to stir the melt. Samples were taken every

10 minutes from the melt. Figure 2.21 (a) shows the simultaneous carbon and manganese changes in the bath with processing time.

Initially, the rate of decarburization was slow. It was reported that because of the increase in temperature, the rate of decarburization increased in the middle stage. Finally, with decreasing carbon in the bath and oxygen concentration in the injected gas, decarburization slowed down. As seen, the carbon concentration reached about 2% by end of the decarburization stage (about 50 minutes from the start of the process). The manganese concentration nearly remained unchanged until 40 minutes. When carbon concentration decreased to 3%, oxidation of manganese started due to its favorability at lower carbon contents. Then reducing agents were added to the melt and manganese content increased from 50 minutes until the end of the reduction stage. These researchers decarburized high carbon ferromanganese to 1.5% C while manganese at the end of the process was essentially the same as the initial concentration.

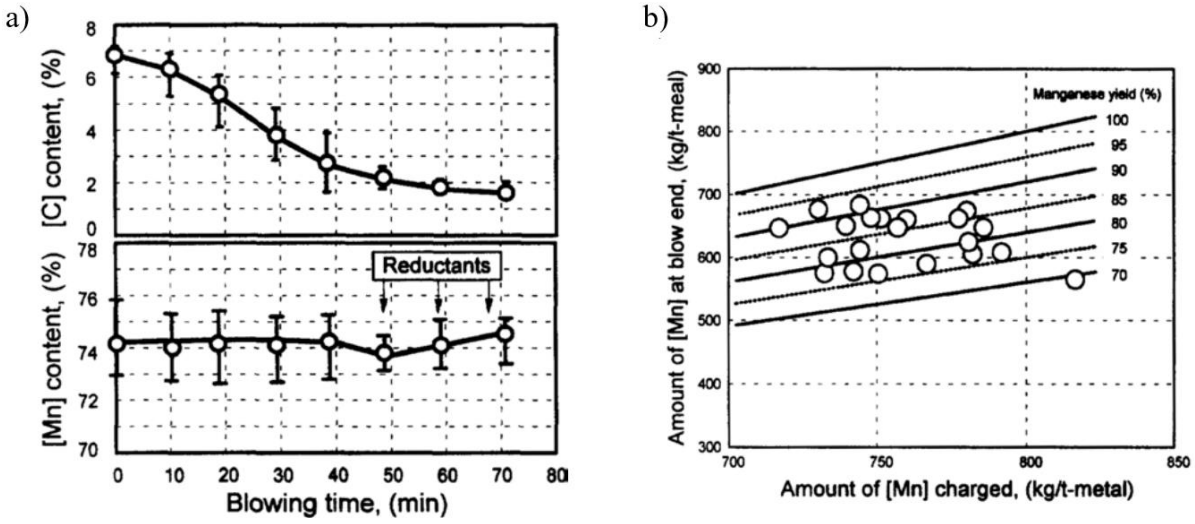

Figure 2.21 a) Simultaneous variations of carbon and manganese in the melt with time, b) The amount of remained manganese in bath versus the amount of charged manganese in a 2-ton AOD converter; reprinted with permission [60].

Figure 2.21 (b) illustrates the correlation between the manganese remaining in the bath at the end of the process and the amount of charged manganese for various trial heats by You *et al*. [74] As indicated, the yield of manganese varies between 75 to 95%. This implies that between 5 to 25% manganese loss as evaporation and oxidation had occurred.

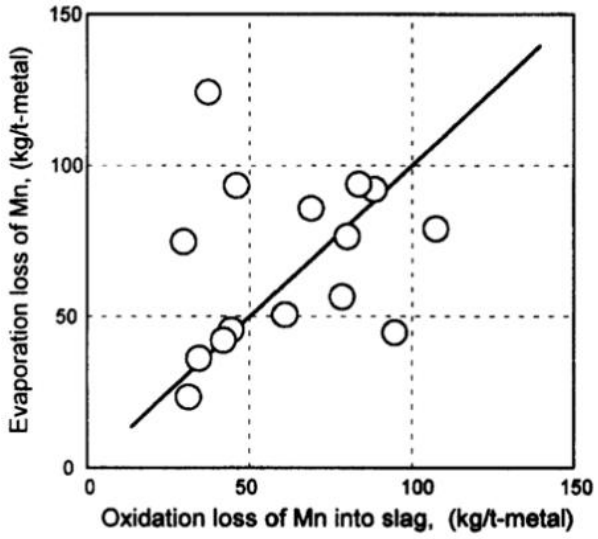

Figure 2.22 The evaporation loss of manganese compared with oxidation loss from high carbon ferromanganese in a 2-ton AOD converter; reprinted with permission [74].

These researchers did not provide details of manganese losses with processing time however, they reported the amount of evaporation loss of manganese as a function of oxidation loss per ton of melt. As seen in Figure 2.22, the evaporation loss of manganese is significant compared to the loss as MnO.

You [75] in another work, carried out the refining of 0.087 ton of Fe-75Mn-7C-0.3Si in a model AOD converter. The oxygen was blown between 0.38 to 1.34 Nm^3/min per ton of metal. Argon was blown at 0.19 to 1.15 Nm^3/min per ton of metal and the mixing ratio of oxygen varied between 0.25 to 0.8. The simultaneous changes of manganese, carbon, and silicon concentration of ferromanganese with time is shown in Figure 2.23. In the initial stage of blowing, the manganese concentration was reported to increase gradually with the blowing time while the decarburization reaction proceeded very quickly with a high carbon concentration. Silicon was mostly oxidized and removed at the initial stage of blowing.

Manganese begins to decrease from around 30 minutes. When the composition of molten metal reached about 2%C and 0.1% Si, manganese loss was initiated, the decarburization rate decreased and the manganese oxidation reaction proceeded preferentially, resulting in a rapid manganese loss. Although the decarburization to less than 0.5%C was done successfully, the manganese loss was about 15% manganese loss by end of blowing.

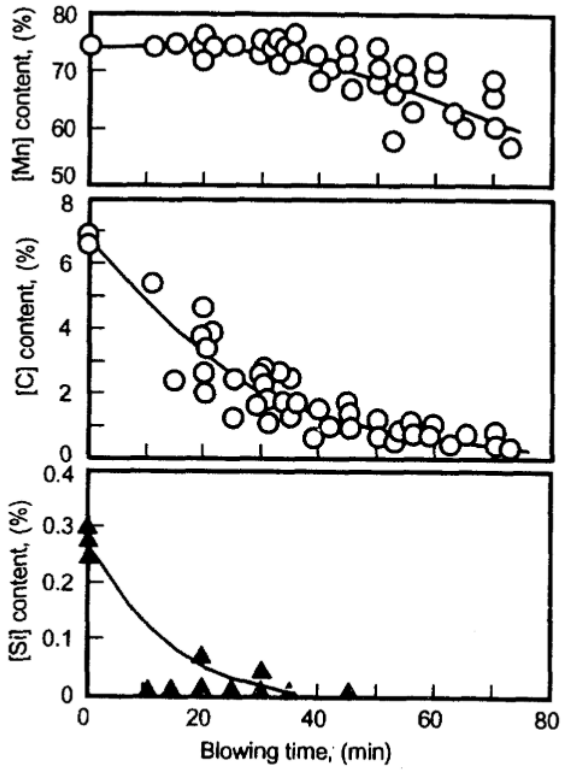

Figure 2.23. The variations of Mn, C, and Si concentrations in the bath with time for AOD processing of 0.087-ton high carbon ferromanganese; reprinted with permission [75].

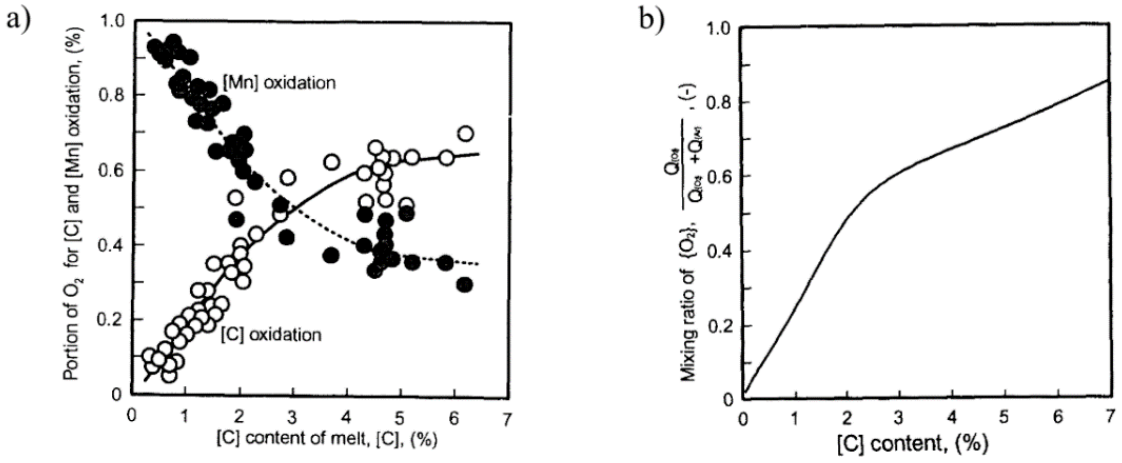

Figure 2.24 a) The oxygen consumption for the oxidation of carbon and manganese versus carbon concentration in the melt, b) mixing ratio of oxygen versus carbon concentration of melt; reprinted with permission [75].

Figure 2.24 (a) shows the oxygen consumption for decarburization and oxidation of manganese in the work by You [75] assuming the products of oxidation reactions are CO and MnO. In the early stage of the blow, at high carbon concentrations, the portion of oxygen consumed for the decarburization was about 0.6 and it decreased almost linearly with the decreasing carbon concentration of the melt. The oxygen utilization for the manganese oxidation increased rapidly. Based on this oxygen utilization data and several regression analyses You derived an empirical equation to quantitatively express the relation between the oxygen mixing ratio and carbon concentration required to promote the decarburization reaction while suppressing manganese oxidation. The result of his analysis is illustrated in Figure 2.24 (b) showing that the oxygen mixing ratio should be decreased from 0.8 for 7% C in the bath to 0.6 for about 3%C and thereafter it should be decreased rapidly for the lower carbon concentrations. In this specific work, he did not provide data about manganese losses by evaporation.

2.3.6 Effect of Slag Basicity

Figure 2.25 shows the effect of basicity $\left(\text{ratio of } \frac{\%\,CaO+\%MgO}{\%SiO_2}\right)$ on oxidation loss of manganese for different temperatures from You *et al.* [74] The amount of MnO in the slag initially decreased with increasing basicity and reached a minimum at basicity of 1.5. Thereafter, increasing basicity led to higher MnO in the slag. As seen, increasing temperature led to slightly higher manganese loss to the slag. These workers recommended keeping the basicity of the slag close to 1.5 and avoid high temperatures to refine ferromanganese economically with minimum losses. This agrees with Dresler's [64] findings for manganese recovery from slag that low basicity favored the higher reclamation of manganese from slag, however, this could only be realized at the expense of damage to the refractories.

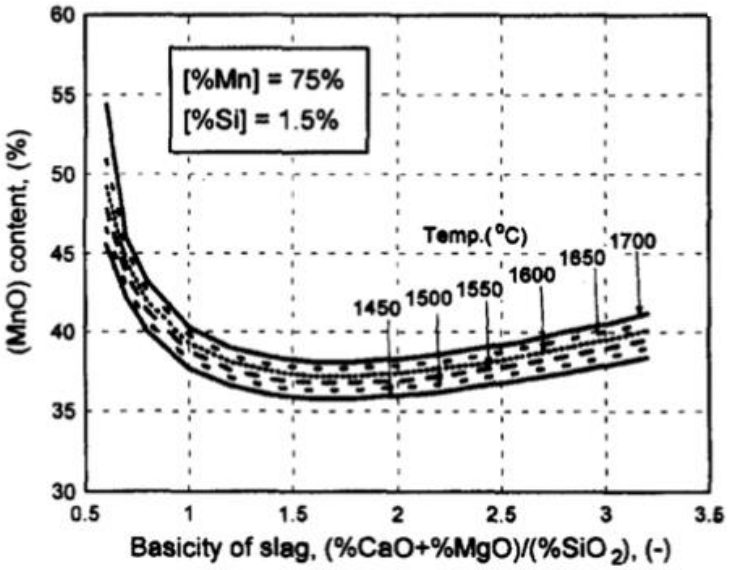

Figure 2.25 The oxidation loss of manganese into slag versus slag basicity for various melt temperatures; reprinted with permission [74].

2.3.7 Effect of Blowing Method

Yamamoto *et al*. [76] investigated the decarburization and manganese losses of high carbon ferromanganese (Fe-76Mn-7C) in a 500 kg combined blowing converter for three different methods of oxygen blowing; Top oxygen blowing, top oxygen blowing with bottom argon stirring, and combined blowing (top oxygen blowing and argon-oxygen injecting from tuyere). These researchers observed a three-stage pattern for manganese loss with processing time (Figure 2.26 (a-c)). Initially, a stage of demanganization, followed by a reversion stage, and a rapid demanganization in the final stage. The carbon concentration pattern with time was similar to that of work by You *et al.* [74]. Initially, the rate of decarburization was slow, then it increased with a constant rate, and finally, the rate dropped with decreasing carbon concentration in the bath. Figure 2.26 (d) shows the temperature of melt increased from 1600 K up to 2100 K after 40 minutes of blowing. Although these workers did not discuss the mechanism of reversion, if one compares the decarburization data with that for demanganization it can be seen that the loss of steel mass by decarburization is sufficient to account for the observed increase in manganese concentration. For example, in Figure 2.26 (c) in the first stage (t= 0 to 4 min), 0.5 wt% of C and 0.5 wt% Mn is removed from melt. Therefore, the mass of steel will be decreased from 500 to 495 kg. In the second stage (t= 4 to 24 min), approximately 5wt% carbon is removed, which means the mass of alloy will be 470 kg due to the carbon loss. At the same time, the concentration of manganese increased by 3.2% (from 76 to 78.5wt%). The initial mass of Mn is 0.76*495kg = 376 kg, and at the end of stage 2, if assumed it is not reacted

it will be 376 kg which is equivalent to 80 wt% Mn. This calculated value is slightly higher than the observed manganese concentration in the bath. This shows that there is some manganese loss in the second stage which agrees with Figure 2.28 that shows the rate of total manganese loss during the second stage is between 1 to 3 kg/min; which is not oxidation loss, but evaporation.

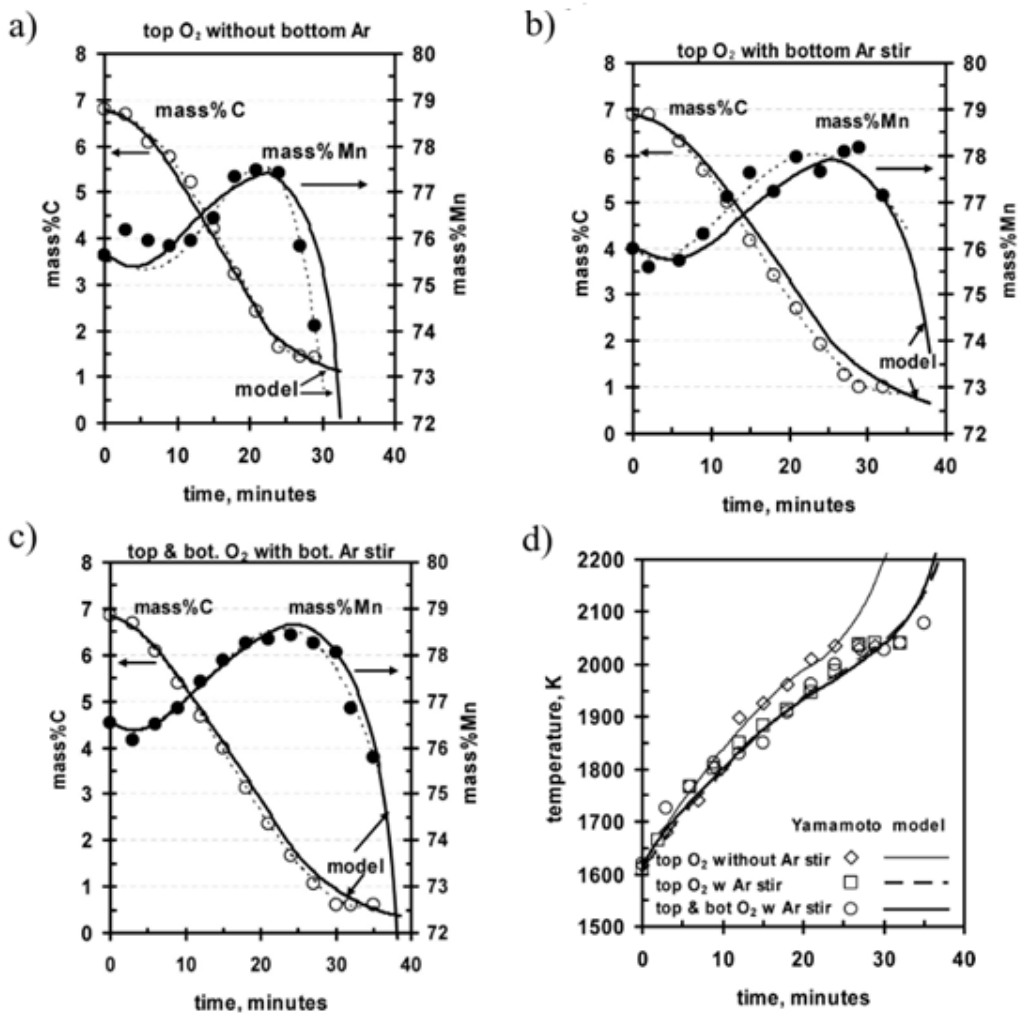

Figure 2.26 Carbon and manganese concentrations in bath versus time for a) top oxygen blowing without bottom Ar stirring, b) top oxygen blowing with bottom argon stirring, and c) top and bottom oxygen blowing and bottom argon-stirring, and d) the measured temperature of melt with time; reprinted with permission [77].

It was reported that manganese loss was due to oxidation and evaporation, and the XRD patterns of dust mainly consisted of Mn_3O_4. Their calculated evaporative loss of manganese based on the weight of collected dust was 0.11 $\frac{g}{cm.s}$ which was close to the theoretical rate of manganese evaporation in vacuum $\left(0.15\ \frac{g}{cm.s}\right)$ assuming that the temperature was 2000 K. Therefore, they proposed that manganese evaporates and form MnO in the furnace and it was oxidized to Mn_3O_4 at the mouth of the furnace. They did not further elaborate on the analysis of findings, kinetically, or thermodynamically. Lee *et al*.[77] proposed that the decarburization of high carbon ferromanganese in Yamamoto's work was controlled by three mechanisms. In the first stage, when carbon concentration was in the range of 7% down to 6%, the chemical reaction was controlling the rate of decarburization. In the middle stage, for the carbon concentrations down to 2%, mass transfer of oxygen in the gas phase controlled, and for carbon levels lower than 2% mass transfer of carbon in the liquid phase was controlling the rate.

For stage 3 of the process, they determined the mass transfer coefficient of carbon using Equation 2.20 and decarburization data from Figure 2.26 (a-c). A was the interfacial area in m^2, k_C was the mass transfer coefficient of carbon in m/min, ρ was the density of molten ferromanganese in (kg/m^3), and W was the mass of ferromanganese in kg. The carbon concentration at time t and at equilibrium were respectively labeled %C, and $\%C_e$, the latter was assumed to be zero. For top oxygen blowing, the interfacial area was considered to be the surface area of the converter, 0.28 m^2 although this is likely to be an underestimate as some deformation of the surface by the jet is expected. The top-oxygen was blown at a flow

rate of 1.58 m^3/min from a single nozzle lance with a throat diameter of 5 mm. This gives the gas velocity of 1345 m/s and Mach number 3. The strike of a supersonic jet with a metal surface creates droplets which significantly increase the surface area of reactions [78]. According to Molloy [79], there are three modes of cavity formation: dimpling, splashing, and penetration. These modes are influenced by lance height, lance angle, and gas flow rate [80]. As reported by Alam *et al*.[81] the rate of droplet generation increases with lance height in penetration mode until further increasing lance heigh transforms the mode to splashing and the rate of droplet generation reaches a maximum. Based on this, assuming a flat surface for the top blowing configuration seems unrealistic. (Any increase after a certain point leads to the decreasing of jet momentum and consequently the rate of droplet generation.)

In the case of injection through bottom tuyeres, reactions would have taken place at the interface between gas bubbles and metal. The difference between the rates of decarburization for the top oxygen blowing with bottom oxygen injection and only top oxygen blowing was used to determine the interfacial area of bubbles which gives 0.049 m^2.

$$\frac{d\%C}{dt} = -Ak_C \frac{\rho}{W}(\%C - \%C_e) \tag{2.20}$$

The determined mass transfer coefficients of carbon in stage 3 were 0.021, 0.026, and 0.0283 m/min respectively, for top oxygen blowing, top oxygen and bottom argon stirring, and top oxygen blowing with bottom argon and oxygen injection. These values are presented in Figure 2.27. These researchers attributed the higher mass transfer coefficients

of carbon in the case of combined blowing to the improved mixing intensity of metal by bottom gas injection. It can be seen that the effect of blowing mode on the results of decarburization are the same as AOD refining of stainless steel as

shown in Figure 2.12.

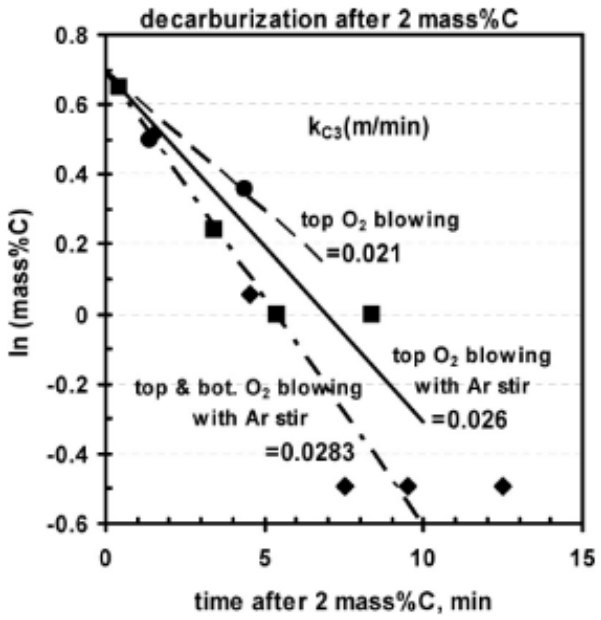

Figure 2.27 Mass transfer coefficient of carbon in stage 3 for different blowing methods; reprinted with permission [77].

Lee *et al*. [77] stated that the excess oxygen which was not consumed for the CO formation was not sufficient to justify the total observed manganese loss as Mn_3O_4. These workers proposed that manganese was removed from the melt as vapor, some of which was oxidized to MnO at a short distance above the surface of melt by a mechanism similar to fuming proposed by Turkdogan *et al*. [82] and MnO oxidized to Mn_3O_4 at the entrance of the converter. The pattern of total manganese loss and oxidation loss with processing time for each blowing method is provided in Figure 2.28. Total manganese losses shown in Figure

2.26 increased with blowing configuration in the order of top blown oxygen with bottom argon blowing, combined blowing with top oxygen and bottom argon and oxygen, to only top oxygen blowing. Hence, the behavior of Mn and Cr during different blowing methods in the argon-oxygen refining process is similar (compare with Figure 2.12).

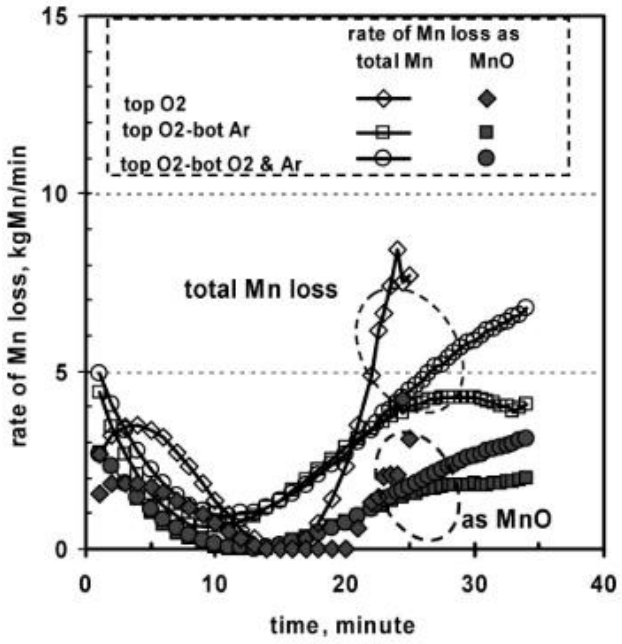

Figure 2.28 Rates of total manganese loss and oxidation loss as MnO time for three different blowing methods; reprinted with permission [77].

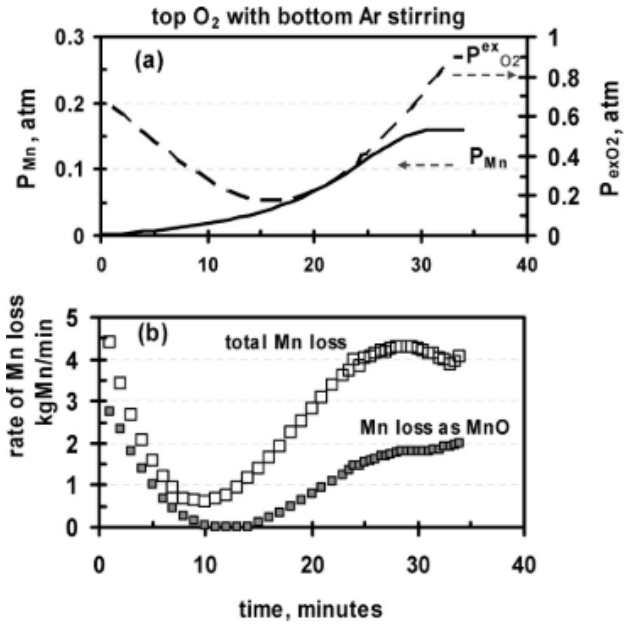

Figure 2.29 a) The vapor pressure of manganese and partial pressure of excess oxygen, and b) rates of total manganese loss and loss as MnO versus time for top oxygen blowing and bottom argon stirring; reprinted with permission [77].

Figure 2.29 (a) shows the variations of the vapor pressure of manganese (p_{Mn}) and partial pressure of excess oxygen ($p_{ex\,O_2}$) with time for top oxygen blowing and bottom argon stirring calculated by Lee *et al.* [77]. p_{Mn} at the gas-metal interface was calculated from the equilibrium constant of Equation (4.) and it increased with time due to the temperature rise of ferromanganese during the process. As observed in Figure 2.29 (b), the trend of manganese loss with time was decreasing until reaching a minimum during the first stage, it then increased with time as expected from the exothermic heating leading to the increased vapor pressure of manganese. The total manganese loss and loss as-MnO increased and decreased with the partial pressure of excess oxygen (Figure 2.29), implying that the excess

oxygen which was not consumed for CO formation governed the dynamics of manganese loss in the gas phase near the gas-metal interface.

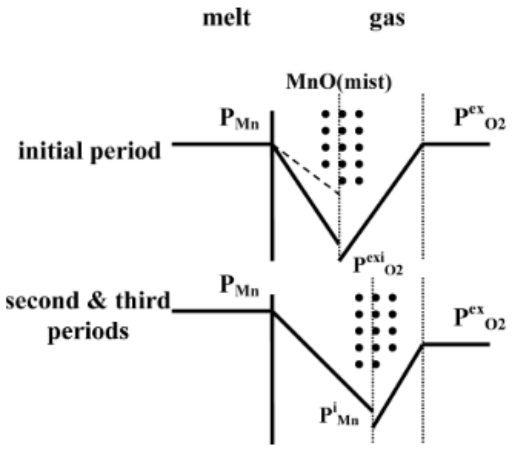

Figure 2.30 Th counter-diffusion of manganese vapor and excess oxygen in the gas phase; reprinted with permission [77].

As explained earlier, Lee *et al.* [77] suggested that manganese vapor reacts with oxygen to form MnO according to the fuming model by Turkdogan *et al.* [82]. In Figure 2.30 the counter diffusion of manganese vapor and excess oxygen for each stage of the process is shown schematically. It was proposed that manganese vapor reacts with oxygen beyond the surface of the metal and therefore a sink is created. The vapor pressure of manganese at the gas-metal interface and excess oxygen in the gas phase determines the thickness of the boundary layer for manganese vaporization. In the first stage, manganese vapor pressure was low and excess oxygen was high, therefore the reaction plane for MnO mist formation moved towards the metal surface. Consequently, the thickness of the layer was small and the concentration gradient of manganese was steep which led to enhanced vaporization until the oxidation at the surface of metal occurred and stopped the vaporization. The flux

of excess oxygen (left over from CO formation) was controlling the rate of manganese loss in the first stage (within the first 10 minutes where Mn concentration reached a minimum). In the second (until to the point where Mn concentration increased to a maximum) and third stage (where Mn concentration decreased again) the rate of the mass transfer of manganese vapor controlled the evaporation of manganese. As the counter fluxes of manganese and oxygen have to balanced, with increasing manganese vapor pressure and depletion of oxygen with time the reaction plane moved away from metal during the second and third stages.

Nell *et al*. [83] developed a model based on heat and mass balance using Metsim software for the oxygen refining of high carbon ferromanganese and validated it with data from a 6-ton AOD vessel. The top oxygen was blown at the flow rate of 20 Nm^3/min and a mixture of oxygen and steam at a total flow rate of 13.5 Nm^3/min (at a reducing flowrate with time) was injected from the bottom. At about 22 minutes Fe-Si and lime were added to the melt along with argon blowing, to reduce MnO from slag and bring back manganese into the melt. The variations of carbon, manganese, and silicon with blowing time are presented in Figure 2.31. As seen, trends of carbon and manganese concentrations versus time until 25 minutes in their study were similar to the work of Yamamoto *et al.* [76]. It was reported that increasing the top oxygen blowing enhanced the rate of decarburization at the expense of losing more manganese by evaporation associated with the raised temperature.

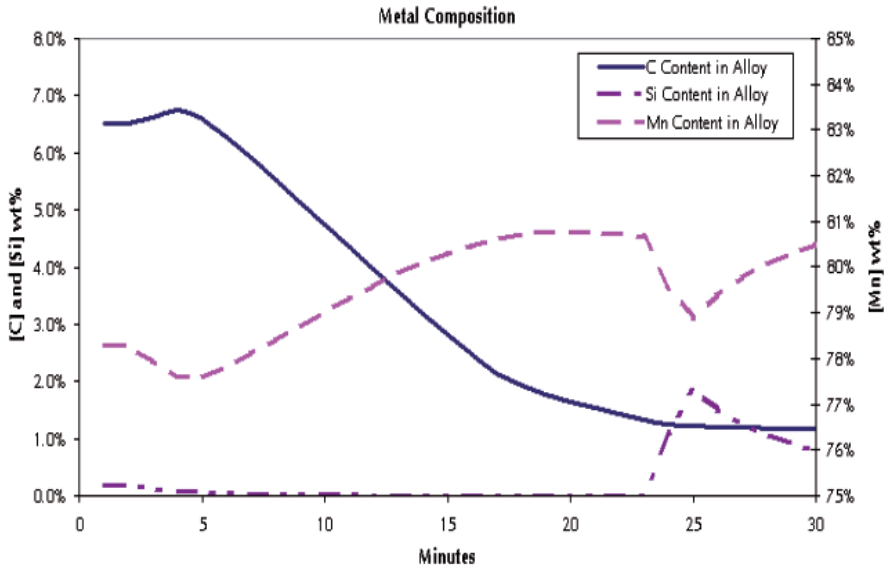

Figure 2.31 The simultaneous variations of carbon, manganese, and silicon concentration with time in a study by Nell *et al*. reprinted with permission [83].

2.3.8 Effect of CO_2 Addition into Blown Gas

Figure 2.32 (a-d) displays the result of decarburization and manganese loss in work done by Liu *et al.* [84] to study the CO_2-O_2 injection into Fe-16Mn-3C melts at 1550℃. Figure 2.32 (a) and Figure 2.32 (b) show the effect of gas composition on the rate of decarburization and manganese loss, respectively. The total gas flow rate was 500 ml/min. The rate of decarburization increased in the order of pure O_2, O_2-25% CO_2, to the O_2-50% CO_2 (Figure 2.32 (a)). This was attributed to the better stirring of melt and transfer of carbon to the interface of gas-metal by twice as much gas being produced per mole of carbon in decarburization by CO_2 (Equation 2.21) compared with the decarburization by oxygen (Equation (2.1)).

$$C + CO_2 = 2CO \qquad \Delta G^0(J) = 166560 - 171T \text{ [29]} \qquad (2.21)$$

Figure 2.32 (b) shows that for pure O_2 injection, manganese concentration decreased linearly until 20 minutes of process, then it continued at a faster rate until the end of the experiment. In this case, the final manganese content was 2.05%. By introducing 25 and 50% CO_2 into the injected gas, the manganese concentration decreased almost linearly until the end of experiments and final compositions were 4.89, and 8.08% Mn in the melt. This indicates that CO_2 addition was effective to avoid excessive manganese loss and consequently for the retention of manganese in the bath. It was not explained why the rate of manganese loss was the same for pure O_2 and O_2-25 vol.%CO_2 during the first stage.

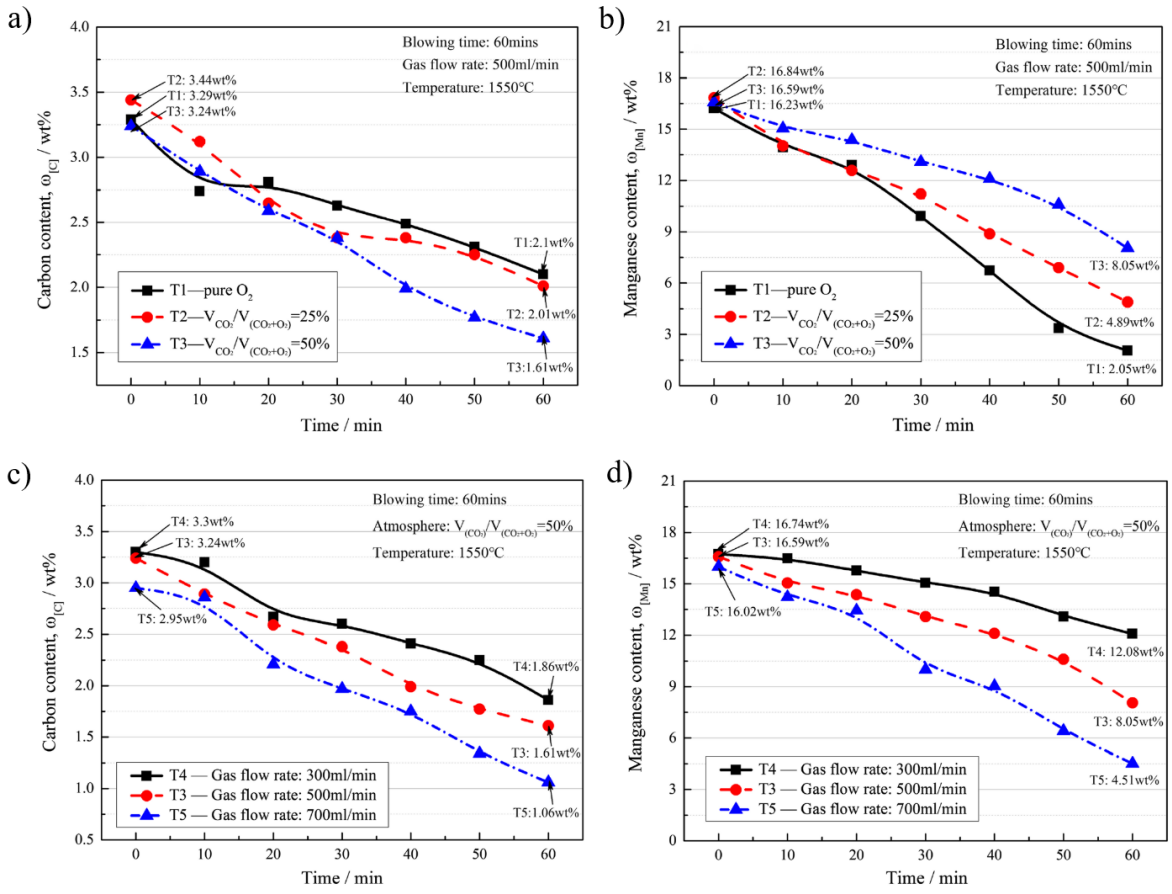

Figure 2.32 Variation of a) carbon concentration and b) manganese concentration versus time, variable: gas composition, and Variation of c) carbon concentration and d) manganese concentration versus time, variable: gas flow rate in study by Liu *et al*. reprinted with permission [84].

Liu *et al.* [84] have also shown that the rate of decarburization and manganese loss increased with the total flow rate as shown in Figure 2.32 (c) and Figure 2.32 (d). Although the flow rate of 700 ml/min was the most efficient case for the decarburization, it led to the highest manganese loss. Another thing that can be seen in these figures is that manganese loss is not taking place at a constant rate during the experiments. This is more evident for the flow rate of 700ml/min (see Figure 2.32 (d)). However, they did not explain the rates with time.

These researchers also studied the effect of temperature on the decarburization and manganese loss at a total flow rate of 300 ml/min and gas composition of O_2-50% CO_2. Figure 2.33 (a) compares the rate of decarburization at 1500 and 1550℃. Within the first 10 minutes, temperature rise did not make any changes, however, the rate of decarburization increased afterward. The increased rate of decarburization at higher temperatures was because decarburization by CO_2 (Equation 2.21) is endothermic and higher temperature promotes this reaction.

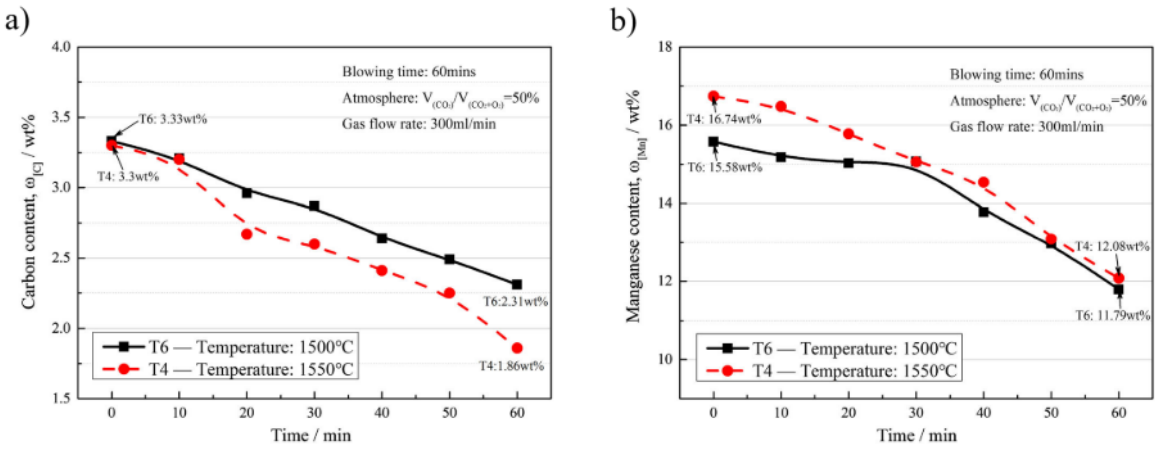

Figure 2.33 Variation of a) carbon concentration and b) manganese concentration versus time, variable: melt temperature; reprinted with permission [84].

The corresponding manganese concentrations are shown in Figure 2.33 (b). The initial manganese concentrations for 1550℃ was 16.74% whereas for 1500℃ it was 15.58%. There was a two-stage pattern manganese loss where initially manganese loss was slow and then the rate increased. This group of researchers did not present mass balance calculations, nor did they suggest a mechanism for manganese loss. They suffice to accepted that

manganese loss was due to a combination of evaporation and oxidation according to literature and thermodynamic calculations.

2.3.9 Mn Loss during AOD Refining of Stainless Steel

Wei *et al*. [85,86] developed a mathematical reaction model for AOD refining of stainless steels during combined top and side blowing. It was assumed that all elements in the liquid phase are equally available and they are selectively oxidized based on their affinity for reaction with oxygen. Their model was validated with industrial heats with good agreement. The variation of carbon, chromium, manganese, and silicon contents in the bath and melt temperature with time during AOD refining of 18.8-ton of stainless steel is provided in Figure 2.34. As seen, the concentration of carbon, chromium, silicon, and manganese decreased at various rates during the first stage of the process. The rate of oxidation of silicon was very fast and x_{Si} approached zero at 700 seconds. Similarly, oxidation of manganese took place at a very fast rate but plateaued at 700 seconds, and where oxygen supply was balanced consumption to form CO and Cr_2O_3. Bath temperatures increased and consequently the rate of decarburization increased while the rate of chromium oxidation decreased slowly. The rate of oxidation of chromium and carbon increased when manganese and silicon were not competing for oxygen. Bath temperature decreased for a short time due to the addition of alloying elements such as high carbon ferrochromium which led to a small extent of increasing chromium and carbon concentrations. The carbon and chromium content continuously decreased and resulted in an increase in bath temperature due to their oxidation reactions. The carbon concentration

decreased slowly and chromium concentration decreased at an increasing rate after the critical carbon concentration was reached.

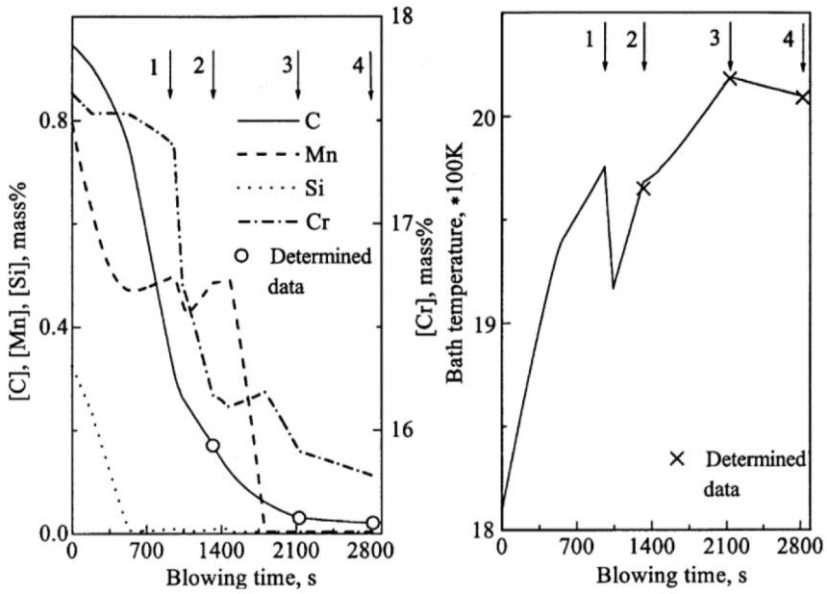

Figure 2.34 Predicted variation of carbon, chromium, manganese, and silicon contents in the bath and melt temperature with time during AOD refining of 18.8-ton stainless steel; 1: adding alloying agents or scrap, and 2, 3, and 4 correspond to the end of blowing period I, II, and III, reprinted with permission [86].

2.4 Summary

The argon-oxygen decarburization of stainless steels has been researched extensively mathematically and experimentally. In contrast, there are only a few studies about the argon-oxygen refining of high carbon ferromanganese as discussed above. Generally, the refining of stainless steels and high manganese alloys in the AOD converter is similar in many aspects. For instance, combined blowing increased the rate of decarburization and decreased metallic losses of both Cr and Mn containing alloys compared to top blowing as shown by Tsujino *et al.* [53] and Lee *et al.* [77]. Another similarity is that the decarburization

to low carbon concentrations requires lowering the partial pressure of CO with argon dilution. It has been shown by Dennis *et al*. [34], Fruehan [31], and Ohno *et al*. [50] for Cr containing steels and similarly was observed by You *et al*. [72,73] for high carbon ferromanganese alloys. Additionally, for both groups of alloys, it is recommended to avoid prolonged high temperatures as this will cause excessive manganese evaporation and severe damage to converter refractories in both cases [40,57].

You *et al*. [72–75] presented experimental and trial data from decarburization and demanganization of high carbon ferromanganese during the argon oxygen refining process. It was stated that the total manganese loss was due to the oxidation and evaporation, however, the contribution of each loss at a different stage of the process was not determined. They developed some empirical equations to explain the importance of oxygen and inert gas flow rates in top lance and bottom tuyeres. However, no kinetic model for the decarburization and manganese losses was proposed. Lee *et al*. [77] presented the only kinetic model in the literature for the decarburization and manganese losses from ferromanganese at each stage of the process. It was proposed that the rate of decarburization was controlled by a chemical reaction at the gas-metal interface in the first stage, by oxygen supply in the second stage, and by mass transfer of carbon in the liquid phase in the third stage [77]. During the first stage, the rate of decarburization was slow, and the melt temperature increased from about 1620 to 1820 K due to the oxidation of manganese. In the second stage, the rate of decarburization increased considerably while there was no manganese loss, and melt temperature increased from 1820 to 1920 K. In the third stage,

the rate of decarburization slowed down with decreasing carbon content in the melt, and manganese loss started at a high rate. In this stage, the temperature increased up to 2100 K. Lee *et al*. [77] proposed that evaporation of manganese is responsible for the total manganese loss and the excess oxygen after CO formation is consumed for oxidation of manganese to MnO. They pointed to the manganese loss in the second and third stages together. However, they did not explain the increasing manganese loss in the second stage.

The three-stage pattern for manganese and carbon in argon oxygen refining of high carbon ferromanganese is a common feature in the reported data in the literature [73,75–77,83,87]. Among those studies in which mechanisms of manganese loss were discussed, it was accepted that manganese loss was due to oxidation and evaporation.

As discussed, the available data in the literature is focused on the refining of high carbon ferromanganese to medium and low carbon contents. Based on the foregoing literature review, there is a need for a clear understanding of the mechanism of decarburization and manganese losses from high manganese steels in lower range manganese and carbon during the argon-oxygen decarburization process. The objective of the current work is to quantify the simultaneous decarburization and manganese losses during Ar-O_2 bubbling of high manganese steels. Additionally, to determine the contribution of each mechanism of manganese loss during different stages of the process. It should be noted that the aim of this work is not to simulate the AOD process. The primary objective of the current work is to explore the mechanism responsible for manganese and carbon removal from high manganese steel. The research will investigate the decarburization and manganese losses

under various temperature, gas composition, total gas flow rate, depth of lance submergence, and alloy composition. The results will determine how oxygen is distributed between carbon and manganese. The effect of the depth of submergence will be investigated to understand if the residence time of bubbles will affect the rate of reaction. Furthermore, the role of the vapor pressure of manganese at the elevated temperatures in evaporative manganese losses will be investigated and a mechanism will be proposed to explain the manganese losses during the process.

Chapter 3

3 Argon–Oxygen Decarburization of High-Manganese Steels: Effect of Alloy Composition

In Chapter 3, all of the experiments and initial analysis of data were carried out by me. Dr. Kenneth S. Coley and Dr. Gordon A. Irons shared the analysis of the data and offered the idea of the evaporation-condensation mechanism. The manuscript was initially drafted by me, edited, and revised by Dr. Kenneth S. Coley, and reviewed to the final version by Dr. Gordon A. Irons. This chapter has been published in steel research international. 2020, DOI: 10.1002/srin.202000480. The following Chapter is the pre-publication version of the article.

Abstract

The kinetics of simultaneous decarburization and demanganization of Fe–Mn–C alloys with 5–25% Mn and 0.05–0.42% C are investigated by bubbling a mixture of Ar–O_2 through the melt at 1823 K. There are three distinct stages during the process. In stage 1, the rate of decarburization is slow, it is faster in stage 2, and slows to an intermediate rate during stage 3. In stage 1, manganese concentration decreases at a constant rate. In stage 2, manganese concentration remains essentially constant or exhibits minor reversion in some cases. In stage 3, manganese concentration decreases again. The overall rate of manganese loss in stage 1 increases with decreasing initial carbon concentration of the alloy, whereas in stage 3, the rate of manganese loss is independent of carbon concentration. The rate of overall manganese loss is partly controlled by the transport of manganese in the

liquid phase. Assuming the products of reaction are CO and MnO, the combination of loss as vapor and oxide is insufficient to justify the total Manganese loss. The mechanism for the extra manganese loss is proposed to be due to evaporation–condensation of manganese in the bubble, is supported both thermodynamically and kinetically.

3.1 Introduction

Manganese is an important alloying element in the second and third generation of Advanced High Strength Steels (AHSS) with 2-25%Mn [1-4]. Manganese Oxygen Refining (MOR) which is basically similar to the BOF has been used since 1976 for the refining of high carbon ferromanganese (HCFeMn) to medium carbon ferromanganese (MCFeMn). However, as higher temperature is required for MOR (>1750℃) compared to BOF, further decarburization to the lower range would be at the expense of excessive manganese evaporation and oxidation; [5,6] as Dresler [7] reported, a 0.2% decrease in carbon concentration resulted in a 10% manganese loss. The demand for low carbon high manganese steels made Argon Oxygen Decarburization (AOD) a potential candidate for the production of these grades of steels [8,9]. Since AOD was commercialized in the 1970s, it has been used extensively to produce stainless steel and it has the ability to decarburize the steel to very low levels. There are numerous studies on the behavior of chromium in the stainless steel with the AOD process which have been reviewed by Visuri [10]. In contrast, there are only a few studies in the literature regarding the argon-oxygen processing of high carbon ferromanganese which will be briefly reviewed here. Yamamoto *et al*. [9] studied the refining of high carbon ferromanganese in a 500 kg combined blowing

converter with a top lance for blowing oxygen and a bottom plug for blowing a mixture of argon and oxygen. These workers observed three stages of manganese removal: an initial stage of demanganization, a reversion stage, and finally a rapid demanganization stage. They attributed the manganese loss to both oxidation and evaporation, but they did not investigate the kinetics of reactions, and no explanation for the rise in manganese concentration in stage 2 was offered. Lee *et al*. [11] analyzed Yamamoto's results and proposed that the rate of decarburization of ferromanganese is controlled by chemical reaction initially, by mass transfer of oxygen in the gas phase, and by mass transfer of carbon in the liquid phase finally. These workers proposed that CO formation did not consume all of the oxygen and the excess enhanced the manganese evaporation and MnO fume formation based on the mechanism proposed by Turkdogan *et al*. [12]. They modeled the decarburization and manganese loss separately which seems inconsistent with the competition between the two processes implied by their proposed mechanism.

You *et al*. [13] investigated the decarburization of high carbon ferromanganese (75%Mn-7%C-0.3%Si) by blowing an argon-oxygen mixture onto the melt. During the early part of their experiment, there was no manganese loss. After the oxidation of Si was over, manganese loss started and decarburization slowed down. It appears that silicon and manganese compete for oxygen. It is expected that heat generated from silicon oxidation would enhance manganese evaporation. However, the contribution of the evaporative loss of manganese was not discussed. They developed an empirical equation to describe the correlation between carbon and manganese oxidation in which the ratio of $O_2/(Ar + O_2)$

was an important factor. In another work, You *et al.* [14] reported that between 5 to 25% of manganese was lost due to oxidation into slag and vaporization to fume during the decarburization of high carbon ferromanganese in a 2-ton converter. However, they did not present the rate of manganese oxidation or evaporation at each stage of the blowing process. These workers defined an apparent vaporization coefficient, β (Equation 3.1) for the manganese loss that was inversely related to the carbon concentration in the melt.

$$\beta = 10^{4.776} \frac{\left(\frac{Q_{O_2(B)}}{Q_{O_2(B)}+Q_{inert(B)}}\right)^{2.604}\left(\frac{Q_{O_2(T)}}{Q_{O_2(T)}+Q_{O_2(B)}}\right)^{1.811}}{[\%C]^{0.608}} \quad (3.1)$$

Q_{O_2}, Q_{inert} are the flow rates of oxygen and inert gas, respectively. The subscript B and T indicate bottom and top blowing. These workers suggested minimizing the oxygen concentration in the top and bottom gas and avoiding high temperatures and long refining time to prevent evaporative loss of manganese.

Recently, Liu *et al.* [15] have studied the manganese and carbon behavior during O_2-CO_2 blowing of Fe-16% Mn-3% C alloys observing that initially, manganese loss was either slow or negligible, getting faster in the later stages. They found that introduction of CO_2 in the gas mixture was beneficial for decarburization and manganese retention in the bath. However, raising the temperature and flow rate resulted in more manganese loss and faster decarburization.

In summary, past researchers have studied the decarburization and losses of manganese in high carbon ferromanganese during refining with argon-oxygen mixtures. Their findings

show that manganese versus time proceeded in two or three stages with manganese loss occurring in the initial and final stages. There is not a clear explanation for the arrest of demanganization in the middle stage. Also, there is a gap in understanding the mechanism of losses for the concentration lower range of manganese and carbon. The present work is part of a larger study to understand the kinetics of decarburization and manganese losses in the AOD processing of high manganese steels in a wide range of 5 to 25% Mn-0.05 to 0.42% C; which were not tested by past researchers. In this paper, laboratory data for a wide range of conditions are presented, and a working mechanism is proposed to explain the simultaneous changes of carbon and manganese concentrations.

3.2 Experimental Section

3.2.1 Alloy Preparation

The alloys used in this study were prepared by mixing the appropriate amount of 99.977% pure electrolytic iron powder (Alfa Aesar, USA), 99.990% pure manganese flakes (Fisher Scientific, USA), and 99.9999% pure carbon (Alfa Aesar, USA). Immediately before mixing the manganese flakes were acid pickled with a 5% HCl solution to remove a surface oxide layer. Manganese pieces were then dried and weighed for mixing. The total weight of the alloy mixture was 330 grams. The composition of each alloy used in this work is listed in Table 3.1.

Table 3.1 Compositions of the alloy mixtures used in this study.

Alloy (wt%)	Mass C (g)	Mass Mn (g)	Mass Fe (g)
Fe-5Mn-0.42C	1.40	16.53	312
Fe-10Mn-0.42C	1.40	33.30	295
Fe-15Mn-0.42C	1.40	49.55	279
Fe-25Mn-0.42C	1.40	82.60	246
Fe-10Mn-0.18C	0.56	33.30	296
Fe-15Mn-0.18C	0.56	49.55	280
Fe-25Mn-0.18C	0.56	82.60	247
Fe-15Mn-0.05C	0.15	49.55	280
Fe-25Mn-0.05C	0.15	82.60	247

3.2.2 Flow Rate Calibration

Each gas flow rate for argon and oxygen was controlled independently by an electronic gas flow controller. (Alborg, GFCS010409 for Ar and Alborg, GFCS-010584 for O_2). The volumetric flow rate from the gas flow controllers was calibrated using soap bubbles in a graded burette before each experiment. The calibration was checked after each experiment using the same method. In all experiments, a gas mixture of Ar-6.7 vol% O_2 at a total flow rate of 300 Nml min^{-1} (the reference temperature and pressure 273K and 101325 Pa) was injected into the melt.

3.2.3 Procedure

The experimental apparatus used for the current work is shown in Figure 3.1. A vertical tube furnace, heated by molybdenum disilicide elements, was used for all experiments. The

temperature was controlled within ±8 K using a B-type (Pt30Rh-Pt6Rh) thermocouple. Inside the furnace, an alumina tube with an inner diameter of 7.9 cm and a height of 76.2 cm was installed and both its ends were sealed with O-rings and water-cooled stainless steel caps. Gas was injected into the melt through an alumina nozzle which entered the furnace through an O-ring sealed port at the top of the furnace. The gas nozzle was a single bore alumina tube with an outer diameter of 0.48 cm and an inner diameter of 0.16 cm. The slag-free alloy mixture was placed in an alumina crucible with an outer and inner diameter of 4 and 3.8 cm and a height of 9 cm. The crucible was positioned at the centre of the hot zone of the furnace and held in place by a support rod. Then the furnace was sealed and evacuated to 80-150 millitorr, then backfilled with argon and purged for the duration of experiments to avoid oxidation of the liquid metal. The crucible was then heated in the furnace to the target temperature of 1823 K (1550℃) and held at temperature for one hour to homogenize the melt. At this temperature, the system was evacuated and backfilled with argon again. Then the entrance and exit gas were opened and, the nozzle was lowered into the melt to a depth of 3 cm below the surface. A mixture of Ar-6.7 vol.%O_2 was injected for 90 minutes. The argon and oxygen were dried by passing them through silica gel and then through anhydrous calcium sulfate columns. A quartz tube with an outer diameter of 0.7 cm and an inner diameter of 0.5 cm with a pipette controller was used to take the samples at intervals of 10-20 minutes from the onset of bubbling. To avoid backflow of metal into the lance, gas injection was continued during the sampling. The samples were quenched in water and obtained in the form of solid cylinders. The samples were sectioned into smaller pieces of

0.1 g and 1 g for the chemical analysis of manganese and carbon, respectively. Carbon concentrations were analyzed by a combustion method (LECO-CS). Samples of 0.1g obtained from metal were dissolved in 4 ml HCl and 2 ml HNO_3 using a microwave digester and analyzed by Inductively Coupled Plasma Optical Emission Spectrometry (ICP-OES) to measure their manganese concentration.

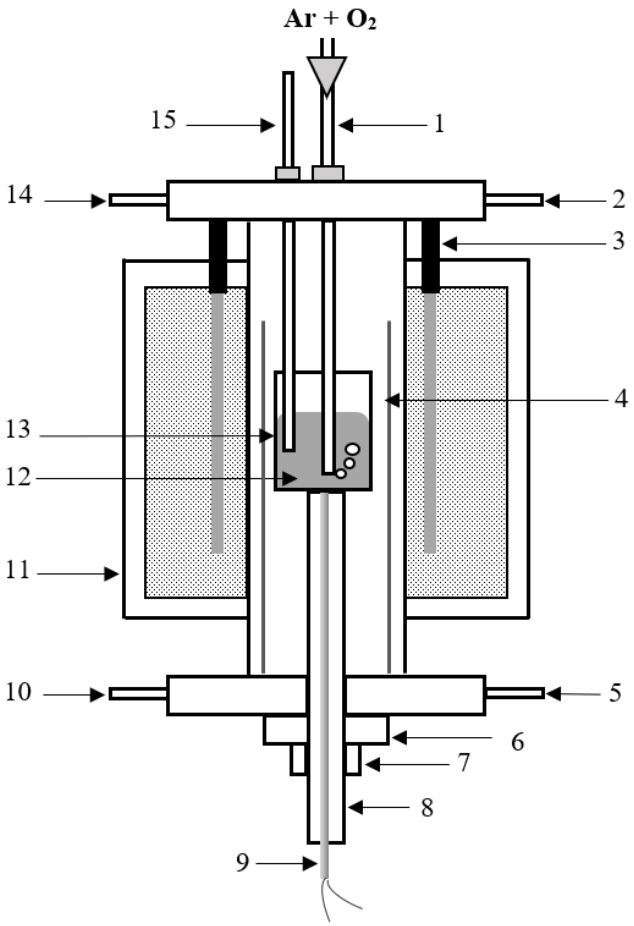

Figure 3.1 Schematic diagram of the experimental setup, not to scale, 1) Nozzle, 2) Water cooling outlet, 3) Furnace heating element, 4) Shield tube, 5) Water cooling 6) Cooling chamber, 7) Rod holder, 8) Support rod/tube, 9) Thermocouple, 10) Gas inlet (Argon purging), 11) Furnace outline, 12) Liquid metal, 13) Alumina crucible, 14) Gas outlet, 15) Sampling tube.

3.3 Results

3.3.1 Demanganization

To examine the effect of carbon and manganese concentration on the rate of demanganization, experiments were carried out with 0.42%, 0.18%, and 0.05% C, and manganese concentrations of 25%, 15%, 10% and 5%. Figure 3.2 (a-c) presents the change in the manganese concentration in the bath with time for different initial manganese and carbon concentrations. Initially, within 10-12 minutes of gas blowing, manganese concentration decreased at an almost constant rate until the reaction ceased. In stage 2 of the process, the manganese remained essentially constant appearing to rise slightly in some cases. The minor increase can be associated with some reversion of MnO in the slag to the metal. This will be discussed in detail in Section 3.4.6. In stage 3, manganese concentration decreased, again at an essentially constant rate. This behavior of manganese is similar to that observed by Yamamoto *et al.* [9] for high carbon ferromanganese (76%Mn-7%C) and Wei *et al.* [16] for stainless steel with 0.8% Mn. Alloy Fe-5%Mn-0.42%C was an exception to this pattern that it did not exhibit measurable manganese loss during the early stages of gas injection. Because the observed behavior is the same as for stages 2 and 3 in all other experiments it is assumed that stage 1 is absent and the stages are labeled 2 and 3. This behavior is similar to that observed by Niiri *et al.* [17] for blowing Ar-CO_2 to the Fe-(0.5-2%) Mn-(1-1.5 %) C alloys and Pehlke *et al.* [18] for the case of blowing CO_2-N_2 to the levitated droplets of Fe-(0.2-0.5%) Mn-2%Si-(1-3%) C alloys.

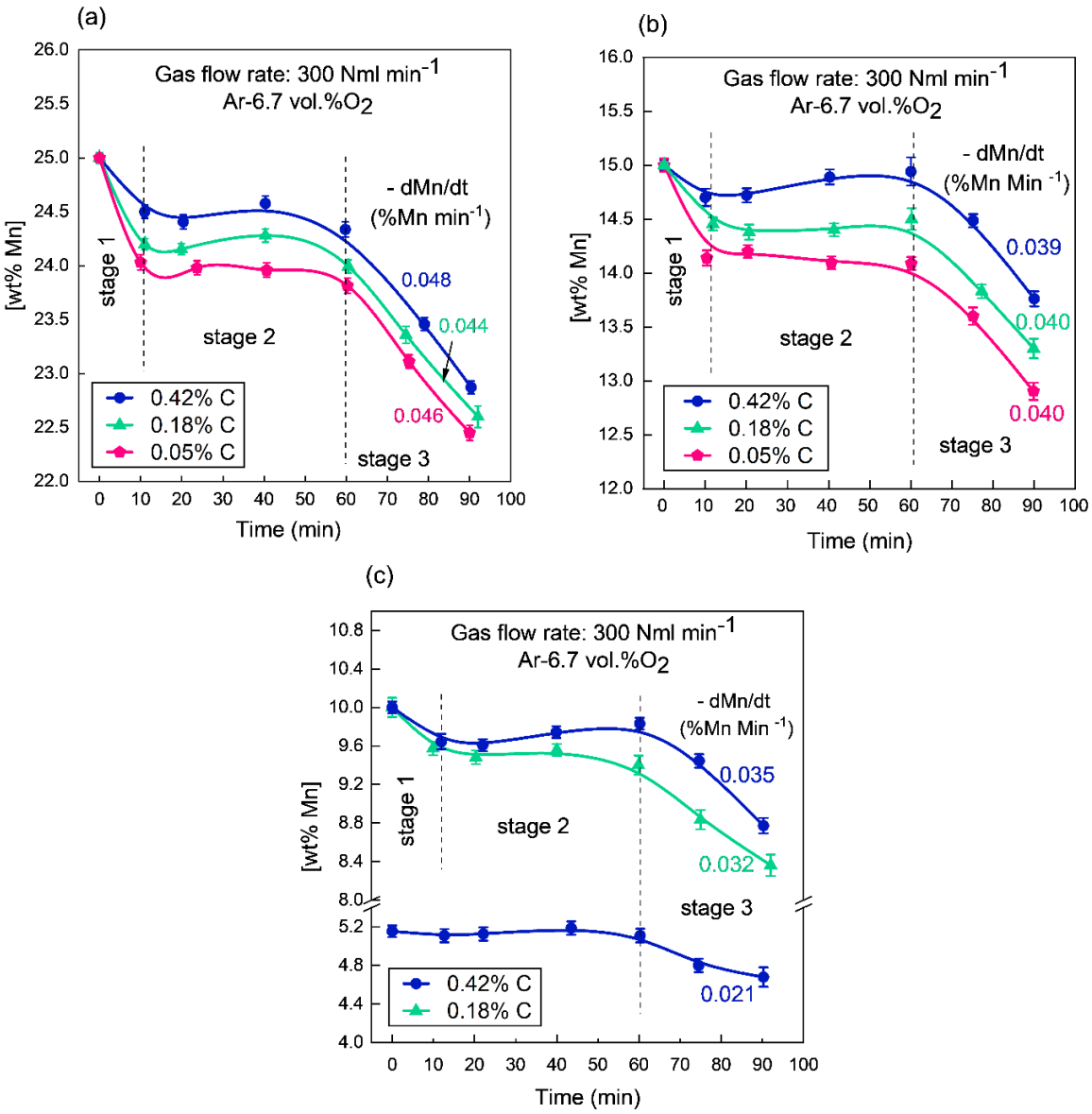

Figure 3.2 Variation of manganese concentration of metal with time at 1823 K for a) Fe-25%Mn, b) Fe-15%Mn, c) Fe-(5 &10%) Mn alloys, Variable carbon concentration.

The measured rates of manganese loss in stages 1 and 3 are summarized in Figure 3.3. In stage 1, the rate of demanganization increased with increasing manganese and decreasing the carbon concentration of the metal. However, in stage 3, the demanganization was only

dependent on the manganese concentration of the alloy. For instance, for alloys with 25%Mn, regardless of their initial carbon concentration, the rate of Mn loss was 0.046 ± 0.002 %Mn min^{-1}.

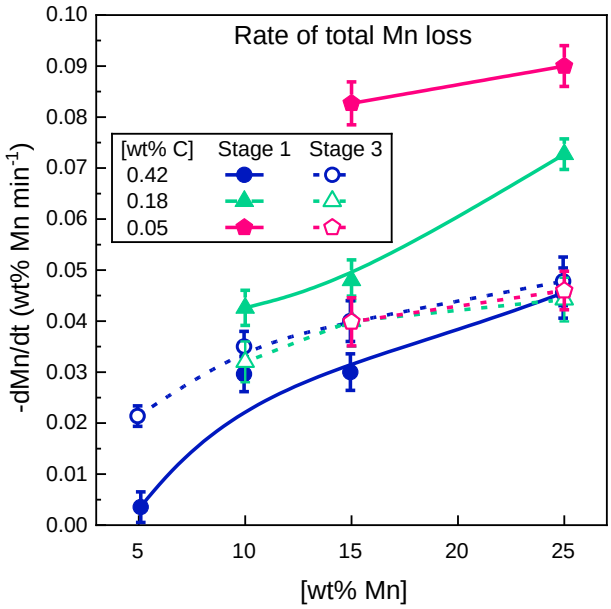

Figure 3.3 Rate of total manganese loss versus initial manganese concentration of the bath, Variable carbon concentration.

3.3.2 Decarburization

Figure 3.4 (a-c) presents the effect of initial manganese concentration on the rate of decarburization of alloys with a starting carbon concentration of 0.42%, 0.18%, and 0.05%. Alloys with the highest manganese content had the lowest rate of decarburization. All the curves follow the same trend. The carbon behavior is similar to the observation of past researchers for the decarburization of high carbon ferromanganese alloys [9,13,19].

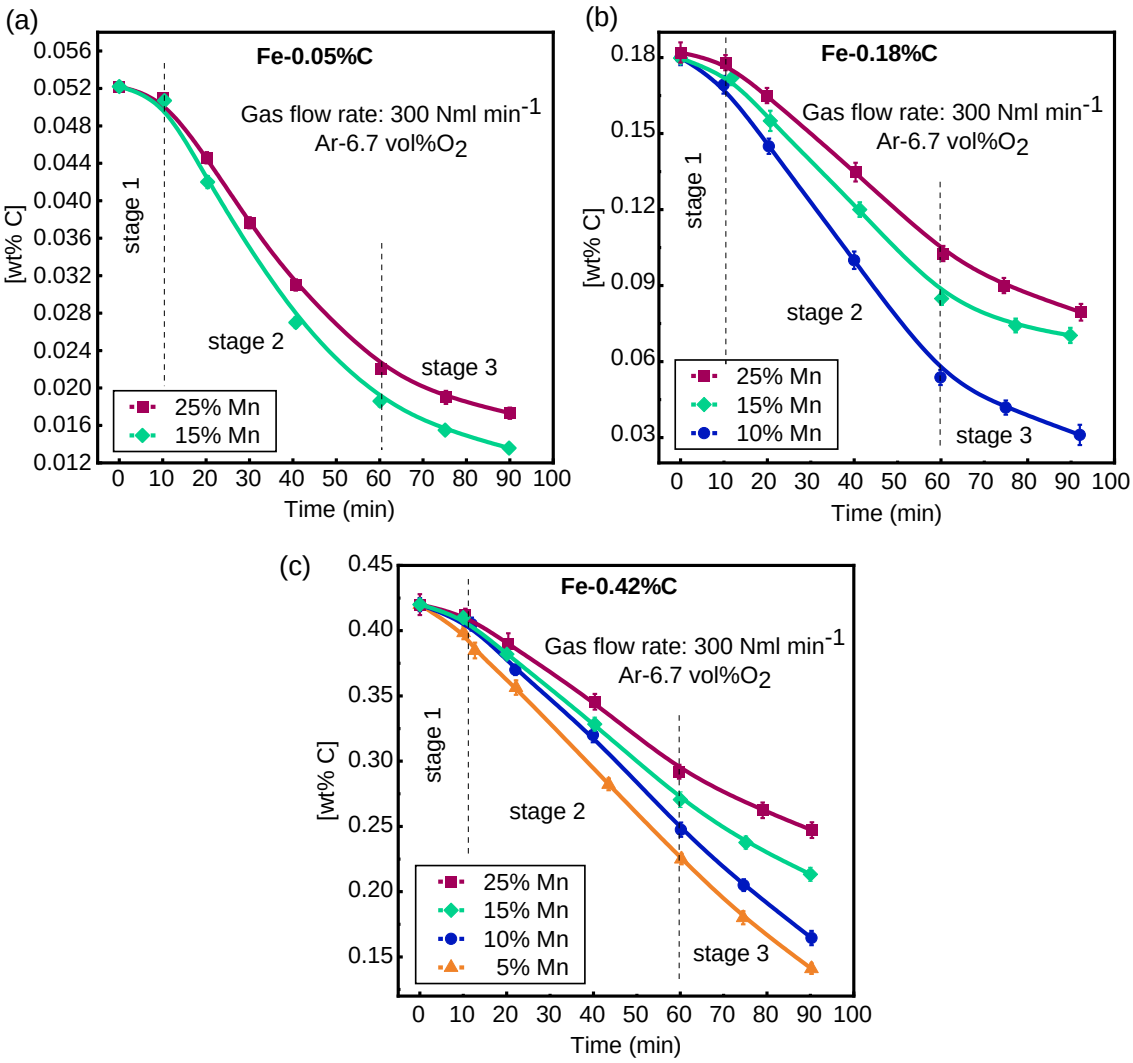

Figure 3.4 Variation of carbon concentration of metal with time at 1823 K for a) Fe-0.05%C, b) Fe-0.18%C, c) Fe-0.42%C alloys, Variable manganese concentration.

The variation of the decarburization rate with time and alloy composition is given in Figure 3.5 (a-c). The rate of decarburization was slow in stage 1, followed by a faster rate in stage 2 and slowed to an intermediate rate in stage 3 with decreasing the carbon level in the bath. For a given carbon concentration, with decreasing the manganese concentration, the rate of

decarburization increased. For a certain manganese concentration, alloys with 0.42% and 0.05% C had the highest and lowest rate of decarburization, respectively.

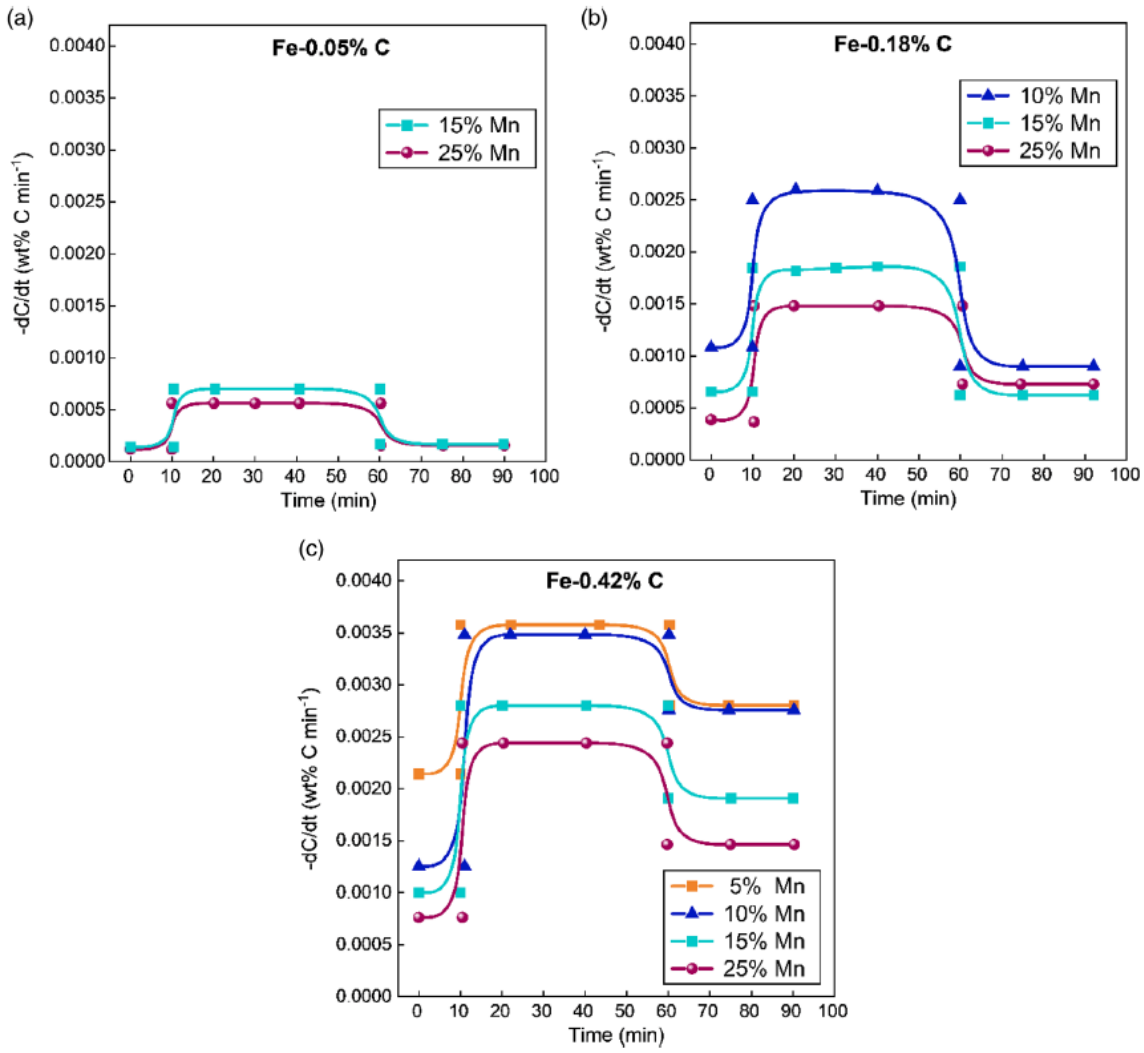

Figure 3.5 Rate of decarburization versus time for a) Fe-0.05%C, b) Fe-0.18%C, c) Fe-0.42%C alloys.

3.4 Discussion

3.4.1 Oxidation of Carbon and Manganese

As oxygen is injected into the liquid steel, the oxidation reactions of dissolved carbon and manganese in the liquid steel takes place and CO and MnO form inside gas bubbles according to the Equations 3.2 and 3.3:

$$C + \frac{1}{2}O_2 = CO \tag{3.2}$$

$$Mn + \frac{1}{2}O_2 = MnO \tag{3.3}$$

The oxygen efficiency for decarburization $\eta_{O_2}^{deC}$ is the ratio of the oxygen that forms CO to the total supplied oxygen. Table 3.2 shows the efficiency of oxygen for decarburization in three stages for each alloy. Alloys with the lowest manganese and highest carbon concentration consumed most of the oxygen for CO formation. It is noticeable that in stage 1, where decarburization was slow, only between 2-36% of supplied oxygen was consumed for decarburization to produce CO. Whereas in the second stage, manganese loss stopped, and the rate of decarburization increased as seen in Figure 3.5. There was a drastic increase in the efficiency of oxygen for decarburization range between 12 to 62%. During stage 3, manganese loss started again, and the competition between carbon and manganese for oxygen increased and the rate of decarburization slowed down. In this stage between 3 to 47% of oxygen was consumed for decarburization. Furthermore, in stage 1 where carbon has the most effect on the demanganization rate it has the least effect on carbon efficiency

whereas in stage 3 where it has the least effect on the demanganization rate it seems to have a considerable effect on controlling decarburization efficiency.

Table 3.2 Efficiency of oxygen for decarburization (%).

Alloy (wt%)	Stage 1	Stage 2	Stage 3
Fe-5Mn-0.42C	36	62	47
Fe-10Mn-0.42C	21	61	43
Fe-15Mn-0.42C	17	52	36
Fe-25Mn-0.42C	13	44	26
Fe-10Mn-0.18C	18	40	14
Fe-15Mn-0.18C	11	33	13
Fe-25Mn-0.18C	6	25	12
Fe-15Mn-0.05C	3	16	3
Fe-25Mn-0.05C	2	12	3

The calculated efficiencies of oxygen for manganese oxidation, $\eta_{O_2}^{deMn}$ for either stage 1 or 3 are greater than 100%. It indicates that oxidation of manganese by Equation 3.3 is not the only mechanism responsible for the total manganese loss. This observation is in agreement with the work of Lee *et al.* [11] and You *et al.* [14]. Both groups of researchers found that the available oxygen was not sufficient to account for the total manganese loss. You *et al.* [14] attributed the difference between the total manganese loss and loss to slag as the evaporative loss of manganese. In the following sections of this paper, the viability of the different mechanisms for the extra manganese loss is explored.

3.4.2 Rate of Mn Losses with Time

Figure 3.6 (a-h) show how manganese loss as MnO and the total loss change with the processing time for the different alloys. As explained earlier, this calculation is based on the assumption that all carbon is removed as CO after accounting for all oxygen associated with CO, the remaining oxygen is assumed to form MnO. Therefore, the rate of loss as MnO is calculated with knowing that $\eta_{O_2}^{deMn} = 100 - \eta_{O_2}^{deC}$. The excess manganese lost not associated with oxygen must be as metallic manganese. This increased in stage 1 with increasing manganese and decreasing carbon concentration in the alloy as seen in Figure 3.6 (b), Figure 3.6 (c), and Figure 3.6 (f). For alloys with 0.42% C, Figure 3.6 (d), and Figure 3.6 (g) wherein MnO formation is dominant in stage 1, the excess loss is small. These trends were observed in Lee *et al.* [11] work for the argon oxygen refining of high carbon ferromanganese.

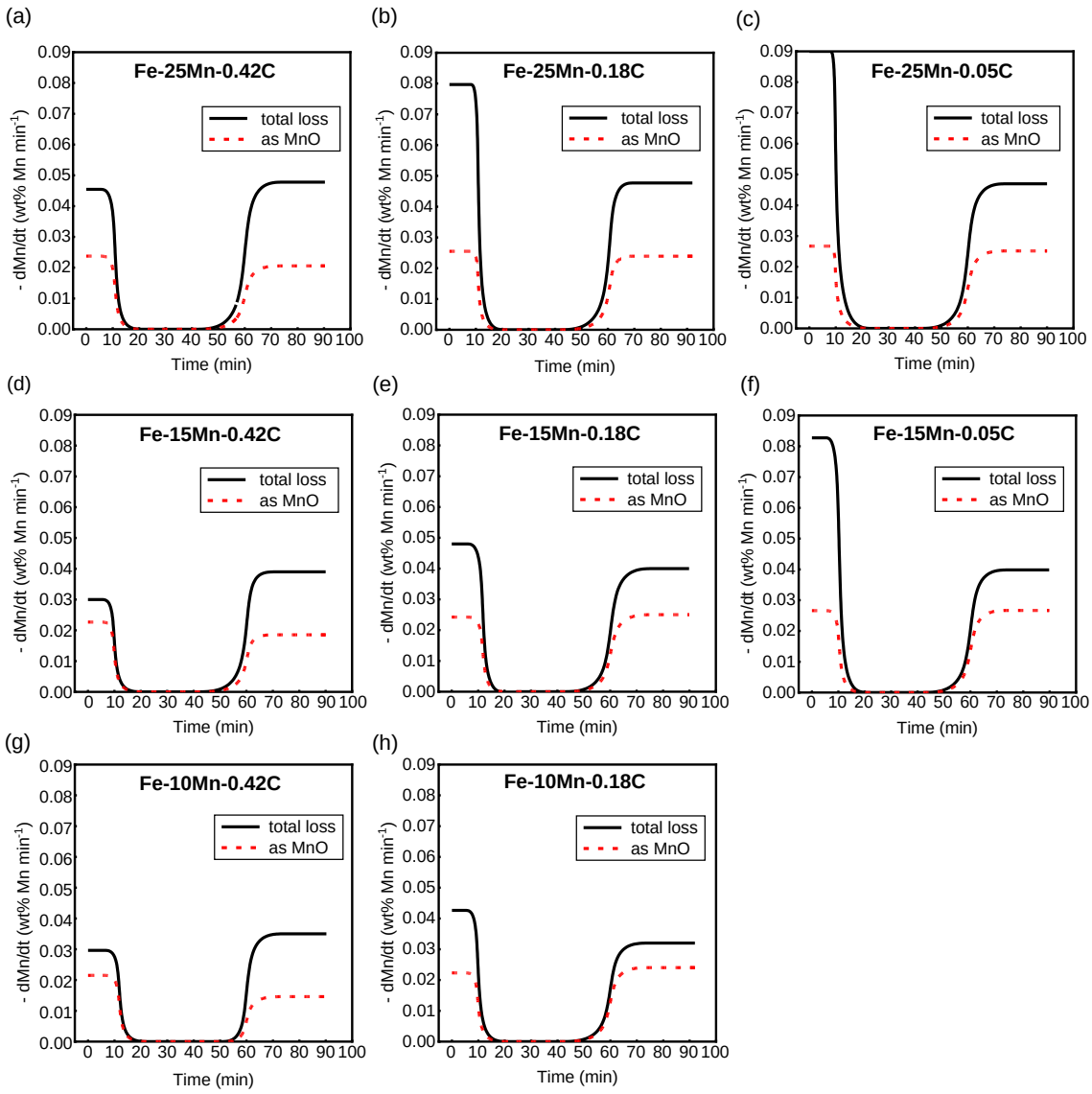

Figure 3.6 Rates of the total and as-MnO loss with time for a) Fe–25Mn–0.42C, b) Fe–25Mn–0.18C, c) Fe–25Mn–0.05C, d) Fe–15Mn–0.42C, e) Fe–15Mn–0.18C, f) Fe–15Mn–0.05C, g) Fe–10Mn–0.42C, and h) Fe–10Mn–0.18C.

3.4.3 Mn Loss by Evaporation

The most obvious source of excess manganese loss over that attributed to oxidation is as Mn(g). In this case, the difference between the total manganese loss and loss as-MnO is taken as evaporation loss according to Equation 3.4.

$$\left(\frac{d\%Mn}{dt}\right)_{total} = \left(\frac{d\%Mn}{dt}\right)_{evaporation} + \left(\frac{d\%Mn}{dt}\right)_{oxidation} \quad (3.4)$$

Knowing the rate of manganese removal and decarburization from the experimental data, the amount of carbon and manganese removed per bubble was calculated by Equation 3.5.

$$\frac{dn_i}{dt} = \frac{dn_i}{db} \times \frac{db}{dt} \quad (3.5)$$

where $\frac{db}{dt}$ is the frequency of the bubble formation which is calculated from the work of Irons *et al*. [20]. $\frac{dn_i}{db}$ is the number of moles of either Mn or C per bubble. Inside each bubble there exists CO, Mn (g), MnO (s) and Ar. The total pressure inside each bubble, P_t is 1 atm. Hence, the vapor pressure of manganese can be calculated from Equation 3.6.

$$p_{Mn} = \frac{n_{Mn}}{n_{CO} + n_{Mn(g)} + n_{Ar}} P_t \quad (3.6)$$

These calculated vapor pressure of manganese in each bubble for stages 1 and 3 are shown in Figure 3.7. It is noticeable that the vapor pressure of manganese in each bubble is much higher than that of pure manganese at 1823 K, i.e., 0.035 atm. Even if we consider an

increase in temperature due to exothermic reactions. Based on Equation 3.7 the required temperature for the bubble to get the vapor pressures presented in Figure 3.7 are in the range of 2100 to 2300 K. This mechanism does not appear to be feasible.

$$\ln\left(\frac{p_{Mn}}{a_{Mn}}\right) = \frac{-33440}{T} - 3.02\ln T + 37.67 \tag{3.7}$$

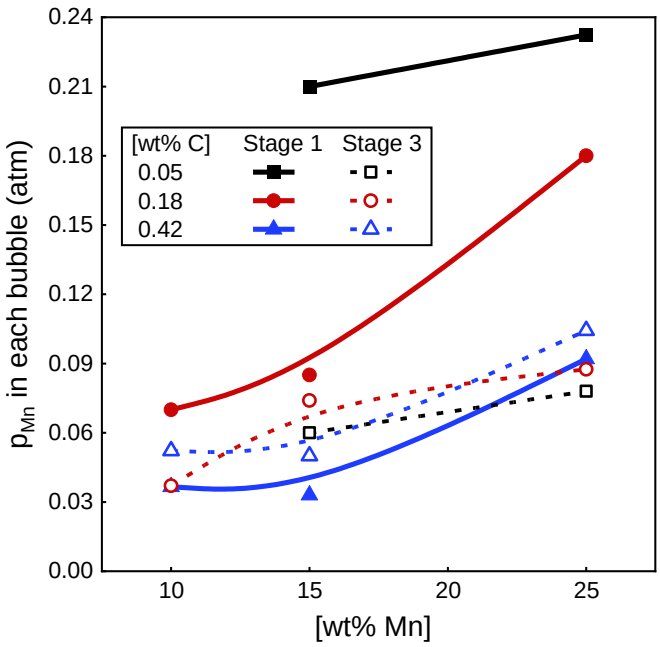

Figure 3.7 The vapor pressure of manganese in each bubble in stages 1 and 3.

3.4.4 The Mechanism for Additional Manganese Loss

As discussed above one requires a viable mechanism to describe the manganese loss as metal in excess of that removed as vapor. This requires removal of manganese in the condensed state most likely as a mist of fine liquid droplets inside the bubble. Therefore,

any proposed mechanism must consider how such droplets might form. The authors can only think of two possible mechanisms:

1) Preferential oxidation of manganese when the bubble forms at the nozzle tip, followed by reduction to Mn (l) by carbon. 2) Evaporation at the surface of the bubble followed by condensation inside the bubble. The former requires that the reduction must occur in the bubble interior or it will be dissolved back into the melt. Thus, the mechanism must involve gas phase ferrying via a CO/CO_2 oxidation-reduction couple. CO being formed via Equation 3.8 and MnO being reduced via Equation 3.9.

$$C + CO_2 = 2CO\ , \qquad \ln K_8 = \ln\left(\frac{p_{CO}^2}{a_C\, p_{CO_2}}\right) = 20.2 - \frac{19393}{T} \tag{3.8}$$

$$CO + MnO = CO_2 + Mn, \qquad \ln K_9 = \ln\left(\frac{a_{Mn}\, p_{CO_2}}{a_{MnO}\, p_{CO}}\right) = 0.42 - \frac{15267}{T} \tag{3.9}$$

For this mechanism to proceed CO/CO_2 set by Equation 3.8 must be greater than CO/CO_2 set by Equation 3.9. For the latter mechanism to be viable, the temperature at the bubble surface must be sufficiently high, from exothermic reactions, to for vapor pressure in equilibrium with the bubble surface (p_{Mn}^s) be higher than that in the liquid mist p_{Mn}^{mist}. In the next section, the viability of each mechanism will be explored.

3.4.4.1 Oxidation-Reduction Mechanism

As discussed above the formation of a fine mist of manganese inside the bubble via an oxidation-reduction mechanism requires the CO/CO_2 ratio in equilibrium with the melt to be higher than that in equilibrium with Mn (l)/MnO. At 1823 K the latter ratio would be

over 2800 whereas the highest value the CO/CO_2 ratio could have in equilibrium with the melt would be 1400. Therefore, this mechanism could not be viable.

3.4.4.2 Evaporation/Condensation Mechanism

If one assumes the temperature at the bubble surface is elevated because of the exothermic reactions forming CO and MnO but remains at 1823 K inside the bubble, there is a possible mechanism where manganese vapor is generated in equilibrium with the activity of manganese in the alloy and subsequently condenses at the lower temperature inside the bubble. The requirement for this mechanism to operate would be that the difference in temperature would be sufficient for

the Mn vapor pressure in equilibrium with the bubble surface (p^{S}_{Mn}) to be higher than that in equilibrium with pure Mn (l) at 1823 K (p^{mist}_{Mn}). Mn will continue to condense as long as the surface of the bubble remains at a sufficiently high temperature. This mechanism is equivalent to the metal fuming mechanism proposed by Turkdogan *et al.* [12] that the rate of evaporation of metal increased as the partial pressure of oxygen in the Ar-O_2 blowing mixture rose until it reached to its theoretical rate of evaporation in a vacuum. Any further increase in the partial pressure of oxygen caused the formation of oxide (fume) on the metal surface which dramatically impeded evaporation. Their mechanism involved the counter diffusion of metal vapor and oxygen across the boundary layer between the metal surface and the gas. The difference between the proposed mechanism here with fuming is that condensed Mn mist is formed rather than MnO fume. Equation 3.10 can be used, to determine the flux of Mn in the gas phase.

$$\frac{\frac{D_{Mn-Ar}}{\delta}}{R}\left(\frac{p_{Mn}^{mist}}{T_b}-\frac{p_{Mn}^{s}}{T_s}\right)=-\frac{dMn_{evap}}{A.dt} \quad (3.10)$$

D_{Mn-Ar} is the manganese vapor and argon interdiffusivity ($cm^2\ s^{-1}$)

δ is the thickness of the gas phase diffusion layer (cm)

R is the gas constant ($cm^3\ atm\ K^{-1}\ mol^{-1}$)

T_b and T_s are the temperatures of the bulk gas and at the bubble surface (K)

$\frac{dMn_{evap}}{dt}$ is the rate of evaporation of manganese ($mol\ s^{-1}$)

A is the surface area of the bubble (cm^2)

As mentioned earlier p_{Mn}^{s} must be higher than p_{Mn}^{mist}. Knowing that the activity of liquid manganese is unity inside the bubble, the minimum temperature at the surface of the bubble, T_s can be calculated from Equations 3.11 and 3.12. The vapor pressure and temperature of manganese at the bubble surface are tabulated in Table 3.3. As seen, T_s is independent of carbon level and it is higher for alloys with lower manganese concentration. For a constant carbon concentration, alloys with 10% and 25%Mn have the maximum and minimum vapor pressure of manganese at the surface of the bubble, respectively.

$$p_{Mn}^{mist}=a_{Mn}^{mist}p_{Mn\ at\ T_b}^{0}=\exp\left(\frac{-33440}{T_b}-3.02\ln T_b+37.67\right) \quad (3.11)$$

$$p_{Mn}^{s}=a_{Mn}^{s}p_{Mn\ at\ T_s}^{0}=a_{Mn}^{s}\exp\left(\frac{-33440}{T_s}-3.02\ln T_s+37.67\right) \quad (3.12)$$

The actual rate of manganese evaporation is unknown. Knowing that reaction is over during the residence time of the bubble (0.1 seconds), the minimum flux can be calculated from

the residence of the bubble. For instance, for Fe-25Mn-0.18C, the minimum rate of evaporation of manganese is equal to 6.2×10^{-7} mol s^{-1}. From Equation 3.12, T_S is 2023 K. $D_{Mn\text{-}Ar}$ is 4.09 cm^2 s^{-1}[21], assuming $\frac{D_{Mn-Ar}}{\delta}$ is 192 cm s^{-1}, δ would be 0.02 cm which is unrealistically high. From the other side, the maximum rate of evaporation of manganese in the vacuum (J_{max}) at 1823 K can be calculated from Equation 3.13 [12] where M_{Mn} is the molar mass of manganese. In this case, the thickness of the gas phase diffusion layer is 0.1 μm which seems to be too small. But it means that there is a practical range for δ in the middle that is very reasonable.

$$J_{max} = \frac{p_{Mn}}{\sqrt{2\pi RTM_{Mn}}} \tag{3.13}$$

Table 3.3 Calculation of available Mn from heated layer.

Alloy (wt%)	T_s(K)	p^s_{Mn}(atm)	Thickness of the heated layer (μm)	Amount of Mn in the heated layer (mol)	Total amount of Mn lost in one bubble (mol)
Fe-10Mn-0.42C	2185	0.042	0.27	2.3×10^{-6}	1.6×10^{-6}
Fe-15Mn-0.42C	2110	0.041	0.36	4.6×10^{-6}	1.7×10^{-6}
Fe-25Mn-0.42C	2023	0.039	0.55	11.8×10^{-6}	2.5×10^{-6}
Fe-10Mn-0.18C	2185	0.043	0.34	2.9×10^{-6}	2.4×10^{-6}
Fe-15Mn-0.18C	2110	0.041	0.43	5.6×10^{-6}	2.6×10^{-6}
Fe-25Mn-0.18C	2023	0.039	0.73	15.6×10^{-6}	4.0×10^{-6}
Fe-15Mn-0.05C	2110	0.042	0.43	5.5×10^{-6}	4.6×10^{-6}
Fe- 25Mn-0.05C	2022	0.040	0.64	13.8×10^{-6}	5.0×10^{-6}

3.4.5 Exothermic Reactions: Source of Temperature Rise at the Bubble Surface

Assuming that there is no heat loss by conduction and all the heat goes to the metal surrounding the bubble and all the oxygen is consumed to produce CO and MnO, the amount of the heat generated from the exothermic reactions of CO and MnO formation at 1823 K must be sufficient for the rising the temperature of the CO, MnO, and Mn(g) from 1823 K to the required higher temperatures (T_S). For instance, for Fe-25Mn-0.18C in stage 1, -0.57 J heat is generated. Knowing that for the liquid steel C_p is 46 J K^{-1} mol^{-1}, and T_S is 2023K, number of moles of steel that can be heated to T_S are 62×10^{-6} which is equal to 5×10^{-4} cm^3 metal. Knowing that the surface area of the bubble is 6.9 cm^2, the thickness of the metal layer beyond the surface of the bubble that can be heated up is 7.3×10^{-5}cm or 0.73 μm. From the experimental results, the total number of moles of manganese removed by one bubble, in this case, is 4×10^{-6}. It can be concluded that the layer around the bubble is thick enough to supply more than the required manganese in the bubble. From the other side, the heat absorbed for the rising temperature of the products from 1823 K to 2023 K is 0.02 J, which is very small compared to the exothermic heat released from the CO and MnO. As a result, the heat balance shows that this mechanism is feasible.

Table 3.3 presents the thickness of the heated layer, the number of moles of manganese in it and compares it with the total number of moles of manganese in each bubble for all the alloys in stage 1. In all cases, there is more manganese in the heated layer than inside the bubble. Similarly, this mechanism works for stage 3.

It is noteworthy that the rate of overall manganese loss is somewhat controlled by competition with carbon in stage 1. As seen in Figure 3.3, rate of manganese loss depends on the initial carbon concentration. In stage 3 it appears that there is still some competition with carbon but that only affects the amount of manganese that reacts with oxygen rather than the whole amount lost. That further suggests transport of manganese in the liquid as the rate determining step for manganese loss. On the other side, as more manganese oxidizes, more heat will be generated, and the surface of the bubble will be at the higher temperature leading to more evaporation (Figure 3.6).

3.4.6 Final slag composition

The slag formed during experiments was not monitored with time. The amount of slag at the end of the experiment for most of the alloys was too small to be analyzed. However, for three alloys the concentration of Mn and Fe in the slag was analyzed by ICP. By assuming that these elements were present as MnO and FeO, their corresponding concentrations were calculated and are provided in Table 3.4. However, slag compositions at the end of experiments do not necessarily help elucidate the mechanism in stage 2. However, based on the mass balance in stage 1, we can estimate the slag at the start of the stage 2 to be almost entirely MnO with an approximate mass of 1.2 grams.

Table 3.4 Chemical composition of final slag.

Alloy (wt%)	wt% MnO	wt% FeO
Fe-15Mn-0.05C	100	---
Fe-25Mn-0.05C	89	11
Fe-25Mn-0.18C	71	29

In stage 2, a plateau exists in the demanganization curve, given that the injected gas bubbles are identical to those in stage 1 and the melt has changed very little it seems unlikely that the plateau was caused by a cessation in manganese oxidation. However, if we assume the Mn loss at the bubble is identical to that in stage 1 there would be insufficient Mn in the slag to balance that loss. This realization leads the authors to conclude that the change in mechanism has suppressed Mn oxidation and small reversion is due to reduction of Mn from slag. The authors are not currently able to offer a definitive explanation for this, however it is worth noting under the conditions of these experiments, C oxidation is thermodynamically favored over Mn oxidation. Therefore, it is quite feasible that a subtle change in the relative kinetics could results in inhibition of Mn loss. Any temperature rise in the melt from oxidation reactions would favor this change. For a limited number of experiments, the authors used a thermocouple in contact with the bottom of the crucible but were not able to detect any temperature rise. Therefore, any temperature rise must have been local or not very large.

3.4.7 Comparison of Mn and Cr in Argon-Oxygen Refining Process

In this part, the behavior of Cr and Mn during argon-oxygen refining are discussed from various aspects such as mechanisms of losses, the effect of temperature and bubbling or blowing into the melt. Researchers in the past [22-29] have classified the decarburization of Fe-C-Cr alloys into two stages based on a critical carbon concentration C_{crit} above which rate of decarburization is independent of initial carbon concentration and below which rate

decreases with carbon concentration. The thermodynamics of Equation 3.14 predicts the critical carbon concentration where chromium starts to oxidize in preference to carbon [30].

$$Cr_2O_3 + 3C = 2Cr + 3CO \quad (3.14)$$

In Yamamoto *et al.* [9] work, the transition point between the middle and final stage is referred to the C_{crit} and they observed that it decreased from 1.4% to 0.6%C when they changed the blowing condition from only top to the combined blowing. Consequently, the major manganese loss in stage 3 hindered. As shown by Lee *et al.* [11] the second and third stages of decarburization were controlled by the supply of oxygen and liquid phase mass transfer, respectively. Therefore, the nature of C_{crit} in their work is similar to that of Cr alloys. However, in this study with lower carbon concentrations unlike the high carbon ferromanganese alloys, manganese loss started from the beginning.

The only mechanism of Cr loss is oxidation from the surface of the metal. However, in addition to oxidation, Mn can evaporate beyond the surface of the metal and form MnO fume [11,31] or as shown in the present work evaporate and condense inside the bubble as liquid mist.

The rate of decarburization for both Cr and Mn alloys is highly temperature dependent [14,32]. High vapor pressure of Mn leads to more loss by evaporation at elevated temperatures [8,9,33]. In contrast, in Cr containing alloys, low temperature favors the oxidation of Cr [34]. As seen in the present study, for a given C concentration in stage 1, the rate of decarburization depends on the initial Mn concentration of alloy. This is because in stage

1 there is a competition between Mn and C for oxygen. However, in Barnhardt's work [22] for air bubbling to the Cr containing melts there was no Cr oxidation initially and the rate of decarburization was the same for Fe-(0, 10, 15, 21%) Cr-0.3%C alloys.

Rate of decarburization of both high carbon ferromanganese alloys and stainless steel was improved in order of top O_2 blowing, top O_2 with bottom Ar stirring to the combined top and bottom O_2 blowing with bottom Ar stirring. Less Mn and Cr loss occurred with that order of configuration of blowing [9,35]. Watanabe *et al.* [32] and Fulton *et al.* [36] also observed from experimental work that the efficiency of oxygen for decarburization was higher in bubbling compared to the blowing to the surface of stainless steel under pressure and at atmospheric pressure, respectively.

For a certain gas flow rate, nozzle geometry, and temperature, increasing the depth of submergence protects Cr from oxidation. Because after the formation of Cr_3O_4 [24] or Cr_2O_3 [23] deep in the melt it will be reduced by C to Cr. However, in shallow melts Cr will oxidize right from the beginning and there is not enough time to be reduced back into the melt [37]. In the case of Mn alloys, Mn loss will be very high if oxygen is blown onto the surface of the melt since a hot spot will form and intensify Mn evaporation. Different authors [35,38,39] have reported a temperature rise at the hot spot between 1900℃ to 2450℃. This has been shown to have significant impact on Mn loss during refining [9]. Oxygen injection through submerged tuyeres would diminish the evaporative loss of Mn because there is vigorous agitation of the melt and locally generated heat would be dissipated through transfer to the melt, lowering the temperature increase. This is the basis of the established practice, in

AOD refining of ferromanganese and ferrochromium alloys, of combining top and bottom blowing of Ar-O_2 to avoid excessive loss of Mn and Cr [40].

Decreasing the O_2/Ar ratio the gas mixture not only can promote the rate of decarburization in both Cr [23–25] and Mn alloys [19,40], it is beneficial for Cr and Mn retention in the bath, as well.

The addition of CO_2 to O_2 or replacement of O_2 with CO_2 in the Ar-O_2 gas mixture increases the rate of decarburization of Fe-16% Mn-3% C [15] and Fe-(10-15%) Cr-3% C alloys [41] and improves the yield of Mn and Cr in the bath.

3.5 Conclusions

To study the kinetics and mechanism of decarburization and demanganization of high-manganese steel in Ar–O_2 processing, experiments were carried out with Fe–Mn–C alloys with 5–25% Mn and 0.05–0.42%C at 1823 K. Findings from this study are summarized here. 1) Decarburization and demanganization required more than the available oxygen. Therefore, all the manganese is not lost by only the oxidation mechanism. 2) Assuming carbon must react with oxygen and form CO, the Mn metal loss is greater than the vapor pressure supports. Therefore, the extra Mn loss is not taking place only by evaporation. 3) The oxidation/reduction mechanism is not supported by the calculations. 4) Local temperature increase facilitating evaporation condensation as a mechanism is feasible but requires a significant temperature rise. The parameters for this mechanism were explored,

and it was supported both thermodynamically and kinetically. 5) The rate of overall manganese loss is at least partly controlled by transport of manganese in the liquid phase.

3.6 Acknowledgments

The authors would like to acknowledge financial support from the Natural Sciences and Engineering Research Council of Canada (NSERC). They also thank ArcelorMittal Dofasco, Stelco, Praxair, and Hatch Ltd. for their support.

3.7 Conflict of Interest

The authors declare no conflict of interest.

3.8 References

[1] B. C. De Cooman, K. Chin, J. Kim, in *New Trends and Developments in Automotive System Engineering* (Ed: M. Chiaberge), InTech **2011**, p 101.

[2] O. Bouaziz, S. Allain, C.P. Scott, P. Cugy, D. Barbier, *Curr. Opin. Solid State Mater. Sci.* **2011**, 15, 141.

[3] B.J. Jamieson, K.S. Coley, *Metall. Mater. Trans. B* **2017**, 48, 1613.

[4] R. Elliott, K. Coley, S. Mostaghel, M. Barati, *JOM* **2018**, 70, 691.

[5] D.S. Kozak, L.R. Matricardi, *Iron Steelmak.* **1981**, 8, 28.

[6] M.M. Gasik, *Handbook of Ferroalloys. Theory and Technology*, Butterworth Heinemann, **2013**.

[7] W. Dresler, in *Steelmaking Conference Proceedings*, **1989**, 13.

[8] Z. Georgeou, C.F. Redeker, J. Schottler, R.-H. Gronebaum, A. Redenius, K. J, A. Newirkowez, D. Rohrberg, J. Wendelstorf, K.-H. Spitzer, R. Nystrom, *Cost-Efficient Metallurgy for the Production of Novel Ultra High- Strength Deep-Drawable Steel Grades with High Mn Contents from 10 to 25 Wt . % by Using the EAF Steelmaking Route*, European Union **2010**.

[9] K. Yamamoto, T. Mimura, S. Ito, T. Onoye,*Tetsu-to-Hagane* **1986**, 72, 1034.

[10] V.-V. Visuri , Doctoral Thesis, University of Oulu, Faculty of Technology, **2017**.

[11] Y.E. Lee, L. Kolbeinsen, *ISIJ Int.* **2005**, 45, 1282.

[12] E.T. Turkdogan, P. Grieveson, L.S. Darken, *J. Am. Chem. Soc.* **1963**, 67, 1647.

[13] B.-D. You, *J. Korean Institue Met. Mater.* **1995**, 33, 1508.

[14] B.-D. You, B.-W. Lee, J.-J. Pak, *Met. Mater.* **1999**, 5, 497.

[15] H. Liu, J. Liu, J. Schenk, F.M. Penz, L. Sun, R. Zhang, Z. An, *Metall. Mater. Trans. B* **2020**, 51, 756 . 2020, 51, 756.

[16] J. Wei, D. Zhu, *Metall. Mater. Trans. B* **2002**, 33B, 121.

[17] Y. Niiri, K. Ito, K. Sano, *Tetsu-to-Hagane* **1969**, 55, 437.

[18] H. Sun, R.D. Pehlke, *Metall. Mater. Trans. B* **1995**, 26, 335.

[19] B. You, J. Han, J. Pak, *Steel Res.* **2000**, 71, 22.

[20] G.A. Irons, R.I.L. Guthrie, *Metall. Trans. B* **1978**, 9, 101.

[21] P. Grieveson, E.T. Turkdogan, *J. Phys. Chem.* **1964**, 68, 1547.

[22] Lyall Franklin Barnhardt, Doctoral Thesis, Massachusette Institute of Technology, **1965**.

[23] R.J. Fruehan, *Ironmak. Steelmak.* **1976**, 3, 153.

[24] Y. Kobayashi, S. Maruhashi, *ISIJ* **1977**, 13, 158.

[25] T. Ohno, T. Nishida, *Tetsu-to-Hagane* **1977**, 63, 2094.

[26] S. ya Kitamura, K. Okohira, A. Tanaka, *ISIJ* **1985**, 72, 47.

[27] O.K. Tokovoi, A. V Tokarev, A.N. Volkadaev, S.N. Prokofev, A.N. Komarov, *Izvvestiya Ross. Akad. Nauk. Met.* **1995**, 3, 10.

[28] S. Dey, D.N. Ghosh, *Metall. Mater. Trans. B* **1976**, 7, 43.

[29] T. Kuwano, S. Maruhashi, Y. Aoyama, *Tetsu-to-Hagane* **1973**, 59, 863.

[30] S. Seetharaman, A. Mclean, R.I.L. Guthrie, S. Seetharaman, *Treatise on Process Metallurgy, Vol.2: Process Phenomena*, Elsevier, Amsterdam **2014**, p. 230.

[31] Y. Ma, I. Kero, G. Tranell, *Oxid. Met.* **2018,** 211.

[32] T. Watanabe, T. Tohge, *Trans Iron Steel Inst Jap* **1974**, 14, 425.

[33] Y. Kato, T. Suzuki, Y. Kishimoto, *Tetsu-to-Hagane* **2011**, 97, 252.

[34] D. R. Swinbourne, T.S. Kho, B. Blanpain, S. Arnout, D.E. Langberg, *Miner. Process. Extr. Metall.* **2012**, 121, 23.

[35] R. Tsujino, K. Kato, S. Kitamura, H. Morishige, R. Nakao, R. Hisatomi, H. Takano, H. Hirata, *Advances in Stainless Steelmaking Technology*, **1994**.

[36] J.C. Fulton, S. Ramachandran, in *Proceedings of Electric Furnace Pro. AIME*, **1972**, 43.

[37] R.J. Fruehan, *Met. Trans. B* **1975**, 6, 573.

[38] C. Delhaes, A. Hauck, D. Neuschutz, *Steel Res.* **1993**, 64, 22.

[39] R. Nakao, H. Takano, H. Morishigie, S. Tanaka, *Tetsu-to-Hagane* **1996**, 82, 267.

[40] B.-D. You, K.-Y. Park, J.-J. Pak, J.-W. Han, *Met. Mater.* **1999**, 5, 395.

[41] H. Wang, N.N. Viswanathan, N.B. Ballal, S. Seetharaman, *High Temp. Mater. Process.* **2009**, 28, 407.

Chapter 4

4 Kinetics of Decarburization and Manganese Loss from Fe-15Mn-1C Alloys by Bubbling of Argon-Oxygen Gas Mixtures

In Chapter 4, all of the experiments and data analysis were carried out by me. Dr. Kenneth S. Coley offered lots of insightful discussions to enrich data analysis. The manuscript was initially drafted by me, edited, and revised by Dr. Kenneth S. Coley, and reviewed to the final version by Dr. Gordon A. Irons. The manuscript of this work has been submitted to Metallurgical and Materials Transactions B.

Abstract

In this work, the kinetics of decarburization and demanganization of Fe-15Mn-1C alloys by bubbling mixtures of Ar-O2 into the melt at 1823K was studied. Experiments were conducted at total gas flow rates of 200 and 300 Nml/min and gas mixtures of Ar containing 6.7 to 20 $\%O_2$. Increasing the gas flow rate and oxygen in the gas mixture resulted in higher overall rates of decarburization and demanganization. However, the experiments with the lowest O2 concentration were the most efficient in terms of oxygen utilization for decarburization. The ratio of manganese loss to decarburization was found to be controlled by the relative mass transport of Mn and C in the metal. Based on the estimated mass transfer coefficient for either C or Mn, the reaction time for each bubble was estimated to be 0.001 seconds which is about 1% of the residence time of the bubble in the liquid. Although the initial competition for oxygen between manganese and carbon was controlled

by relative mass transport rates, this work found no evidence that manganese and carbon repartitioned towards the equilibrium over the remaining lifetime of the bubble.

4.1 Introduction

Advanced high-strength steels (AHSS) rely heavily on the manganese content as an important alloying element. High manganese twinning-induced plasticity (TWIP) steels with 15-30%Mn [1,2] attracted the automotive industry's interest due to their outstanding combination of strength and elongation. Since the 1980s, the properties of this grade of steels have been researched extensively; a review of these studies is summarized by Bouaziz *et al.* [3]. However, less attention was paid to the processing of these steels. Currently to the knowledge of the authors only POSCO [4,5] and Thyssen Krupp [6] have commercialized the production of high manganese steels containing up to 26% Mn and 0.2-0.6% C. The important challenge for steelmakers is to reduce carbon content while minimizing the manganese losses during the oxygen refining process because high temperature and the presence of oxygen can lead to excessive manganese losses [7,8]. The yield of Mn in the Argon Oxygen Decarburization (AOD) processing of high carbon ferromanganese is reported to be 92% and higher [9]. Hence, AOD can be an appropriate route to produce high manganese steels. AOD is broadly researched experimentally and mathematically for the behavior of chromium in stainless steels [10–20]. For stainless steel, there is a critical carbon content C_{crit} above which no chromium is oxidized and the rate of decarburization is controlled by the supply of oxygen. Below C_{crit}, chromium oxidizes, and mass transfer of carbon in the liquid controls the decarburization rate [21]. For AOD

processing of stainless steel, Krivsky [27] proposed that argon must be injected deep in the melt to be dispersed thoroughly to be efficient in gas dilution. This finding was later confirmed by Saccomano *et al*. [23] for plant data and by Fruehan [24] in laboratory experiments. In Fruehan's study [24], a mixture of Ar-O_2 was injected into a shallow bath of 7.5 cm of stainless steel containing18Cr-8Ni-0.5C. He reported that the ratio of the rates of Cr to C removal was nearly identical to their concentrations in the liquid despite the fact that thermodynamics heavily favored CO formation. Fruehan interpreted these results to suggest that chromium oxidized more rapidly than carbon because of faster mass transport. Due to the short residence time of the bubble in the bath, there was insufficient time for reduction of chromium oxide (Cr_2O_3) by C to bring the Cr_2O_3/CO back towards the equilibrium. These findings were the basis of a model for Cr recovery in AOD [11] wherein it was assumed that in the vicinity of the tuyeres, Cr is mainly oxidized and as the bubbles ascend Cr_2O_3 at the surface of the bubbles is reduced by dissolved C. The current work aims to determine whether during AOD refining, the competition for oxygen between manganese and carbon follows the same mechanism as that of chromium and carbon.

Compared to stainless steel, there are only a few published studies on the oxygen refining of high manganese alloys [25–30]. Yamamto *et al.* [25] studied the simultaneous decarburization and manganese loss in Ar-O_2 refining of Fe-76Mn-6.8C-(0.01-0.08)Si melts in a pilot converter with top lance O_2 blowing and bottom plug Ar or Ar+O_2 injection. Carbon and manganese concentrations changed in three stages with respect to time. First, there was manganese loss, followed by a reversion stage and then a final rapid manganese

loss. Initially, the rate of carbon removal was slow, proceeding to a higher rate and finally slowing to an almost negligible rate. Manganese loss was reported to be due to oxidation and evaporation however, the kinetics of decarburization and Mn losses were not addressed. Lee *et al*. [26] analyzed Yamamoto's data and proposed that the rate-controlling steps for decarburization were chemical reaction at the gas/liquid interface in stage 1, mass transfer of oxygen in the gas phase during stage 2, and the mass transfer of carbon in the liquid phase in stage 3. These researchers reported the excess oxygen enhanced Mn evaporation to form MnO fume according to the mechanism of Turkdogan *et al*. [31]. However, no mention was made of metal phase mass transfer control in reference to Mn which makes sense at very high Mn concentrations.

You [27] studied decarburization of Fe-75Mn-7C-0.3Si by combined top and bottom Ar/O_2 blowing in an 87 kg AOD converter. Decarburization proceeded quickly initially until reaching approximately 2% at which point demanganization started and decarburization ceased. Later, You *et al.* [28,29] studied the decarburization of Fe-75Mn-6C using $Ar-O_2$ injection in a laboratory setup reporting that the utilization of oxygen for decarburization increased remarkably with increasing temperature and decreasing fraction of oxygen in the gas mixture. This is in accordance with thermodynamic predictions that at higher temperatures, CO formation is favored over MnO. In a further study, these workers [30] conducted oxygen refining of high carbon ferromanganese in a 2-ton AOD converter with combined blowing. The reported total manganese loss by oxidation and evaporation was

between 2 and 25%. In contradiction to the previous work of this group [28,29], they recommended lower temperatures to avoid evaporative loss of Mn.

Liu *et al*. [32] examined CO_2-O_2 injection into a Fe-16Mn-3C alloy showing that the dilution of O_2 with CO_2 enhances the rate of decarburization while retaining Mn in the bath. These workers did not offer a detailed analysis, proposing that Mn loss was due to evaporation and oxidation.

Despite several studies of argon-oxygen refining of high carbon ferromanganese, no full picture of the behavior of Mn in AOD is presented in the published literature. It might be expected that Mn and Cr behave similarly in AOD refining but researchers have highlighted the role of MnO fume formation which might lead to some differences. As proposed by Fruehan for AOD refining of stainless steel the Cr_2O_3 layer formed at the bubble melt interface is reduced by carbon during the bubble rise through the melt. In the case of manganese, if the oxide is formed as a fume inside the bubble it may not be as accessible for reduction by carbon. Furthermore, there is little discussion in the Mn literature regarding the concept of a critical carbon concentration.

Previous work by the authors [33] focused on the kinetics of manganese loss and decarburization in Ar-O_2 bubbling into Fe-Mn-C alloys containing 0.05 to 0.42% C and 5 to 25% Mn at 1823K. The rate of total manganese loss and the competition between carbon and manganese for oxygen appeared to be at least partly controlled by the relative rates of manganese and carbon transport in the liquid metal. This observation agrees with the findings of Fruehan for Cr-C alloys. The current work will explore further, the nature of

the competition between manganese and carbon for oxygen. Furthermore, the authors' previous work [33] for alloys with between 0.05 and 0.42% C, showed that the total manganese loss could only be explained by invoking an evaporation-condensation mechanism. The current work will determine if this mechanism operates when the carbon concentration is increased to 1%.

In summary, the current work will address gaps in the published literature regarding the behavior of Mn in AOD refining. Specifically, this work will investigate the competition between Mn and C for O_2 including, the role of relative mass transport rates in the metal, the possibility of oxide fume formation via Mn vapor, and the existence or otherwise of critical carbon content. The authors will also examine whether their previously proposed mechanism for Mn evaporation-condensation continues to operate at higher carbon contents.

4.2 Experimental Method

The experimental method identical to the previous work used by authors [33], is summarized here for the convenience of the readers. The steel composed of 15%Mn and 1%C was prepared by mixing electrolytic iron powder (99.977%), manganese flakes (99.990%), and graphite (99.9999%). To remove the oxide layer from manganese flakes, a 5% HCl solution was used for acid pickling before the mixing. 330 g of the steel mixture was placed in an alumina crucible with the outer and inner diameter of 4 and 3.8 cm and a height of 9 cm and positioned in the hot zone of the furnace. A vertical resistance furnace with an alumina tube of an inner diameter of 7.9 cm and a height of 76.2 cm was used as shown in Figure

4.1. The furnace was sealed using O-rings and water-cooled stainless steel caps at both ends. The metal was melted under an argon atmosphere that before entering the furnace was passed through a column of anhydrous $CaSO_4$. To ensure that the furnace was fully sealed before each experiment it was evacuated using a vacuum pump and backfilled with argon. The crucible was then heated in the furnace to the target temperature of 1823K (1550℃) and held for one hour to homogenize the melt. The temperature was controlled within ±8 K using a B-type (Pt30Rh-Pt6Rh) thermocouple. At this temperature, the system was evacuated and backfilled with argon again. Then the entrance and exit gas were opened and, the nozzle was lowered into the melt where the height of the bath above the tip of the nozzle was 3 cm. Then, a mixture of $Ar\text{-}O_2$ was injected into the melt through a single bore alumina tube with the outer and inner diameters of 0.48 cm 0.16 cm, respectively. The total flow rates were 200 and 300 Nml/min and the gas mixture varied from 6.7 to 20 %. It should be noted that for each experiment, the gas flow rate and composition were constant. The metal samples were taken frequently and were analyzed by ICP-OES for manganese content and by LECO for carbon content.

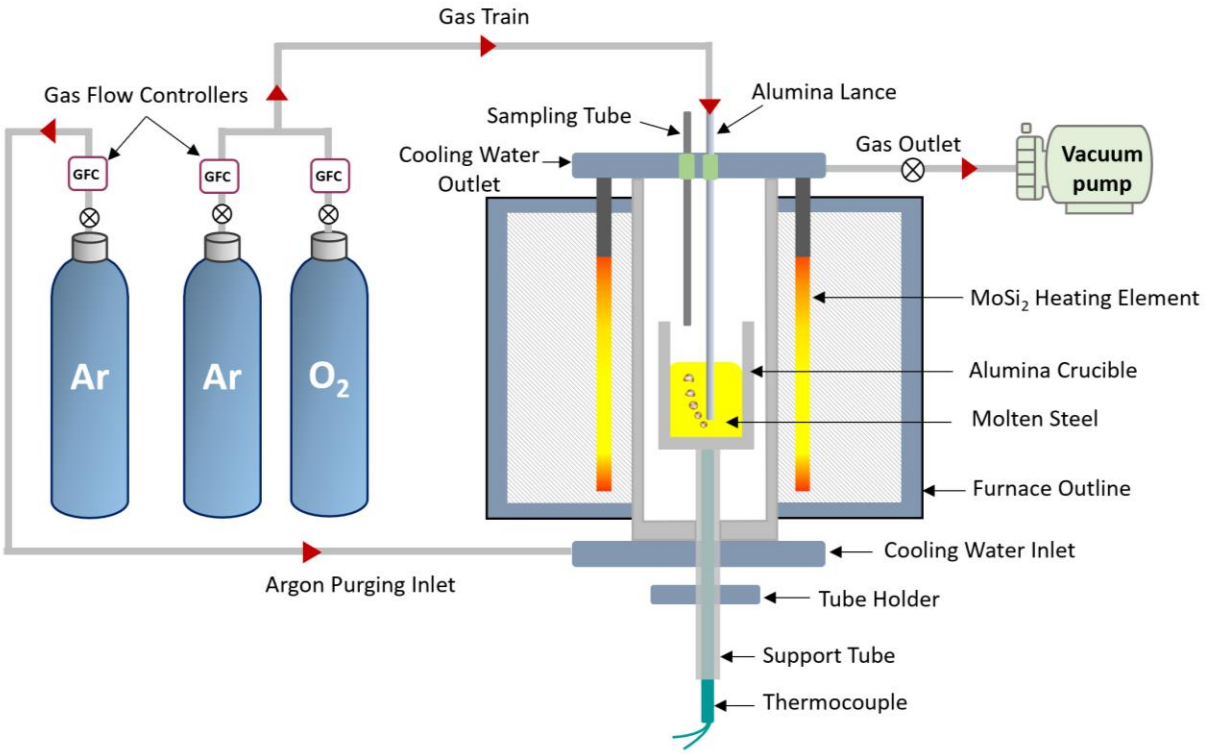

Figure 4.1 Schematic diagram of the experimental setup used in this work-not to scale.

4.3 Results

4.3.1 Effect of Gas Composition and Flow rate on Decarburization and Manganese Loss

To investigate the effect of gas composition on the rate of decarburization and demanganization, experiments were conducted at 1823K using Ar-O_2 mixtures containing 6.7 to 20 % O_2 at total flow rates of 200 and 300 Nml/min. The results are shown in Figure 4.2 and Figure 4.3. For both gas flow rates, the decarburization rate increased with increasing oxygen in the gas mixture. This is in agreement with studies by Fruehan [11] for AOD processing of Fe-1.2C-11Cr alloys but contrary to the finding of You *et al*. [28,29] for decarburization of Fe-75Mn-6C alloys.

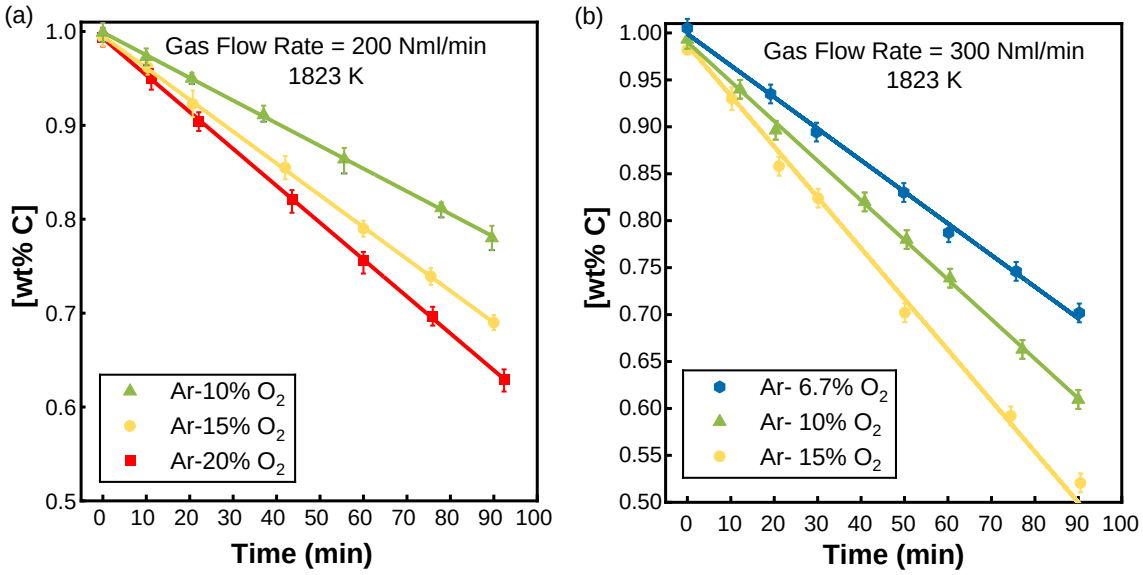

Figure 4.2. Variation of carbon concentration of Fe-15Mn-1C alloys with time at 1823K for the flow rates of a) 200 Nml/min b) 300 Nml/min, Variable gas composition.

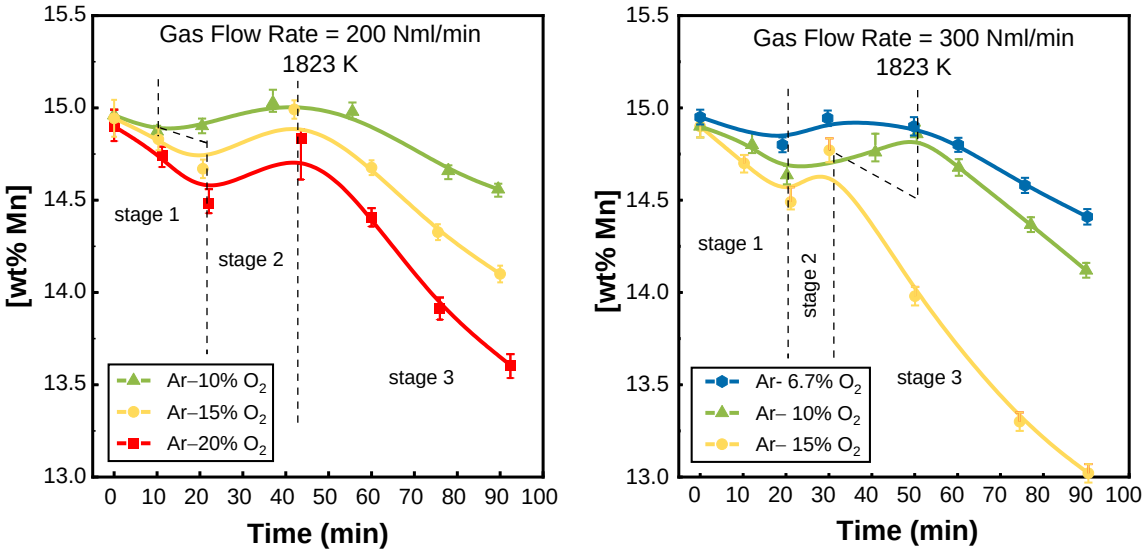

Figure 4.3. Variation of manganese concentration of Fe-15Mn-1C alloys with time for the flow rates of a) 200 Nml/min b) 300 Nml/min at 1823K, Variable gas composition.

Figure 4.3 shows data for the effect of gas composition on the rate of demanganization of Fe-15Mn-1C alloys. As found in previous work by the authors [33] demanganization proceeds in three stages. For lower flow rates and lower oxygen in the gas mixture, Mn loss in stage 1 is discernible but low, making it difficult to distinguish between stage 1 and stage 2. With increasing oxygen in the gas mixture, the rate of demanganization increased in stages 1 and 3. This finding is consistent with the reported data by You *et al*. [29] for Fe-75Mn-6C and Liu *et al*. [32] for Fe-16Mn-3C alloys.

From the comparison of the slopes of the rate plots in Figure 4.2 (a) and (b), it is seen that the rate of decarburization increases with the flow rate. The corresponding curves for manganese presented in Figure 4.3 show that the demanganization rate also increases with flow rate. Quantitative comparison of the rates (Table 4.1) shows that for the same gas composition the rate increases in direct proportion to the total flow rate. This is in agreement with the work of Liu *et al*. [32].

Table 4.1 Slopes of the rate of decarburization and demanganization plots

Ar-10 % O_2			
Flow rate (Nml/min)	-dC/dt	-(dMn/dt) $_{Stage\ 1}$	-(dMn/dt) $_{Stage\ 3}$
200	0.0027	0.0087	0.0124
300	0.0043	0.013	0.0187
Ar-15% O_2			
Flow rate (Nml/min)	-dC/dt	-(dMn/dt) $_{Stage\ 1}$	-(dMn/dt) $_{Stage\ 3}$
200	0.0034	0.0132	0.0186
300	0.0051	0.0194	0.029

4.4 Discussion

4.4.1 Thermodynamic Assessment

To compare the experimental data with thermodynamic predictions, the equilibrium composition of liquid metal and gaseous and oxide products was calculated using FactSage 8.0, with FactPS, FToxid, and FSstel databases in the Equilib module. For these calculations, the input amount and composition of the metal, gas flow rate, and gas composition, were chosen to be the same as used in the experiments presented above. It was assumed that the temperature remained constant at 1823 K during the processing time.

Figure 4.4 shows the calculated changes in the carbon and manganese concentration in the bath at different oxygen levels in the gas mixture for a flow rate of 200 Nml/min. The prediction is entirely consistent with the concept of critical carbon content showing a two-stage trend. Above the critical carbon content, no manganese is predicted to be oxidized, and all oxygen is consumed for decarburization. Below the critical carbon concentration, most of the oxygen is predicted to be consumed by the oxidation of manganese and decarburization is much slower.

A critical finding of the current work is that, although Figure 4.4 (a) and (b) are essentially thermodynamic predictions of the data presented in Figure 4.2 (a) and Figure 4.3 (a) respectively, there is no agreement between the prediction and the experimental observations. This is definitive proof that although the reaction between injected bubbles and the melt is expected to be very fast, the injected bubbles do not achieve equilibrium with the bulk melt.

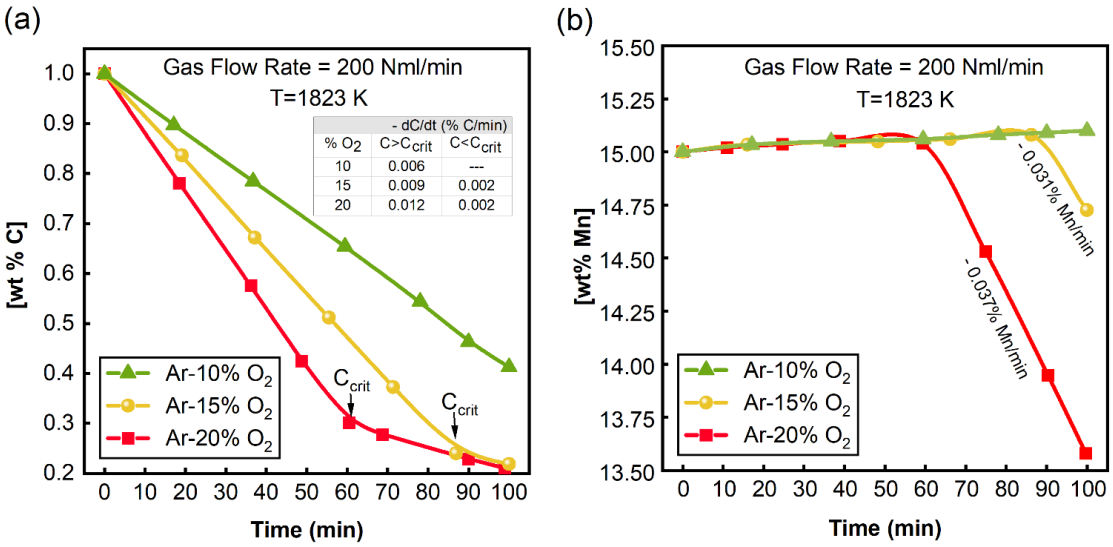

Figure 4.4 FactSage prediction for a) carbon concentration vs. time, and b) manganese concentration vs. time at a total gas flow rate of 200 Nml/min, variable: oxygen in the gas mixture.

4.4.2 Rate of Decarburization and Demanganization

Figure 4.5 shows that the rates of decarburization normalized for oxygen flow rate versus the oxygen percentage in the gas mixture are independent of the total gas flow rate. With increasing oxygen concentration in the gas mixture, the overall rate of decarburization is increased, however, the efficiency of oxygen for decarburization decreases. In the work of You *et al*. [28] for Fe-75Mn-6C alloys, the rate of decarburization decreased with increasing O_2 concentration in the Ar-O_2 mixture. These workers stated that by lowering the $O_2/(Ar+O_2)$ ratio, the equilibrium carbon concentration at the liquid/bubble interface is decreased. The difference in Mn and C concentration compared to the current work could be one reason for this apparent contradiction.

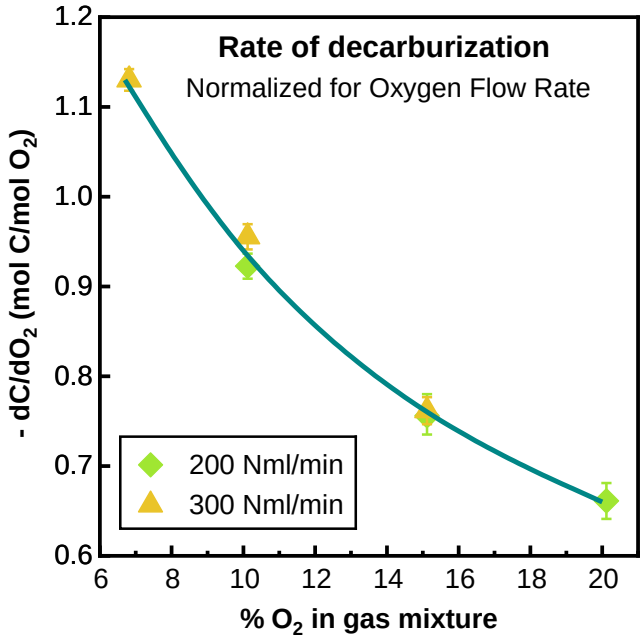

Figure 4.5. Rate of decarburization of Fe-15Mn-1C alloys versus percent oxygen in the gas mixture normalized for oxygen flow rate.

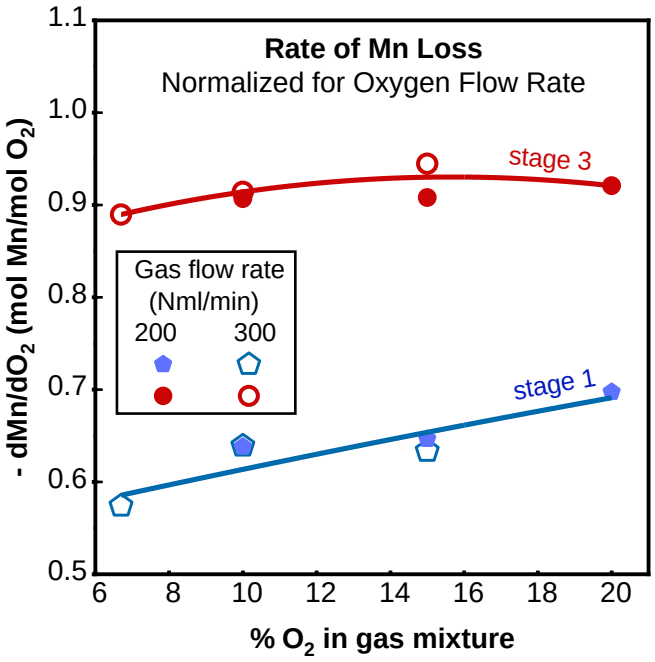

Figure 4.6. Rate of demanganization of Fe-15Mn-1C alloys versus percent oxygen in the gas mixture normalized for oxygen flow rate.

In Figure 4.6 the rate of manganese loss is normalized for oxygen flow rate by plotting (dMn/dO_2) versus $\%O_2$ in the gas mixture. In stage 1, dMn/dO_2 increased linearly with oxygen concentration in the gas mixture, but it is hardly affected in stage 3. It is interesting to note that while the oxygen that goes to carbon is nearly constant with time, in terms of oxygen that goes to manganese there is a significant difference between stages 1 and 3. It seems that carbon oxidizes at an almost constant rate and the competition for what is left is between Fe and Mn. In stage 2, it would appear that either, all the oxygen went to Fe or that Fe and Mn oxidized in proportion to their concentration in the alloy, giving the appearance of no manganese loss. With increasing gas flow rate, the increased oxygen supply resulted in the observed higher rate of manganese loss (Table 4.1). However, in both stages, the normalized rates of demanganization were independent of flow rate (Figure 4.6). For all oxygen levels, the rates of demanganization were lower in stage 1 than in stage 3. This observation is similar to previously reported data by the authors [33] for Fe-15Mn-0.42C alloy. However, for Fe-15Mn-0.05C and Fe-15Mn-0.18C the rates of demanganization were higher in stage 1. It has been shown that with decreasing carbon concentration in the alloy, the contribution of evaporative loss to overall demanganization increased. To facilitate discussion demanganization data from the authors' previous work [33] are shown in Figure 4.7 along with the equivalent data from the current study.

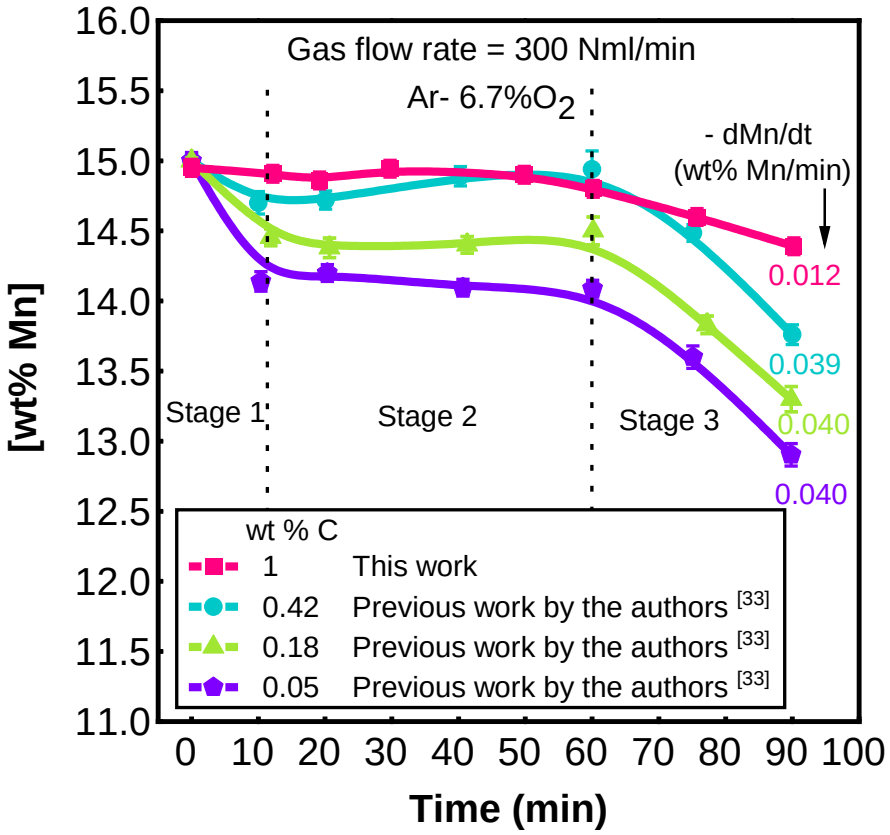

Figure 4.7 Manganese concentration in the bath versus time for Fe-15Mn alloys, gas flow rate: 300 Nml/min and gas composition Ar-6.7% O_2.

In stage 1 the data show that for a higher carbon concentration in the melt the rate of demanganization is decreased. In stage 3, for lower carbon (<0.42%) alloys, the rate of demanganization is the same regardless of carbon content. However, at 1% carbon, demanganization in stage 3 is much slower than that for the lower carbon alloys. These observations suggest that the role of carbon in competing for oxygen is more significant during stage 1, and nonexistent in stage 3 for lower carbon alloys, but for 1% C alloy is very significant. In order to understand the factors in play, it is worth analyzing how oxygen is partitioned between the species in the system.

4.4.3 Oxygen Partitioning

The objective of this section is to determine the way in which oxygen partitions amongst CO, CO_2, MnO, and FeO. It is reasonable to assume that the products of oxidation are primarily CO and MnO, so the efficiencies of oxygen for decarburization and manganese removal are the fraction of oxygen consumed for CO and MnO formation to the total supplied oxygen. While this assumption is consistent with previous findings of the authors [33], examination of Table 4.2 shows that based on this assumption, a considerable amount of oxygen would remain unconsumed for the case of Fe-15Mn-1C alloy. This is especially true in stage 1 of the process. In Fruehan's work [24] on Fe-Cr-C alloys, 50% of the oxygen was consumed for the oxidation of Cr and C. He stated that the rest of the oxygen might be consumed for the oxidation of Fe or leave the system unreacted. The latter does not seem to be realistic. To understand how the available oxygen is distributed to each species in this process, a more refined calculation is conducted below. It employs a mass balance, some assumptions about the relative rates of mass transfer of carbon and manganese, and some assumptions of local equilibrium at the metal-gas interface. The following detailed assumptions are made in calculations:

1. Given the excess oxygen relative to carbon and manganese in the bubble it is assumed that all the manganese is lost as MnO. (Note: approximately 3 to 5% of the manganese loss is likely from Mn vapor however, for the convenience of the calculation, it is assumed that the only mechanism responsible for manganese loss in the current work is oxidation to MnO)

2. All oxygen is consumed for oxidizing C, Mn, and Fe and the products are CO, CO_2, MnO, and FeO.
3. During the period in which carbon and manganese are actively being removed at the bubble surface, the following is true:
    a) The competition between Mn and C is controlled by their relative rates of mass transport in the metal; there is neither gas-phase nor slag-phase control.
    b) In keeping with the assumption of control by mass transport in the metal, all reactions are assumed to be in local equilibrium at the gas/metal interface.
    c) MnO and FeO form slag at the gas-metal interface which according to reference [34] is an ideal solution, therefore the sum of their activities is equal to 1.
    d) Again, during the active removal of Mn and C, the interfacial concentrations of manganese and carbon will be negligible in comparison to Fe so at the gas/metal interface $a_{Fe} \cong 1$.
4. After the active reaction is over it is expected that the melt composition at the gas/melt interface would recover to the bulk composition. It is worth noting that experimental observation suggests no change in the composition in the bubble in response to the change in the composition at the surface.

Based on the preceding assumptions, the primary equations required to describe the oxidation reactions are:

$$2n_{O_2} = n_{CO} + 2n_{CO2} + n_{MnO} + n_{FeO} \quad (4.1)$$

$$a_{FeO} + a_{MnO} = 1 \quad (4.2)$$

$$Fe + CO_2 = FeO + CO \qquad a_{FeO} = \frac{K_3\, a_{Fe} P_{CO_2}}{P_{CO}} \quad (4.3)$$

$$Mn + CO_2 = MnO + CO \qquad a_{MnO} = \frac{K_4\, a^i_{Mn} P_{CO_2}}{P_{CO}} \quad (4.4)$$

$$CO_2 + C = 2CO \qquad a^i_C = \frac{{P_{CO}}^2}{P_{CO_2}\, K_5} \quad (4.5)$$

$$MnO + C = Mn + CO \qquad a^i_{Mn} = \frac{K_6\ a^i_C\, a_{MnO}}{P_{CO}} \quad (4.6)$$

By simultaneously solving Equations 4.1 to 4.6, the values of n_{CO}, n_{CO2}, a_{MnO}, a_{FeO}, a^i_C, and a^i_{Mn} are obtained (see Table 4.3 and Table 4.4 for stages 1 and 3). The calculated oxygen partitioning for the formation of CO, CO_2, MnO, and FeO is provided in Figure 4.8. The total partitioning is 100% because Fe is assumed to react with the oxygen that did not react with Mn or C. There is much more CO than CO_2 in the gas, reflective of equilibrium with the melt interface. The various conditions in Figure 4.8 demonstrate that increasing oxygen in the gas mixture resulted in less CO and more FeO, CO_2, and MnO in both stages 1 and 3. Although the overall rate of decarburization increased with increasing oxygen in the gas mixture, gas mixtures containing lower oxygen were more efficient in decarburization and resulted in less FeO and MnO. The trend for CO is in agreement with the work of You *et al.* [28] for the bottom injection of Ar-O_2 into high carbon

ferromanganese and Dey *et al.* [35] for O_2-N_2 and Ohno *et al.* [36] for O_2-Ar blowing into Fe-Cr-C melt.

Table 4.2 Calculation of oxygen consumption in Fe-15Mn-1C alloys with the assumption of only CO and MnO formation.

Gas Flow Rate	Gas Composition	Number of moles of species per bubble			% Oxygen consumption for		% Excess oxygen after MnO and CO formation	
		n_{O_2}	n_{CO}	n_{MnO}	CO	MnO		
200 Nml/min	Ar-10% O_2	9.1×10^{-7}	8.4×10^{-7}	5.8×10^{-7}	46	32	22	Stage 1
				8.2×10^{-7}	46	45	9	Stage 3
	Ar-15% O_2	1.4×10^{-6}	1.0×10^{-6}	8.9×10^{-7}	38	32	30	Stage 1
				1.2×10^{-6}	38	45	17	Stage 3
	Ar-20% O_2	1.8×10^{-6}	1.2×10^{-6}	1.3×10^{-6}	33	35	32	Stage 1
				1.7×10^{-6}	33	46	21	Stage 3
300 Nml/min	Ar-6.7% O_2	7.6×10^{-7}	8.5×10^{-7}	4.3×10^{-7}	53	29	18	Stage 1
				6.7×10^{-7}	53	44	3	Stage 3
	Ar-10% O_2	1.1×10^{-6}	1.1×10^{-6}	7.2×10^{-7}	48	32	20	Stage 1
				1.0×10^{-6}	48	46	7	Stage 3
	Ar-15% O_2	1.7×10^{-6}	1.3×10^{-6}	1.1×10^{-6}	38	32	30	Stage 1
				1.6×10^{-6}	38	47	15	Stage 3

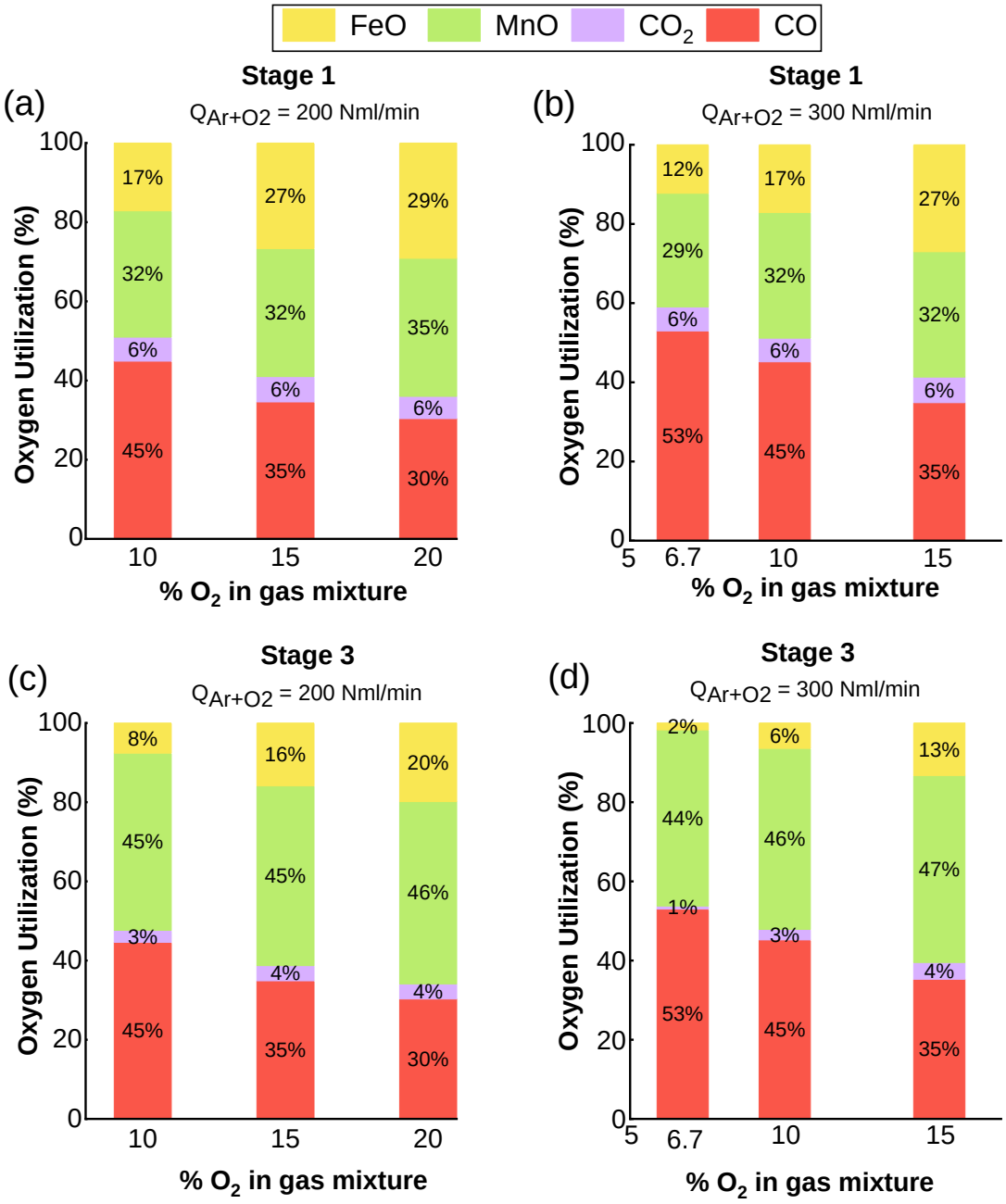

Figure 4.8. The calculated oxygen partitioning for MnO, CO, CO_2, and FeO formation in a) stage 1- total gas flow rate 200 Nml/min, b) stage 1-total gas flow rate 300Nml/min, c) stage 3-total gas flow rate 200Nml/min, d) stage 3-total gas flow rate 300 Nml/min.

4.4.4 Mass Transfer Coefficients for Mn and C

The mass transfer coefficients for C and Mn in the liquid were investigated using an approach suggested by Fruehan [24] where the ratio of rates of removal was almost equal to the concentration ratios. Likewise, in this work, it is assumed that the molar ratio of the rates of demanganization to decarburization is equal to the ratio of the flux of Mn to C in the liquid (Equation 4.7). The concentrations are written based on activities. The activity coefficient for carbon and manganese are calculated by Lee's [37] thermodynamic model for the liquid Fe-Mn-C system. For Mn, the activity coefficient is approximately 1 regardless of the carbon content. For carbon, only the activity coefficient of the bulk matters (0.71 and 0.67 for stages 1 and 3, respectively). Therefore, the values obtained for a^{i}_{Mn} and a^{i}_{C} from Section C, were substituted in Equation 4.7, and the ratio of mass transfer coefficients $\frac{k_{Mn}}{k_C}$ calculated for each gas flow rate and composition. This ratio and the interfacial concentrations of Mn and C are listed in Table 4.3 and Table 4.4 for stages 1 and 3 of the process.

$$\frac{J_{Mn}}{J_C} = \frac{k_{Mn}}{k_C}\frac{\left(C^{i}_{Mn} - C^{b}_{Mn}\right)}{\left(C^{i}_{C} - C^{b}_{C}\right)} \qquad (4.7)$$

J_{Mn} and J_C are the flux of Mn and C in the liquid in units of $\frac{mol}{cm^2 s}$. The mass transfer coefficients of Mn and C are represented as k_{Mn} and k_C in units of cm/s. The superscript "i" and "b" denote the interface and bulk, respectively.

Table 4.3 Calculation of interfacial concentrations and mass transfer coefficients for Fe-15Mn-1C alloy for stage 1.

Gas flow rate (Nml/min)	Vol.%O_2 in gas mixture	$\frac{p_{CO}}{p_{CO_2}}$	C^i_{Mn} (mol/cm^3)	C^i_C (mol/cm^3)	a_{FeO}	a_{MnO}	$\frac{k_{Mn}}{k_C}$
200	20	11	2.7×10^{-4}	1.7×10^{-5}	0.45	0.55	0.33
	15	11	2.7×10^{-4}	1.4×10^{-5}	0.43	0.57	0.26
	10	15	3.9×10^{-4}	1.4×10^{-5}	0.34	0.66	0.22
300	15	11	2.7×10^{-4}	2.6×10^{-5}	0.46	0.54	0.26
	10	15	4.5×10^{-4}	1.7×10^{-5}	0.35	0.65	0.21
	6.7	17	5.0×10^{-4}	1.3×10^{-5}	0.28	0.72	0.20

Table 4.4 Calculation of interfacial concentrations and mass transfer coefficients for Fe-15Mn-1C alloy for stage 3.

Gas flow rate (Nml/min)	Vol. %O_2 in gas mixture	$\frac{p_{CO}}{p_{CO_2}}$	C^i_{Mn} (mol/cm^3)	C^i_C (mol/cm^3)	a_{FeO}	a_{MnO}	$\frac{k_{Mn}}{k_C}$	Measured composition of the final slag	
								%FeO	%MnO
200	20	16	6.6×10^{-4}	3.3×10^{-5}	0.29	0.71	0.36	7.5	75
	15	18	6.5×10^{-4}	2.7×10^{-5}	0.25	0.75	0.32	---	---
	10	29	1.2×10^{-3}	3.4×10^{-5}	0.15	0.85	0.27	---	---
300	15	17	7.6×10^{-3}	3.1×10^{-5}	0.20	0.80	0.33	4	84
	10	34	1.4×10^{-3}	4.2×10^{-5}	0.12	0.88	0.25	---	---
	6.7	138	6.1×10^{-3}	1.7×10^{-4}	0.04	0.96	0.28	---	---

Compared to the concentration of Mn and C in the bulk liquid, 2×10^{-2} and 6×10^{-3} mol/cm^3, the gas/liquid interface concentrations can be considered negligible. This means that there is a steep concentration gradient in the liquid boundary layer. This observation confirms the assumption that at the point where the partitioning of oxygen to the different species is defined, the gas bubble is in equilibrium with the gas metal interface but far from equilibrium with the bulk metal. This seems quite likely during the period where manganese and carbon are being transported to the bubble to react with oxygen. However, as will be discussed in the next section, the period during which this is occurring appears to be a short fraction of the overall bubble lifetime, further suggesting that the concentrations of Mn and C at the bubble/melt interface will recover to their bulk values within the lifetime of the bubble. This in turn might lead one to expect a redistribution of elements in the bubble approaching equilibrium with the melt. Clearly, this did not happen as shown in Section 4.4.1. The authors are not able to offer a definitive explanation for the initial partitioning in the bubble not reverting to equilibrium but believe if the MnO had initially formed as a fume inside the bubble, it might not be in contact with the melt for reduction by carbon.

According to Table 4.3 and Table 4.4, the ratio of mass transfer coefficients for C and Mn was on average 3. This can be explained by the dependency of the mass transfer coefficient on the diffusivity presented as $k \propto D^n$ where power n typically varies from 0.5 to 1 [38,39]. Different researchers in the past have reported various diffusion coefficients for Mn in molten Fe or Fe-C_{sat} alloys as given in Table 4.5. According to Yagi *et al.* [40] and Ono *et*

al. [41], the effect of C on the diffusion coefficient of Mn is very small. Hence, the diffusion coefficient of Mn in liquid steel at 1823 K is taken by average as 4.4×10^{-5} cm^2/s which is 3 times smaller than that of C according to the literature. As a result, the calculated ratios of mass transfer coefficients in this work are in the expected range.

Table 4.5 Diffusion coefficients of C and Mn in molten Fe-C alloys.

Solvent	Diffusing element	wt% diffusing element	D× 10^5 $\frac{cm^2}{s}$ at 1823K	Authors
Fe-C	C	0- 2.5	1% C: 12	Mori *at al*. [42]
		0-saturation	1% C: 13 ($\pm$2)	Goldberg *et al.* [43]
		1.11 - 4.13	1% C: 12	Ono [44]
		0.31 - 3.68	1% C: 12.4	Wanibe *et al*. [45]
Fe-C_{sat}	Mn	0 -15	5 ($\pm$0.7)	Calderon [46]
		0-5.4	4.4 ($\pm$0.36)	Ono [41]
		2.5	3.9	Saito [47]
Pure Fe	Mn	0-10	4.5	Majdic [48]

To estimate the fraction of bubble lifetime over which active reaction is occurring, the individual mass transfer coefficients for manganese and carbon were assessed. It is assumed that k_C is 0.035 cm/s which is the average of reported values for carbon mass transfer to bubbles in liquid steel in the temperature range 1823 to 1873 K [11,15,21,49,50]; the mass transfer coefficient for Mn is assumed to be 3 times smaller. Based on these estimates the time required for decarburization and demanganization can be calculated as follows. Knowing the amount of C or Mn removed per bubble and using the calculated mass transfer coefficients, the reaction time is estimated to be approximately 0.001 seconds. This is about 1% of the residence time of the bubble in the liquid. In the present work, determination of the actual mass transfer coefficient is not possible because the reactions of Mn and C with

O_2 are over within times considerably less than the residence time of the bubble in the liquid. This suggests that in this system the ability for C to reduce MnO back into melt is not very strong. The authors cannot offer a definitive explanation for this but if MnO forms as a fume inside the bubble the contact between MnO and carbon in the liquid would be minimal. In other work by the authors [51] the concentration of manganese and carbon versus time were not affected by the depth of submergence of the lance. This supports the findings of the current work that the time for the reaction of manganese and carbon with oxygen is much shorter than the residence time of the bubble in the liquid.

It is worth reflecting on one of the major assumptions in the forgoing calculations, that all manganese is oxidized to MnO in the bubble. This assumption is contrary to the authors' previous work [33] where to justify the total loss the authors had to assume a significant contribution from manganese vapor and an evaporation-condensation mechanism. To understand why such a mechanism did not operate in the current work one must consider the role of carbon. In the current work, the carbon concentration is 1% whereas in the previous work carbon was less than 0.42%. In this paper, it has been established that the competition for oxygen is controlled by the relative rates of mass transport of carbon and manganese in the steel. Hence, one might expect that for the same manganese concentrations a higher carbon concentration would lead to less MnO formation. Figure 4.9 shows the contribution to the rate of manganese loss by a combination of vapor and by evaporation-condensation. This value is plotted against the rate of heat production based on the oxide species formed. From this Figure, it is clear that the heat available for

evaporation-based mechanisms is less for higher carbon alloys and negligible for 1% C alloy considered in the current work. The effect of carbon on manganese loss by mechanisms involving vapor is qualitatively consistent with the effect of carbon on decreasing the heat generated by the oxidation of manganese. The detailed behavior differs from stage 1 to stage 3, but the overall effect of carbon is similar. The authors are not currently able to offer an explanation for the difference between the stages.

For two experiments in this work, the final composition of slag was analyzed by ICP for their Mn and Fe content. Assuming that the oxides in the slag are present as MnO and FeO, their corresponding weight percent is calculated and given in Table 4.4. The measured amounts of MnO in the final slag are in fair agreement with the calculated activities of MnO. However, the amounts of measured FeO are different from their calculated activities and the total amount of oxides does not reach 100%.

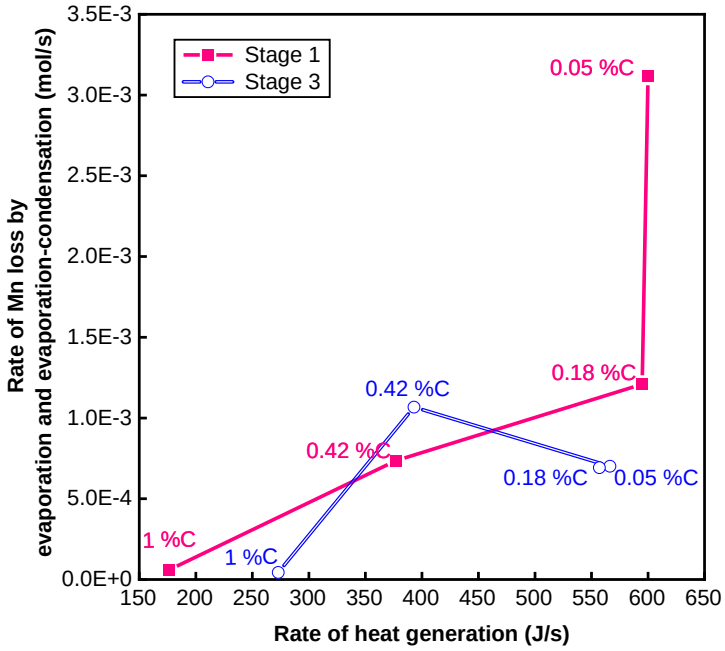

Figure 4.9 Rate of manganese losses as metallic manganese due to evaporation and evaporation-condensation versus the rate of heat generation for Fe-15Mn alloys.

4.5 Conclusions

The effect of gas composition and flow rate on the rate of decarburization and demanganization of Fe-15Mn-1C alloys at 1823 K was studied experimentally and thermodynamically.

1. The competition between Mn and C for oxygen is controlled by the ratio of mass transfer coefficients for these elements in the metal.
2. For the 1% C alloy considered in this work, Mn loss occurred almost entirely as MnO dust rather than as a combination of MnO and mechanisms involving vapor as seen in previous work for lower carbon alloys. The absence of evaporation-related mechanisms appears to be related to the higher carbon content decreasing

the amount of MnO formed thereby decreasing the heat generated and therefore decreasing the amount of vapor that could be produced.

3. Based on the estimated mass transfer coefficient for either C or Mn, the reaction time for each bubble was 0.001 seconds which is about 1% of the residence time of the bubble in the liquid.
4. The AOD mechanism did not play a major role in the current work where the competition for oxygen was dominated by mass transport. This mechanism is similar to that proposed by Fruehan for Cr, however, the repartitioning of species towards the equilibrium suggested by Fruehan does not seem to have operated in this case. This would appear to be in contradiction to the very short reaction time highlighted in conclusion 3 which would have suggested a fairly rapid repartitioning, but if the form of manganese oxide was as fine dust there might be insufficient contact with the melt for rapid repartitioning. It is still possible that in a deep bath there would be sufficient time for MnO to be reduced back into the melt.

4.6 Acknowledgments

The authors gratefully acknowledge financial support from the Natural Sciences and Engineering Research Council of Canada. Additional thanks go to ArcelorMittal Dofasco, Stelco, Praxair, and Hatch Ltd. for in-kind support and technical expertise.

4.7 References

1 B. C. De Cooman, K. Chin, and J. Kim: in *New Trends and Developments in*

Automotive System Engineering, 2011, pp. 101–28.

2 R. Elliott, K. Coley, S. Mostaghel, and M. Barati: *JOM*, 2018, vol. 70, pp. 680–90.

3 O. Bouaziz, S. Allain, C.P. Scott, P. Cugy, and D. Barbier: *Curr. Opin. Solid State Mater. Sci.*, 2011, vol. 15, pp. 141–68.

4 *POSCO, POSCO Steel Plates*, Pohang, South Korea, unpublished research, 2014.

5 *POSCO, New Materials: High Mn Steels*, Pohang, South Korea, unpublished research, 2015.

6 *Thyssenkrupp, Precision Steel, Precidur ® X40MnCrAlV 19-2 HY, Product Information for Hot-Rolled Precision Strip Made in Hohenlimburg*, Germany, Hohenlimburg, unpublished research, 2019.

7 W. Dresler: in *Steelmaking Conference Proceedings*, 1989, pp. 13–20.

8 D.S. Kozak and L.R. Matricardi.: *Iron Steelmak.*, 1981, vol. 8, pp. 28–31.

9 T. Germershausen, J. Bader, J. Reichel, U. Gerike, and S.M.S.S. Ag: in *The thirteenth International Ferroalloys Congress Efficient technologies in ferroalloy industry*, Almaty, Kazakhstan, 2013, pp. 335–46.

10 T. Ohno and T. Nishida: *Tetsu-to-Hagane*, 1977, vol. 63, pp. 2094–9.

11 R.J. Fruehan: *Ironmak. Steelmak.*, 1976, vol. 3, pp. 153–8.

12 N. Andersson, A. Tilliander, L. Jonsson, and P. Jönsson: *Steel Res. Int.*, 2012, vol.

83, pp. 1039–52.

13 J. Wei, H. Zhu, Q. Jiang, G. Shi, H. Chi, and H. Wang: *ISIJ Int.*, 2010, vol. 50, pp. 1347–56.

14 G.S. Rao and D.G.C. Robertson: in *Advanced Processing of Metals And Minerals, The Minerals, Metals & Materials Society (TMS)*, 2006, pp. 325–42.

15 T.D. Roy and D.G.C. Robertson: *Ironmak. Steelmak.*, 1978, vol. 5, pp. 198–206.

16 T.D. Roy, D.G.C. Robertson, and J.C.C. Leach: *Ironmak. Steelmak.*, 1978, vol. 5, pp. 207–10.

17 J.-H. Wei and D.-P. Zhu: *Metall. Mater. Trans. B*, 2002, vol. 33, pp. 111–9.

18 S. Asai and J. Szekely: *Metall. Trans.*, 1974, vol. 5, pp. 651–7.

19 J. Szekely and S. Asai: *Metall. Trans.*, 1974, vol. 5, pp. 1573–80.

20 J. Reichel and J. Szekely: *Iron Steelmak.*, 1995, vol. 22, pp. 41–8.

21 R. J. Fruehan: *Ironmak. Steelmak.*, 1976, vol. 3, pp. 33–7.

22 W.A. Krivsky: *Metall. Trans.*, 1973, vol. 4, pp. 1439–47.

23 J.M. Saccomano, R.J. Choulet, and J.D. Ellis: *J. Met.*, 1969, vol. 21, pp. 59–64.

24 R.J. Fruehan: *Met. Trans. B*, 1975, vol. 6, pp. 573–8.

25 K. Yamamoto, T. Mimura, S. Ito, and T. Onoye: *Tetsu-to-Hagane*, 1986, vol. 72, pp. 1034–46.

26 Y.E. Lee and L. Kolbeinsen: *ISIJ Int.*, 2005, vol. 45, pp. 1282–90.

27 B.-D. You: *J. Korean Institue Met. Mater.*, 1995, vol. 33, pp. 1508–13.

28 B.-D. You, J. Han, and J. Pak: *Steel Res.*, 2000, vol. 71, pp. 22–6.

29 B.-D. You, K.-Y. Park, J.-J. Pak, and J.-W. Han: *Met. Mater.*, 1999, vol. 5, pp. 395–9.

30 B.-D. You, B.-W. Lee, and J.-J. Pak: *Met. Mater.*, 1999, vol. 5, pp. 497–502.

31 E.T. Turkdogan, P. Grieveson, and L.S. Darken: *J. Am. Chem. Soc.*, 1963, vol. 67, pp. 1647–54.

32 H. Liu, J. Liu, J. Schenk, F.M. Penz, L. Sun, R. Zhang, and Z. An: *Metall. Mater. Trans. B*, 2020, vol. 51, pp. 756–62.

33 A. Rafiei, G.A. Irons, and K.S. Coley: *Steel Res. Int.*, DOI:10.1002/srin.202000480.

34 F. Oeters, K. Koch, R. Scheel, and U. Noelle: *Arch Eisenhuettenwes*, 1977, vol. 48, pp. 475–80.

35 S.K. Dey and D.N. Ghosh: *Metall. Mater. Trans. B*, 1976, vol. 7, pp. 43–8.

36 R. Tsujin, M. Hirai, T. Ohno, N. Ishiwata, and Tsutomu Inoshita: *ISIJ Int.*, 1989, vol. 29, pp. 291–9.

37 Y.E. Lee: *Metall. Mater. Trans. B*, 1998, vol. 29, pp. 397–403.

38 G.F. Versteeg, P.M.M. Blauwhoff, and W.P.M. VAN Swaaij: *Chem. Eng. Sci.*, 1987, vol. 42, pp. 1103–19.

39 J. Wei and H. Zuo: *Steel Reseach Int.*, 2007, vol. 78, pp. 863–75.

40 T. Yagi, Y. Ono, and M. Ushijima: *Tetsu-to-Hagane*, 1970, vol. 56, pp. 1640–5.

41 Y. Ono and S. Matsumoto: *Trans. JIM*, 1975, vol. 16, pp. 415–22.

42 H. Nomura and K. Mori: *Tetsu to Hagane*, 1969, vol. 55, pp. 1134–41.

43 D. Goldberg and G.R. Belton: *Metall. Trans.*, 1974, vol. 5, pp. 1643–8.

44 Y. Ono: *Tetsu-to-Hagane*, 1977, 63, vol. 63.

45 Y. Wanibe, S. Takai, T. Kojima, and H. Sakao: *Trans. Iron Steel Inst. Japan*, 1980, vol. 20, pp. 783–9.

46 F.P. Calderon, N. Sano, and Y. Matsushita: *Metall. Mater. Trans. B*, 1971, vol. 2, pp. 3325–32.

47 T. Saito, Y. Kawai, K. Maruya, and M. Maki: *Sci. Reports Res. Institutes, Tohoku Univ. Ser. A, Physics, Chem. Metall.*, 1959, vol. 11, pp. 401–10.

48 A. Majdic, D. Graf, and H. Schenck: *Arch. für das Eisenhüttenwes*, 1969, vol. 40, p. 627.

49 J.O.H. Park, D.S. Kim, and S. Lee: 2005, vol. 36, pp. 67–73.

50 O.K. Tokovoi, A. V Tokarev, A.N. Volkadaev, S.N. Prokofev, and A.N. Komarov:

Izvvestiya Ross. Akad. Nauk. Met., 1995, vol. 3, pp. 10–4.

51 A. Rafiei, G.A. Irons, and K.S. Coley: *Metall. Mater. Trans. B, Under Review*.

4.8 Additional Information about Chapter 4:

An example of solving simultaneous equations 4.3 to 4.8 for stage 1 of the process under the condition that the total gas flow rate is 200 Nml/min and gas composition is Ar-15%O_2. (To make it easier to follow the solution, equations' numbers are different from the paper).

It is known from experimental data that the removed carbon is:

$$n_{C,tot\,removed} = n_{CO} + n_{CO2} = 0.0192 \quad (1)$$

$2n_{O_2} = 0.051$ and n_{MnO} from experiments is 0.0164. Substituting these values in mass balance Equation 2 gives:

$$2n_{O_2} = n_{CO} + 2n_{CO_2} + n_{MnO} + n_{FeO} \quad (2)$$

$$n_{CO_2} + n_{FeO} = 0.0152 \quad (3)$$

It is assumed that sum of MnO and FeO activities is equal to 1:

$$a_{MnO} + a_{FeO} = 1 \quad (4)$$

The equilibrium constant of Equation (5) is written to express the activity of FeO.

It is assumed that the activity of Fe is 1. Therefore:

$$Fe+CO_2=FeO+CO; \qquad a_{FeO} = \frac{k_5 . a_{Fe} p_{CO_2}}{p_{CO}} = \frac{5.3\times1\times n_{CO_2}}{n_{CO}} \quad (5)$$

The equilibrium constant of Equation (6) is written to express the activity of MnO.

$$Mn+CO_2=MnO+CO; \qquad a_{MnO} = \frac{k_6 . a^i_{Mn} p_{CO_2}}{p_{CO}} = \frac{2854 a^i_{Mn} n_{CO_2}}{n_{CO}} \quad (6)$$

Substituting Equations 5 and 6 in Equation 4 yields:

$$\frac{5.3 \times 1 \times \mathrm{n_{CO_2}}}{\mathrm{n_{CO}}} + \frac{2854 a_{Mn}^{i} n_{CO_2}}{n_{CO}} = 1 \tag{7}$$

Bring $\frac{n_{CO}}{n_{CO_2}}$ to the right side, and substitute n_{CO_2} from Equation 1 gives:

$$5.3 + 2854 a_{Mn}^{i} = \frac{n_{CO}}{n_{CO_2}} = \frac{n_{CO}}{0.0192 - n_{CO}} \tag{8}$$

The equilibrium constant of Equation 9 can be written to express the activity of manganese at the interface of gas and metal ($\mathrm{a^i_{Mn}}$):

$$\mathrm{MnO+C=Mn+CO;} \qquad \mathrm{a^i_{Mn}} = \frac{\mathrm{k_9.a_{MnO}a^i_C}}{\mathrm{p_{CO}}} = \frac{5.03 \times \mathrm{a_{MnO}a^i_C}}{\mathrm{p_{CO}}} \tag{9}$$

Where:

$$\mathrm{a_{MnO}} = \frac{\mathrm{n_{MnO}}}{(\mathrm{n_{MnO}+n_{FeO}})} = \frac{0.0164}{(0.0164+(0.0152-\mathrm{n_{CO_2}}))} = \frac{0.0164}{\left(0.0164+\left(0.0152-(0.0192-\mathrm{n_{CO}})\right)\right)} = \frac{0.0164}{(0.0124+\mathrm{n_{CO}})} \tag{10}$$

Substituting Equation 10 in Equation 9 gives:

$$\mathrm{a^i_{Mn}} = \frac{5.03 \times \mathrm{a_{MnO}a^i_C}}{\mathrm{p_{CO}}} = \frac{5.03 \times \frac{0.0164}{(0.0124 + \mathrm{n_{CO}})} \times \mathrm{a^i_C}}{\mathrm{p_{CO}}} \tag{11}$$

The equilibrium constant of Equation 12 can be written to express the activity of carbon at the interface of gas and metal ($\mathrm{a^i_C}$):

$$\mathrm{CO_2+C=2CO;} \quad \mathrm{a^i_C} = \frac{\mathrm{p_{CO}}^2}{\mathrm{p_{CO_2}.K_{12}}} = \frac{\mathrm{p_{CO}}^2}{\mathrm{p_{CO_2}} \times 14889} \tag{12}$$

Substituting $\mathrm{a^i_C}$ from equation 12 in Equation 11 yields:

$$a^{i}_{Mn} = \frac{5.03 \times \frac{0.0164}{(0.0124 + n_{CO})} \times \frac{{p_{CO}}^2}{p_{CO_2} \times 14889}}{p_{CO}} = \frac{5.5 \times 10^{-6}}{(0.0124 + n_{CO})} \frac{p_{CO}}{p_{CO_2}} \quad (13)$$

$a^{i}_{Mn}$from Equation 13 can be substituted in Equation 8 which gives:

$$5.3 + 2854\left(\frac{5.5 \times 10^{-6}}{(0.0124 + n_{CO})} \frac{p_{CO}}{p_{CO_2}}\right) = \frac{n_{CO}}{0.0192 - n_{CO}} \quad (14)$$

The ratio of partial pressures of CO/CO_2 is equal to their ratio of numbers of moles:

$$\frac{p_{CO}}{p_{CO_2}} = \frac{n_{CO}}{n_{CO_2}} = \frac{n_{CO}}{0.0192 - n_{CO}} \quad (15)$$

$\frac{p_{CO}}{p_{CO_2}}$ from Equation 15 can be substituted in Equation 14 which gives equation 16

with only 1 unknown (n_{CO}):

$$5.3 + 2854\left(\frac{5.5 \times 10^{-6}}{(0.0124 + n_{CO})} \frac{n_{CO}}{(0.0192 - n_{CO})}\right) = \frac{n_{CO}}{0.0192 - n_{CO}} \quad (16)$$

Therefore,

$$n_{CO} = 0.018 \text{ moles}$$

As a result,

$$n_{CO2} = 0.0016 \text{ moles}$$

The number of moles of argon is $n_{Ar} = 0.14$, hence:

$$p_{CO} = \frac{0.018}{0.018+0.0016+0.14} = 0.11 \text{ atm} \quad , \quad p_{CO2} = 0.010 \text{ atm}$$

The number of moles of FeO can be found from Equation 3:

$$n_{FeO} = 0.014 \text{ moles}$$

From Equation 12 $\quad a_C^i = 7.8 \times 10^{-5}$

From Equation 11 $\quad a_{Mn}^i = 2 \times 10^{-3}$

To obtain the concentration of carbon at the interface (C_C^i), Equation 17 can be used where C_{st} is the concentration of steel, X_C^i is the mole fraction of carbon at the interface of gas-metal, and γ_C is the activity coefficient of carbon calculated by Lee's [39] thermodynamic model.

$$C_C^i = C_{st}.X_C^i = C_{st}\frac{a_C^i}{\gamma_C} = \frac{6.12\ mol}{\left(\frac{330\ g}{7\frac{g}{cm^3}}\right)} \times \frac{7.8\times10^{-5}}{0.7} = 1.4 \times 10^{-5}\ \frac{\text{mol}}{\text{cm}^3} \tag{17}$$

Similarly, the concentration of manganese at the interface (C_{Mn}^i) is calculated:

$$C_C^i = C_{st}.X_C^i = C_{st}\frac{a_C^i}{\gamma_C} = \frac{6.12\ mol}{\left(\frac{330\ g}{7\frac{g}{cm^3}}\right)} \times \frac{2\times10^{-3}}{0.98} = 2.7 \times 10^{-4}\ \frac{\text{mol}}{\text{cm}^3} \tag{18}$$

The activity of FeO and MnO will be equal to:

$$a_{FeO} = 0.43 \ , \quad a_{MnO} = 0.57$$

So far, all the calculations were based on thermodynamics. Now, assuming that the ratio of the manganese to carbon removal is equal to their ratio of fluxes, with knowing interfacial values, the ratio of mass transfer coefficients $\left(\frac{k_{Mn}}{k_C}\right)$ can be found readily:

$$\frac{J_{Mn}}{J_C} = \frac{\frac{dn_{Mn}}{dt}}{\frac{dn_C}{dt}} = 0.86 = \frac{k_{Mn}}{k_C}\frac{\left(C^i_{Mn} - C_{Mn}\right)}{\left(C^i_C - C_C\right)} = \frac{k_{Mn}}{k_C}\frac{C_{st}\left(X^i_{Mn} - X_{Mn}\right)}{C_{st}\left(X^i_C - X_C\right)} = \frac{k_{Mn}}{k_C} \times 3.2 \qquad (19)$$

$$\frac{k_{Mn}}{k_C} = \frac{0.86}{3.2} = 0.26$$

Chapter 5

5 Argon Oxygen Decarburization of High Manganese Steels: Effect of Temperature, Alloy Composition, and Submergence Depth

This chapter served to communicate a significant collection of experimental data gathered entirely by me. All data analysis and manuscript drafting were completed by me. Discussions were shared between me and Dr. Kenneth S. Coley and Dr. Gordon A. Irons. The manuscript was edited, and revised by Dr. Kenneth S. Coley, and reviewed to the final version by Dr. Gordon A. Irons. The manuscript of this work has been submitted to Metallurgical and Materials Transactions B.

Abstract

In this study, decarburization and manganese losses from Fe-Mn-C steels containing 10, 15, and 25% Mn steels and 0.18 and 0.42%C during Ar-O_2 bubbling in the temperature range of 1823 to 1913 K were studied. The results showed that higher temperature resulted in a higher rate of decarburization because of more oxygen partitioned to carbon oxidation than to manganese. Manganese loss was explained by considering multiple mechanisms; oxide formation and vapor formation, and evaporation-condensation. Manganese loss increased at higher temperatures which have been attributed to an increase in vapor pressure. Changing the depth of lance submergence did not make any difference in the decarburization and manganese loss, the reactions occurred well within the time the bubble was present in the melt. Prolonged time after reaction did not lead to a repartitioning of the species. Comparison of thermodynamic calculations with experimental observations

showed that manganese and carbon in the bulk metal were not in equilibrium with the gas species in the bubble. After the bubble reacted near the lance tip, the system did not proceed to true equilibrium.

5.1 Introduction

The automotive industry is facing increasing global demand to comply with environmental regulations and fuel efficiency. This has driven steelmakers to fulfill these requirements by the development of new high strength steels with improved mechanical properties [1-4]. Manganese is a critical alloying element for advanced high strength steels due to its ability to improve mechanical properties such as toughness and ductility. The manganese concentration in TWIP and TRIP steels varies between 5 to 30% [5-7] while the carbon concentration is required to be less than 0.5% [8]. Numerous researches have been conducted regarding the mechanical properties and microstructure of these alloys [9,10]. However, published data about the processing of these steels is scarce.

Decarburization of liquid iron-manganese alloys is challenging due to the high vapor pressure of manganese and its affinity for oxygen. There has been more work on ferromanganese alloys that are used as alloy additions to make manganese-containing steels. Manganese oxygen refining (MOR) with a similar concept of basic oxygen furnace (BOF) allows the production of medium and low carbon ferromanganese by blowing oxygen through a lance or bottom tuyeres into high carbon ferromanganese [11]. The carbon concentration of 0.5-1% can be achieved if the temperature rises to above 1750℃. However, this leads to undesirable manganese losses by evaporation and oxidation which

can be as high as 5% [12]. To achieve the decarburization to meet metallurgical requirements, it is necessary to use argon to dilute the blown oxygen [13]. Hence, argon oxygen decarburization (AOD) is a vital step after melting the materials in the electric arc furnace (EAF), (the so-called EAF-AOD route) to economically produce high manganese steels with rapid decarburization while avoiding excessive loss of manganese. The manganese losses could be compensated by the addition of ferrosilicon during the reduction stage of AOD [14]. The AOD was first commercialized for stainless, which has been well-researched [15-20], whereas there are only a few published works on the argon-oxygen processing of ferromanganese alloys [21-24]. Yamamoto *et al*. [25] decarburized molten Fe-76Mn-7C alloys to 0.5-1% C with Ar-O_2 blowing in a combined converter with a top lance for O_2 blowing and a bottom plug for Ar stirring or Ar+O_2 injection. The total manganese loss was reported to be about 3-4% due to oxidation and evaporation. As reported by Lee *et al*. [26] decarburization of high carbon ferromanganese proceeds in a series of sequential stages. According to these workers, in the first of three stages, the rate is controlled by the chemical reaction between oxygen and carbon at the interface between the gas and the metal. The reaction is controlled by the rate of supply of oxygen in the middle stage. In the final stage, at low carbon levels, the rate of mass transfer of carbon in the liquid to the gas/liquid interface was controlling. These researchers proposed that a portion of oxygen that is not used for the decarburization, will react with manganese vapor and form MnO mist beyond the surface of the metal according to the fuming mechanism proposed by Turkdogan *et al*. [27]. You *et al*. [21-24] have studied the decarburization of high carbon

ferromanganese both in laboratory scale and pilot converters. These workers reported that the efficiency of oxygen for carbon removal improved with decreasing concentration of oxygen in Ar-O_2 gas mixtures and with increasing temperature.

Furthermore, the evaporative and oxidative losses of manganese were reported to be in the range of 2-25% in the combined blowing converter. These workers did not determine the contribution of each of these mechanisms for Mn loss. Liu *et al*. [28] carried out a laboratory study of the decarburization and manganese loss from Fe-16Mn-3C alloys by injection of CO_2-O_2 showing that the introduction of CO_2 to oxygen increased the rate of decarburization while helping Mn retention in the melt.

The current paper is a part of a larger experimental study that seeks to understand the kinetics and mechanisms of the decarburization and manganese losses from high manganese steels during Ar-O_2 bubbling. A previous paper by authors [29] investigated the effect of alloy chemistry on decarburization and manganese losses. It has been shown that the total manganese loss in the processing of Fe-Mn-C alloys containing 10 to 25%Mn and 0.05 to 0.42%C was higher than being explained only as vapor and oxide. An evaporation-condensation mechanism was proposed and Mn evaporates in equilibrium with Mn in the metal and condenses at a lower temperature inside the bubble. This mechanism can work only if there is sufficient temperature gradience between the bubble surface and its interior. It was demonstrated that this mechanism works both from a thermodynamic and kinetic point of view. In a further study by current authors [30], it has been shown that increasing the gas flow rate and oxygen fraction in the gas mixture led to higher rates of

decarburization and manganese losses from Fe-15Mn-1C alloys. The efficiency of oxygen for the decarburization increased with lowering oxygen in the gas mixture, indicating that the AOD mechanism worked. The rate of supply of oxygen was rate determining. However, the competition between carbon and manganese for oxidation was the main controlling step. Unlike the previous study for lower range carbon alloys, assuming that products of oxidation were CO and MnO there was a considerable amount of unconsumed oxygen. Based on mass balance it has been shown how oxygen is distributed among CO, CO_2, MnO, and FeO. The current paper studies the effect of temperature, alloy composition, and submergence depth on decarburization and manganese losses.

5.2 Experimental Methods

The experimental procedure in this paper is the same as previous work by authors [29,30], but have repeated the description here for the convenience of the reader. The experiments were conducted in a resistant heated vertical tube furnace (Figure 5.1) in the temperature range of 1550 to 1640℃ (1823 to 1913K). The temperature was controlled using a type-B platinum-rhodium thermocouple within ±8K. There was an alumina working tube with a diameter of 7.9 cm which was sealed using O-rings and water-cooled stainless steel caps at both ends allowing to evacuate the furnace using a vacuum pump (at the top end) or argon for purging being introduced to the furnace from bottom end. Six alloy compositions were used in this work. Fe–Mn–C containing 10, 15, and 25%Mn and 0.18 and 0.42%C. The desired amount of manganese flakes (99.990% purity), electrolytic iron powder (99.977% purity), and graphite rods (99.9999% purity) were mixed to prepare the alloys. Prior to

mixing alloys, manganese flakes were acid pickled with 5% HCl solution to remove the surface oxide layer. The mass of alloys was 330 grams in all experiments. The alloy was placed in an alumina crucible with 3.8 cm inner diameter, 4 cm outer diameter, and height of 9 cm and raised to the hot zone of the furnace. Before each experiment, the furnace was sealed and evacuated to the range of 80–150 millitorr and backfilled with argon. Ar purging was continued until the end of the experiment to avoid oxidation of the liquid metal. When the target temperature for each experiment was reached, one hour was given to ensure that melt is homogenized. Then, a single-bore alumina tube with an outer diameter of 0.48 cm and an inner diameter of 0.16 cm was lowered into the melt so that submergence depth was reached the desired one (depending on the experiment, either 1, 2, 2.5, and 3 cm). Then bubbling of Ar-O_2 mixture started at the total flow rate of 300 Nml/min and composition of Ar-6.7%O_2 for all experiments. The metal samples were taken frequently and analyzed by ICP-OES for manganese content and by LECO for carbon content. Also, at the end of the experiments fume samples were collected from the wall and cap of the furnace and analyzed by ICP-OES for their manganese and iron content.

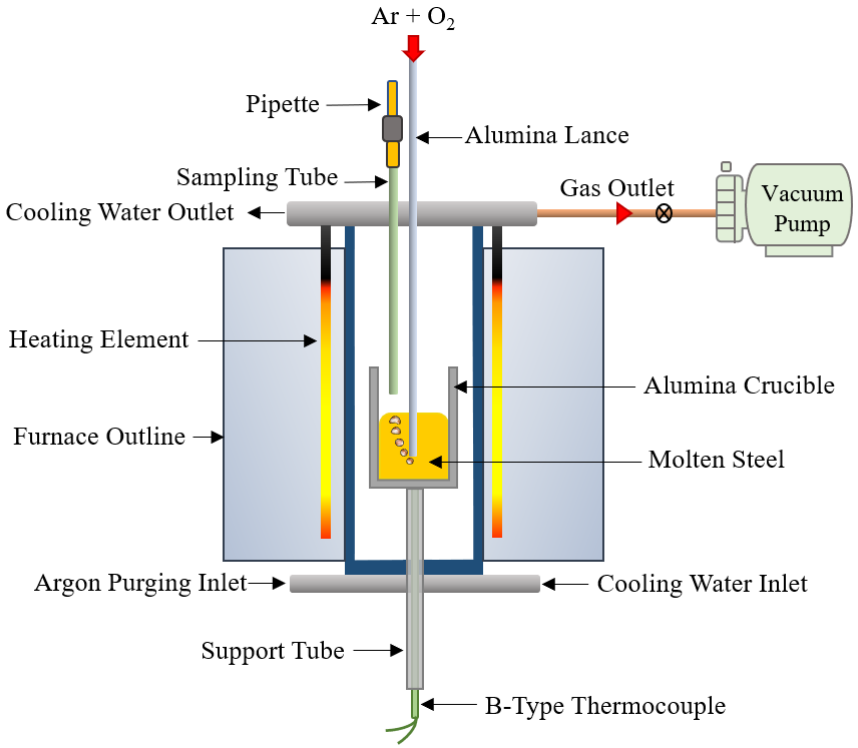

Figure 5.1 Schematic diagram of the experimental setup, not to scale.

5.3 Results

5.3.1 Effect of Temperature on Manganese Loss and Decarburization

To study the effect of temperature on the rate of manganese loss, experiments were carried at 1823, 1893, and 1913 K. The total gas flow rate and composition were 300 Nml/min and Ar-6.7%O_2. The submergence depth was 3 cm. Figure 5.2 (a-c) and Figure 5.3 (a-c) show the change of manganese concentration in the bath versus time for Fe -0.18C and Fe-0.42C, respectively. Figures a, b, and c correspond to the manganese concentrations of 25, 15, and 10%, respectively. The pattern of manganese behavior is similar for all temperatures and compositions. Initially, there was a manganese loss at a constant rate, followed by a reversion or plateau in the middle stage and another manganese loss at a constant rate in

the final stage. Increasing temperature led to a faster rate of Mn loss and shorter middle stage. Consequently, at 1893 and 1913 K, manganese loss in stage 3 started earlier compared to that at1823 K. You *et al.* [22] did not present the Mn versus time data for various temperatures in Ar-O_2 bubbling to Fe-75Mn-6C alloys, they reported that the rate of manganese loss increased with temperature. Liu *et al.* [28] also observed higher rates of Mn loss at higher temperatures during CO_2-O_2 injection into Fe-16Mn-3C alloys.

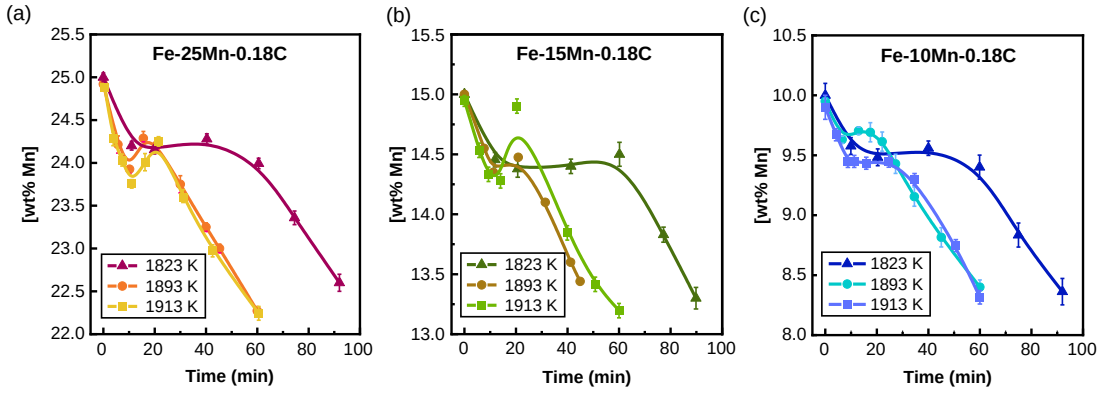

Figure 5.2. Manganese concentration in the bath versus time for a) Fe-25Mn-0.18C, b) Fe-15Mn-0.18C, and c) Fe-10Mn-0.18C alloys, Gas flow rate: 300Nml/min and gas composition: Ar-6.7%O_2, submergence depth: 3cm, variable: temperature.

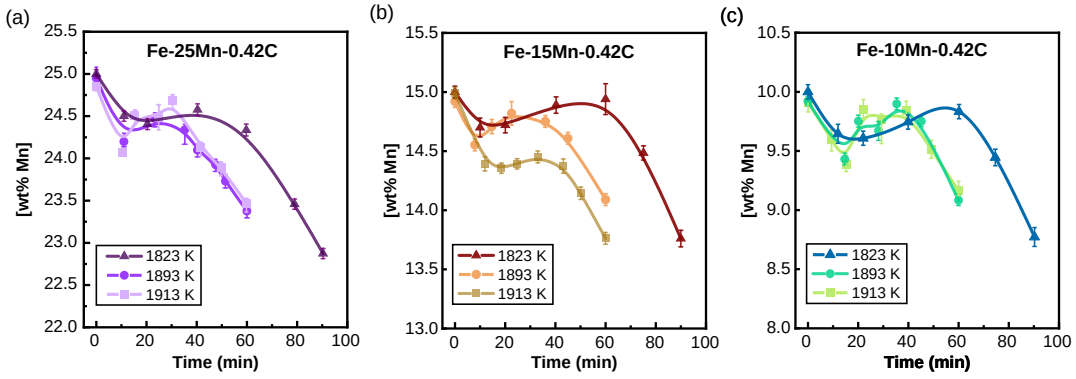

Figure 5.3. Manganese concentration in the bath versus time for a) Fe-25Mn-0.42C, b) Fe-15Mn-0.42C, and c) Fe-10Mn-0.42C alloys, Gas flow rate: 300Nml/min and gas composition: Ar-6.7%O_2, submergence depth: 3cm, variable: temperature.

Figure 5.4 (a-c) illustrate the decarburization of the Fe-25Mn-0.18C, Fe-15Mn-0.18C, and Fe-10Mn-0.18C alloys for the various temperatures. Similarly, Figure 5.5 (a-c) show the decarburization of the Fe-25Mn-0.42C, Fe-15Mn-0.42C, and Fe-10Mn-0.42C alloys. Increasing temperature resulted in higher rates of decarburization. Depending on the initial manganese concentration, if enough bubbling time is given, Fe-0.42C alloys can decarburize to 0.18% or lower carbon concentrations. For example, the final carbon content of Fe-15Mn-0.42C alloy at 1913 K in is 0.17% (Figure 5.5(b)). Also, the end carbon of Fe-10Mn-042C in 1823 and 1913 K was 0.165 and 0.128%C (Figure 5.5(c)). The effect of temperature on the rate of decarburization is consistent with You *et al*. [22] and Liu *et al*. [28] work.

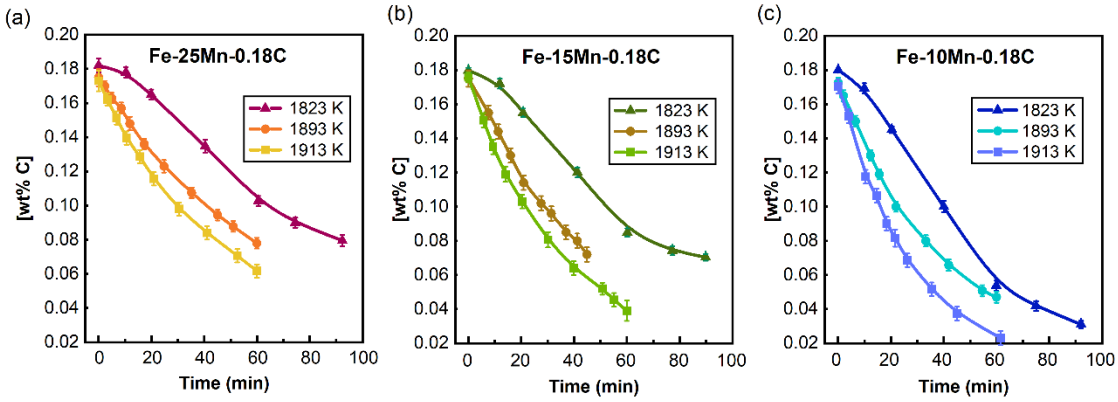

Figure 5.4. Carbon concentration in the bath versus time for a) Fe-25Mn-0.18C, b) Fe-15Mn-0.18C, and c) Fe-10Mn-0.18C alloys, submergence depth: 3cm, variable: temperature.

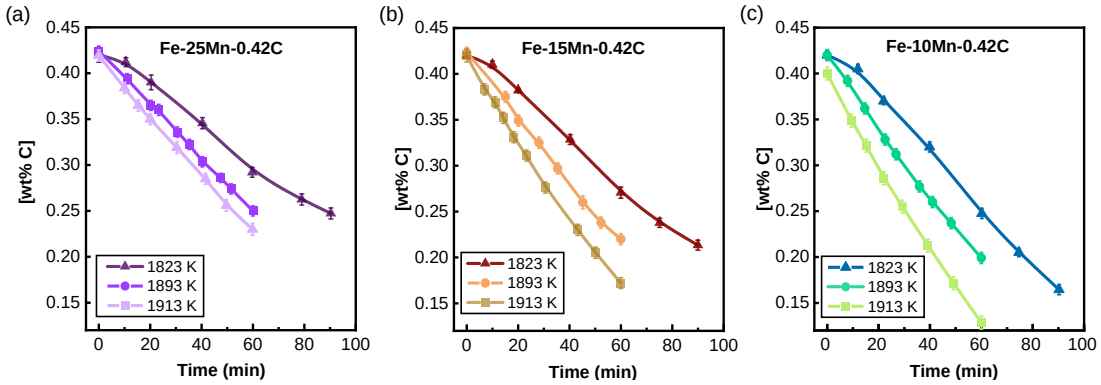

Figure 5.5. Carbon concentration in the bath versus time for a) Fe-25Mn-0.42C, b) Fe-15Mn-0.42C, and c) Fe-10Mn-0.42C alloys, submergence depth: 3cm, variable: temperature.

5.3.2 Effect of Alloy Composition

Figure 5.6 (a-g) show decarburization versus time for 25, 15, and 10% Mn concentrations. In each case, the temperature was maintained constant and the gas flow rate and gas composition were 300 Nml/min and Ar-6.7%O_2. The depth of submergence in all these experiments was 3 cm. Manganese concentrations were 10, 15, and 25%. As indicated, in all cases the rate of decarburization increased with decreasing initial manganese concentration. This trend is applied to both Fe-0.18C and Fe-0.42C alloys. As observed in

Figure 5.6 (a-c), decarburization of alloys Fe-0.18C at all temperatures followed a curve shape and the rate of decarburization slowed down with the carbon concentration in the bath. However, alloys Fe-.042C exhibited a linear pattern with a constant rate for a given Mn concentration at 1893 and 1913 K (Figure 5.6 (e) and Figure 5.6 (f)). Alloy Fe-0.42C at 1823 K was an exception, where the rate of decarburization was slow in the first stage. Then, the rate increased in the middle stage and finally decreased with the carbon content in the bath (Figure 5.6 (d)).

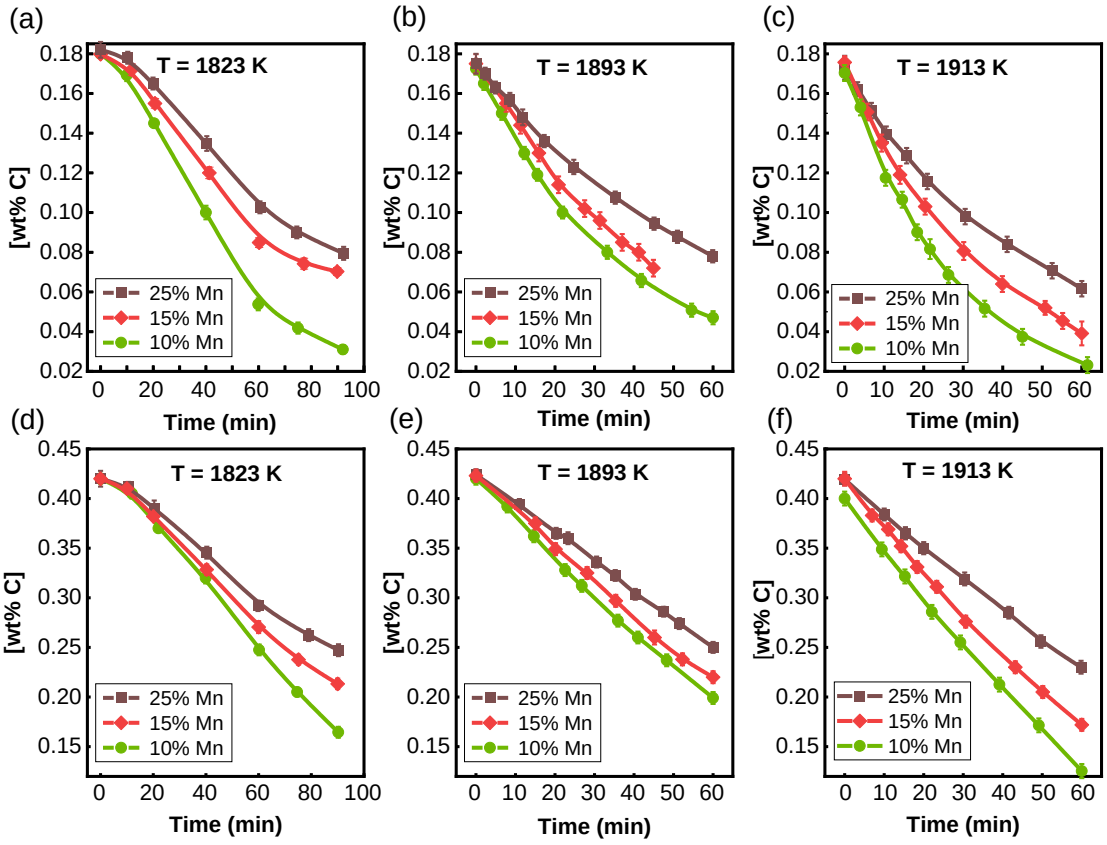

Figure 5.6. Effect of the initial Mn concentration on decarburization of Fe-0.18C alloys at a) 1823 K, b) 1893 K, c) 1913 K, and Fe-0.42C alloys at d) 1823 K, e) 1893 K, f) 1913 K, gas flow rate 300 Nml/min and gas composition: Ar-6.7% O_2, Submergence depth: 3cm.

Figure 5.7 (a-i) compares the effect of initial carbon concentration on manganese loss of alloys at each temperature. In all cases, the rate of manganese loss in stage 1 for Fe-0.18C alloy is higher than that of Fe-0.42C alloy. At 1823K, stage 3 starts at the same time for both carbon concentrations (Figure 5.7 (a), Figure 5.7 (d), Figure 5.7 (g)). In contrast, with increasing temperature to 1893 and 1913 K, stage 3 started earlier. Furthermore, for Fe-0.18C alloys duration of the middle stage was shorter and stage 3 started earlier than for Fe-0.42C alloys.

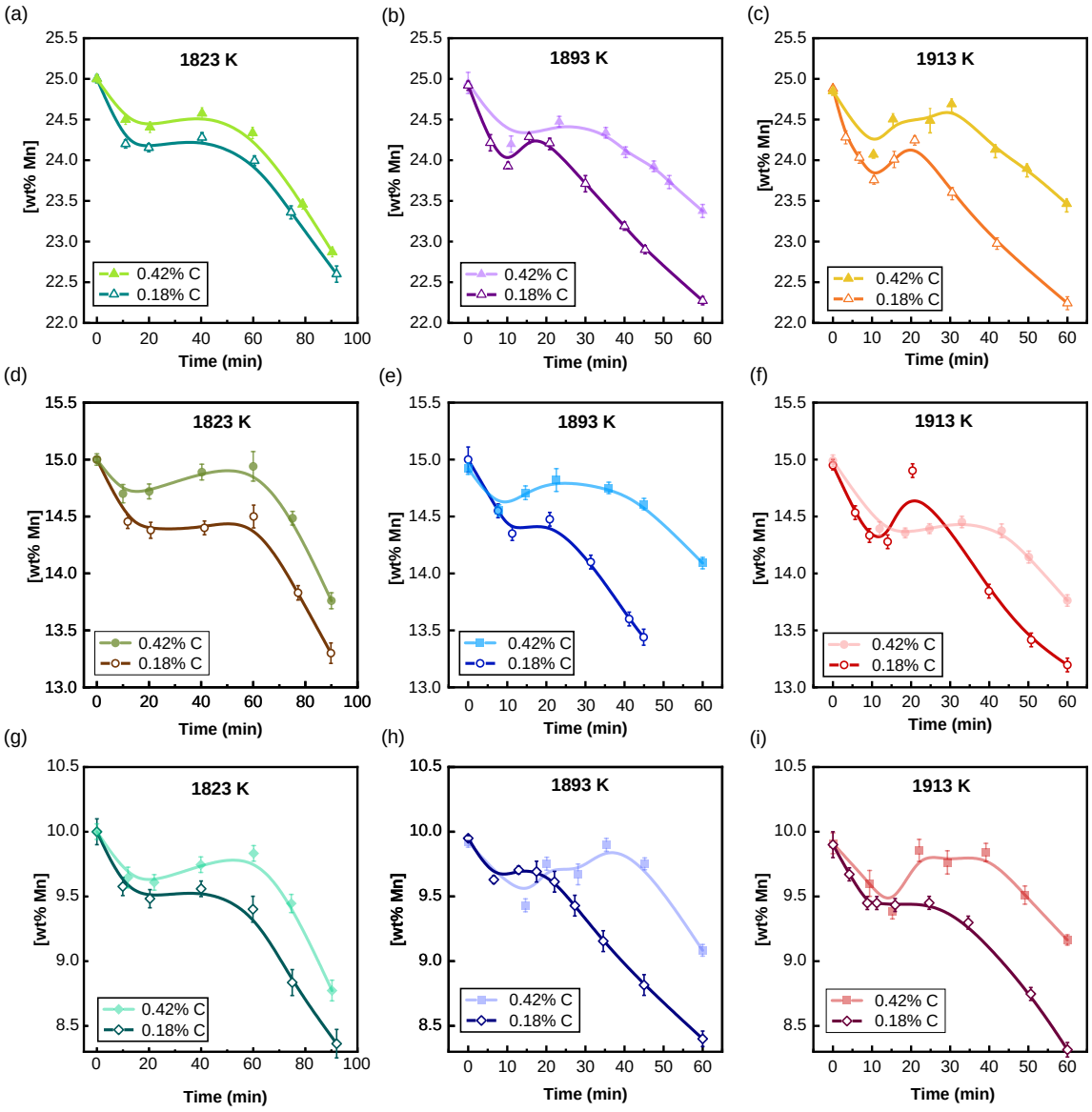

Figure 5.7. Effect of the initial carbon concentration on manganese loss of Fe-25Mn alloys at a) 1823 K, b) 1893 K, c) 1913 K, and Fe-15Mn alloys at d) 1823 K, e) 1893 K, f) 1913 K, and Fe-10Mn alloys at a) 1823 K, b) 1893 K, c) 1913 K, gas flow rate 300 Nml/min and gas composition: Ar-6.7% O_2, submergence depth: 3cm.

5.3.3 Effect of Submergence Depth

To investigate the effect of nozzle submergence depth on the rate of decarburization and demanganization, several experiments were carried out at depths of 1, 2, 2.5, and 3 cm for Fe-25Mn-0.18C and Fe-25Mn-0.42C alloys. These depths refer to the height of metal above the nozzle tip. The gas flow rate, gas composition, and temperature were maintained constant at respectively, 300 Nml/min, and Ar-6.7% O_2, and 1893 K. Figure 5.8 (a) and Figure 5.8 (b) show the change in carbon concentration in the metal with time for alloys with 0.18 and 0.42C. The corresponding manganese concentrations in the metal are given in Figure 5.9 (a), and Figure 5.9 (b). C and Mn concentrations were not influenced by the submergence depth. In a previous work by the authors [30], it was shown that the reaction times are of the order of 0.001 seconds which is about 1% of the residence time of bubble in the metal. Hence, before a bubble leaves the tip of the nozzle, reactions have occurred and completed so that change in the residence time of the bubble by increasing the depth of the nozzle will not affect the rate of reactions. The author's previous work also showed that although the overall reaction time was very short in comparison to the bubble residence time, the competition for oxygen between carbon and manganese was largely dictated by their predicted relative rates of mass transfer in the metal.

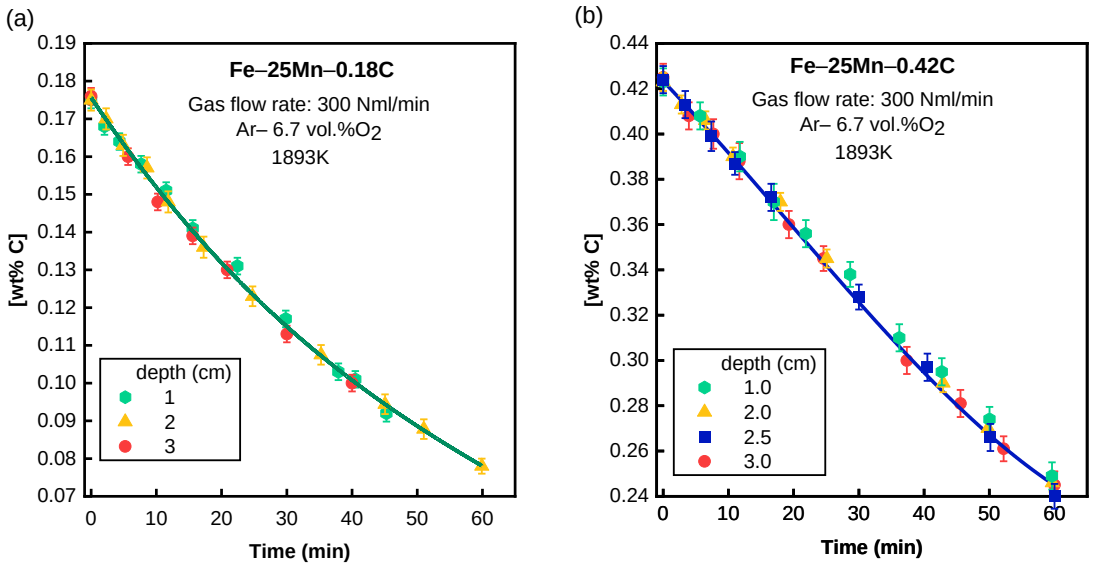

Figure 5.8. Carbon concentration in bath vs. time for a) Fe-25Mn-0.18C, b) Fe-25Mn-0.42C, variable: submergence depth.

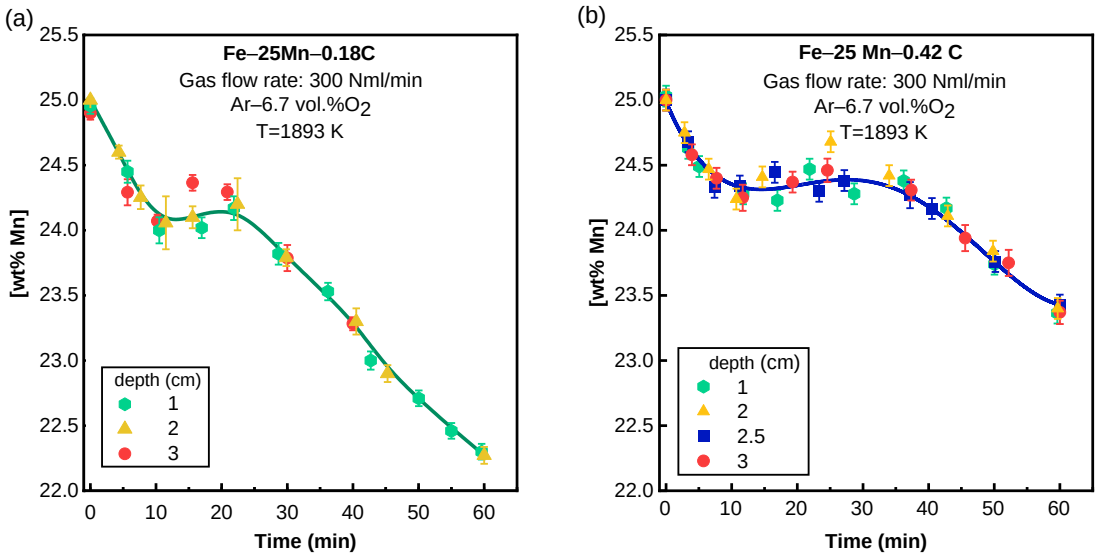

Figure 5.9. Manganese concentration in bath vs. time for a) Fe-25Mn-0.18C, b) Fe-25Mn-0.42C, variable: submergence depth.

5.3.4 Chemical Composition of Collected Fume

There was no fume on the crucible wall. However, the fume deposited on the furnace wall and cap was collected. It was not possible to collect all of it, but it was clear that the amount of fume generated increased with the initial manganese concentration of the alloy due to the increase in the vapor pressure of manganese. This observation is in agreement with the work of Chu *et al.* [31] on the processing of Fe-Mn-C steels containing 2 to 30%Mn and 0.004%C under vacuum. The concentration of Mn and Fe in fume was measured using ICP. According to X-ray diffraction, these elements were present primarily as MnO and Fe_2O_3. However, because the fine powder in the deposit oxidized as soon as the furnace was opened the authors are not able to determine in which form the fume deposited. For this reason, we have presented the composition of fume as the ratio of Mn/Fe. This ratio is plotted in Figure 5.10 (a) for various temperatures and alloy compositions. There was no appreciable difference between the composition of the fume at the wall and the cap of the furnace. For this reason, one composition for each experiment is plotted in this figure. As observed in Figure 5.10 (a), the Mn/Fe ratio of the fume increased with the initial manganese concentration of the alloy and decreasing temperature. Alloys with lower carbon contents (0.18% C) had higher ratios of Mn/Fe in fume. With increasing temperature, the fraction of Fe in the fume increased. The Mn/Fe ratio of the fume is consistent with the trend of the ratio of equilibrium pressures of Mn/Fe as shown in Figure 5.10 (b). However, from experimental data, Mn/Fe ratios are lower than predicted from the data in Figure 5.10 (b). For all except one alloy, the slope of the lines in Figure 10 (a) are

almost identical which would be consistent with a controlling role for mass transport of Mn in the metal. Furthermore, the rates increase with decreasing carbon concentration which would suggest competition for oxygen between manganese and carbon.

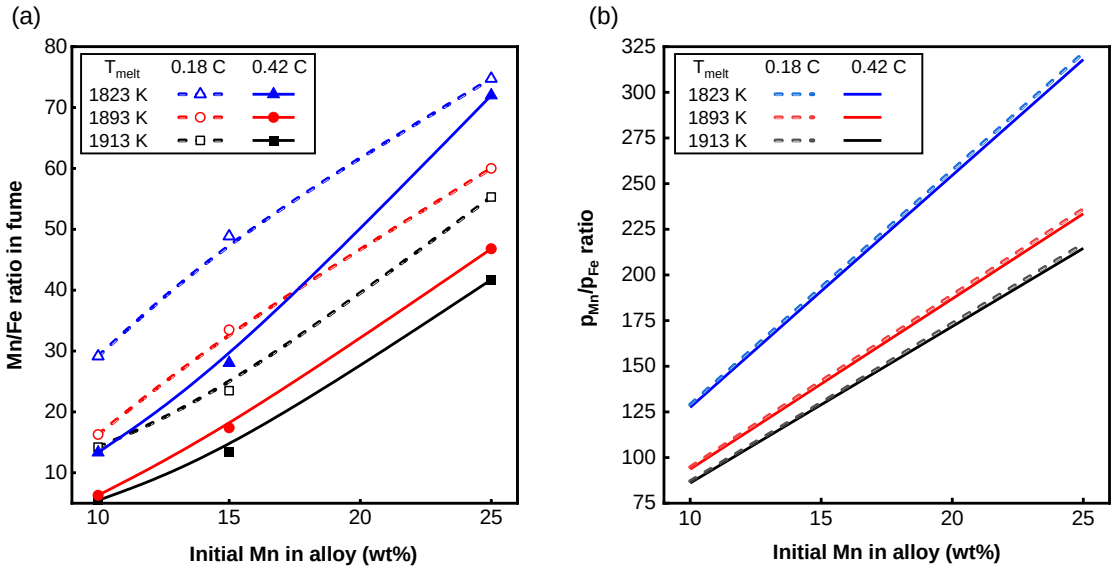

Figure 5.10. Chemical composition of fume collected after the experiments, submergence depth: 3cm, variable: temperature.

5.4 Discussion

5.4.1 Thermodynamic Analysis

Figure 5.11 (a-b) show the predicted equilibrium carbon and manganese concentration versus time for Fe-25Mn-0.42C alloy at temperatures of 1823 to 1913 K. To plot these graphs, the mass of steel, gas composition, and total flow rate used in the experiments were used as input in FactSage 8.0 using FactPS, FToxid, and FSstel databases in the Equilib module. It was assumed that for each case temperature remained constant at its initial value during the gas introduction. As was shown by similar calculations by the authors for alloy Fe-15Mn-1C [30], above a critical carbon content, the predicted rate of decarburization is

fast, and below the critical carbon content slows significantly (Figure 5.11 (a)). The calculations predict that regardless of temperature, rates of decarburization above the critical carbon content are 0.006%C/min because they will be entirely controlled by the supply of oxygen, whereas, below the critical carbon content rates decrease with temperature. Furthermore, above the critical carbon content, no loss of manganese is predicted. The experimental data do not agree with these predictions. For Fe-25Mn-0.42 C (Figure 5.5 (a)) the experimental rates of decarburization are 1.8 to 2.3 times slower than the FactSage prediction for temperatures of 1823 to 1913 K, and there was a simultaneous rapid manganese loss (Figure 5.3 (a)). It should be noted that the predicted fraction of iron in the fume, whether present as FeO or Fe is negligible and much less than that observed experimentally (Figure 5.10 (a)). It should also be noted that FeO is unstable relative to MnO and CO under the current experimental conditions.

Comparison of thermodynamic calculations with experimental observations shows that manganese and carbon in the bubble are not in equilibrium with the melt. This is consistent with observations from a previous publication by the authors [30] which showed that carbon and manganese oxidation occurred in proportion to the mass transfer rates of the species in the melt. Moreover, as indicated in Figure 5.8 and Figure 5.9, changing the depth of lance submergence did not make any difference in the decarburization and manganese loss, the reactions occur well within the time the bubble is present in the melt and that prolonged time after reaction does not lead to a repartitioning of the species. Therefore, it is clear that the bubble, having reacted, does not go through a transition towards true equilibrium.

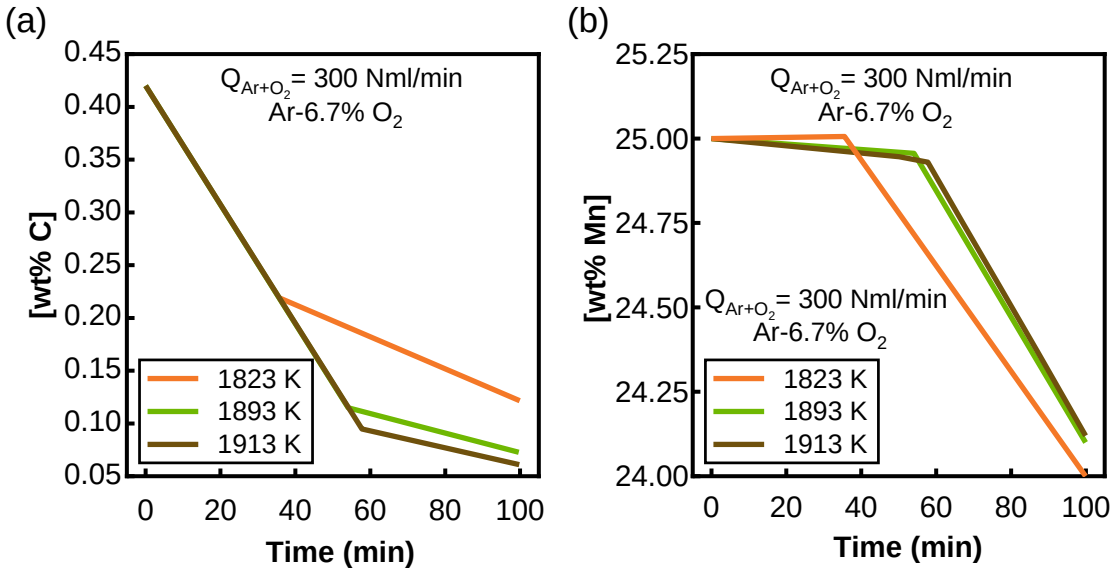

Figure 5.11. FactSage prediction for variation of a) carbon and b) manganese concentrations in the bath for Fe-25Mn-0.42C at various temperatures.

5.4.2 Rate of Mn Loss

Figure 5.12 shows the measured rates of manganese loss versus the initial manganese concentration of alloys. Increasing temperature resulted in the higher rates of Mn loss in both stages 1 and 3 for Fe-0.18C alloys (Figure 5.12 (a)). For stage 3, the effect of temperature on manganese loss was considerably smaller than for stage 1. Similarly, in Figure 5.12 (b), the increasing temperature is seen to have a bigger effect on stage 1. Furthermore, in all cases, alloys with higher initial manganese content exhibited higher rates of manganese loss, particularly in stage 1 of the process. Increasing temperature from 1823 to 1913 K led 20%, 37%, and 47% increase in the rate of manganese loss in stage 1 of the process for Fe-0.18C alloys. For Fe-42C alloys rate of manganese loss increased by 16%, 67%, and 65% for 10, 15, and 25%Mn alloys.

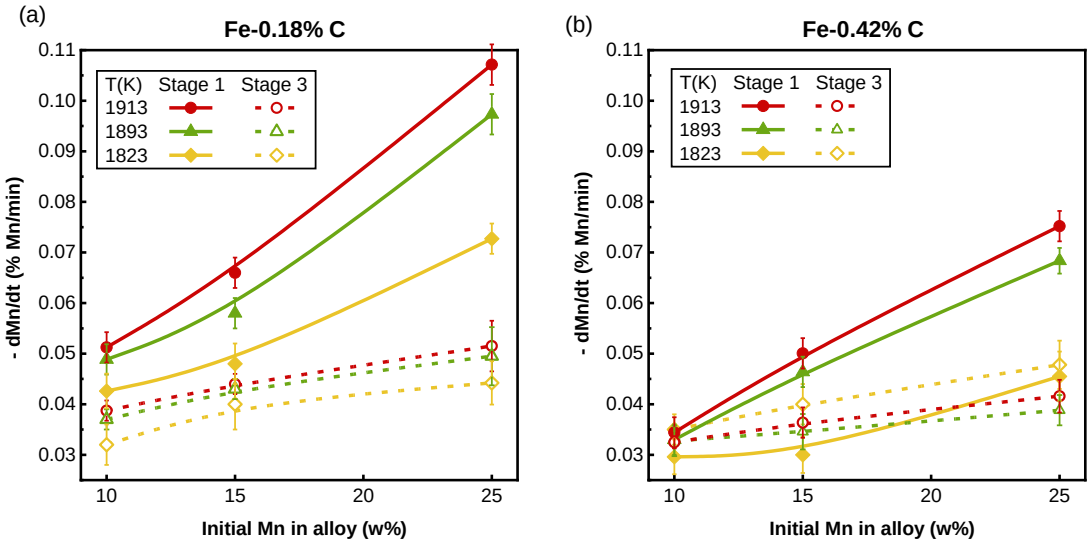

Figure 5.12. Rates of total manganese loss with the initial manganese concentration for a) Fe-0.18C, and b) Fe-0.42C alloys, Variable: temperature.

5.4.3 Oxygen Utilization

Assuming that the products of oxidation are CO and MnO, the fraction of oxygen consumed for the CO and MnO formation to the total supplied oxygen can be calculated. Table 5.1 shows the oxygen utilization, calculated on this basis, for decarburization for each alloy and temperature. For Fe-0.42C alloys at 1893 and 1913 K, the oxygen utilizations were very similar in all three stages. However, for Fe-0.18C alloys, oxygen utilization decreased with carbon content in the bath (from stage 1 to 3). For alloys at 1823 K, oxygen utilization was low in stage 1, higher in stage 2, and low in stage 3 again. The available oxygen after CO formation not sufficient to account for total manganese loss shown in Figure 5.12. Therefore, in addition to oxidation to MnO, there must be another mechanism involved in manganese loss. This observation agrees with studies by You *et al.* [21] and Lee *et al.* [26] for oxygen refining of high carbon ferromanganese. It was reported by these authors that the difference between the total manganese loss and oxidation was due to the evaporation of

manganese. In a previous publication by the current authors, where the experimental temperature was confined to 1823K, two possible mechanisms were assessed. In that work, it was found the straight-forward loss by evaporation could not explain all of the Mn loss. However, an additional mechanism, involving local heating of the bubble surface by the oxidation reactions to enhance manganese vaporization, followed by condensation of a fine mist of liquid manganese in the bubble, explained the additional loss over the loss by straight-forward evaporation. The additional mechanism is called the evaporation-condensation mechanism. In the following sections of this paper, the viability of these potential mechanisms extended the temperature range from 1823 to 1913K is discussed.

Table 5.1 Oxygen utilization for decarburization (%).

	1823 K			1893 K			1913 K		
Alloy	Stage 1	Stage 2	Stage 3	Stage 1	Stage 2	Stage 3	Stage 1	Stage 2	Stage 3
Fe-25Mn-0.42C	13	44	26	48	48	46	53	53	50
Fe-15Mn-0.42C	17	52	36	56	56	53	72	72	69
Fe-10Mn-0.42C	21	61	43	61	61	60	80	80	76
Fe-25Mn-0.18C	6	25	12	38	29	22	53	32	23
Fe-15Mn-0.18C	11	33	13	46	40	28	60	56	25
Fe-10Mn-0.18C	18	40	14	57	53	22	73	57	18

5.4.4 Potential Mechanisms for the Excess Manganese loss

5.4.4.1 Mn Loss as Mn (g) by Evaporation

If the difference between total manganese loss and loss as MnO is due to evaporative loss, the required vapor pressure of Mn (g) can be calculated readily, as detailed in Appendix 5.A. For evaporative loss to be a viable mechanism, the vapor pressure of Mn would have to be very high, which requires a substantial temperature rise of up to 557 K (Table 5.AI). The required temperature for the excess manganese loss to be due to evaporation as Mn (g) is plotted versus the initial Mn of alloys in Figure 5.13. In both Figure 5.13 (a), and Figure 5.13 (b), temperatures required to support evaporation as the source of excess manganese loss increased with increasing experimental temperature. For Fe-0.18C alloys, these required temperatures for stage 3 were considerably lower than for stage 1 (Figure 5.13 (a)). Liu *et al*. [28] observed similar excess manganese loss from Fe-16Mn-3C alloy by injection of pure O_2 at a flow rate of 500 ml/min into the melt. These workers did not present mass balance calculations, nor did they suggest a mechanism for Mn loss. However, these researchers have referred to the effect of CO_2 introduction in decreasing evaporation loss of Mn, most likely due to the endothermic nature of decarburization with CO_2. The mass of liquid steel was not given in their experiments, however, based on the crucible dimensions (inner diameter: 6 cm and height 12.5 cm, 20% of the crucible is filled) it is possible to make some estimate of the mass of steel to be at least 500 grams. With this assumption and knowing how much total Mn and C were removed based on their data, the vapor pressure of manganese required to support evaporative loss can be estimated to be

0.052 atm which would require a temperature rise of about 400 K. That temperature increase seems high. The current authors were not able to detect a temperature increase on the outer wall of the crucible and do not believe it is conceivable that a 400 K temperature increase in the melt would not be detected on the crucible wall, however, it might be possible to have very high local temperature increases in the vicinity of the bubble.

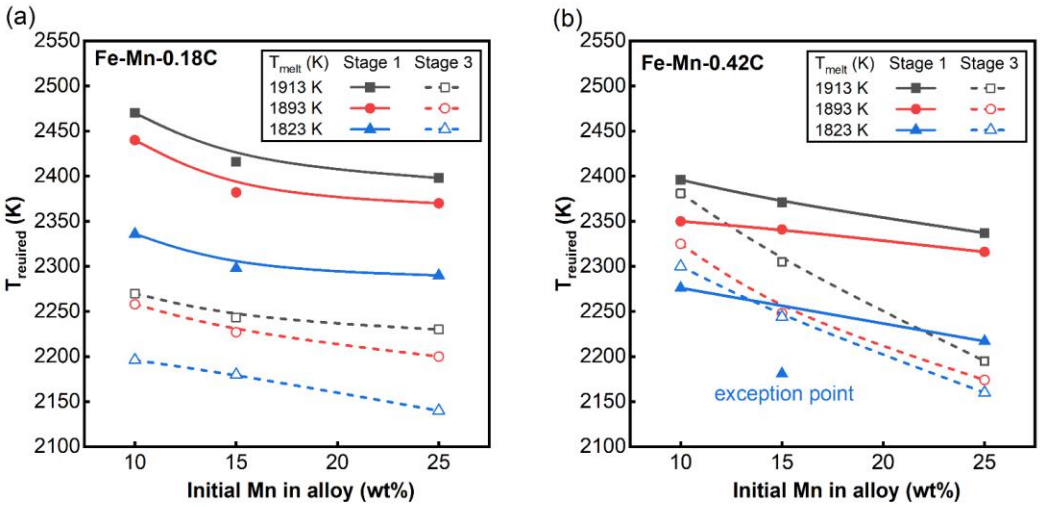

Figure 5.13. The required temperature for the excess manganese loss being as a vapor for Fe-Mn-0.18C alloys, and b) Fe-Mn-0.42C alloys, variable: temperature.

5.4.4.2 Mn Loss as Droplet inside Bubble by Evaporation-Condensation

Given the difficulty in justifying the necessary temperature rise for evaporative loss, the authors previously proposed a mechanism based on evaporation-condensation [29]. The proposed mechanism assumes that in addition to loss as oxide and vapor, manganese may form a mist of liquid droplets inside the bubble as follows: the temperature of the bubble surface is increased by exothermic reactions (MnO and CO formation) the local

temperature rise leads to Mn evaporation at a high vapor pressure. The manganese vapor then condenses as fine droplets inside the bubble. This mechanism is viable under conditions where Mn vapor generated is in equilibrium with Mn in the alloy and condenses at a lower temperature inside the bubble. This mechanism can work only if the temperature difference is enough for the Mn vapor pressure in equilibrium with the bubble surface p_{Mn}^{S} is higher than that in equilibrium with pure Mn (l) in the bubble interior p_{Mn}^{mist}. Mn condensation will continue as long as the temperature gradient between the bubble surface and its interior remains sufficiently high. This mechanism is equivalent to the concept of fume formation proposed by Turkdogan *et al*. [27] except in the current case, the metal condenses as a mist of liquid droplets rather than as oxide particles observed by Turkdogan *et al*. [27]. The detailed calculation procedure for the evaporation-condensation mechanism is given in Appendix 5.B. The vapor pressures and temperatures of Mn at the bubble surface for each alloy at various experimental conditions are provided in Table 5.2. As indicated, the temperature at the surface of the bubble (T_S) required for the proposed evaporation-condensation mechanism increased with the starting temperature. For a given Mn concentration T_S is independent of carbon concentration and it is higher for alloys with lower manganese content.

It is mentioned earlier that the exothermic oxidation reactions generate the required heat for this mechanism to work. Here, the viability of this mechanism is explored from a heat balance point of view. Given the short time over which the manganese loss to the bubble occurs, it is assumed that there is no heat loss, and because the gas enters the melt through

a heated ceramic tube, all the supplied oxygen is consumed to produce CO and MnO at the starting temperature. The generated heat from the oxidation reaction must be sufficient to heat the layer of metal surrounding the bubble to the required higher temperatures T_S. The thickness of this layer can be calculated to determine the number of moles of steel and Mn in that layer. The details of these calculations are provided in Appendix 5B. Table 5.2 shows the thickness of the heated layer for each stage as well as the number of moles of Mn contained in that layer which is compared with the total number of moles of Mn removed per bubble for various alloys and temperatures. In most cases, the amount of manganese in the heated layer is more than sufficient to support the manganese loss and for the cases where this is not true, the amount is close. This would suggest that the mechanism is viable given the fact that manganese can transport into the heated layer and it is only the manganese at the surface that needs to be at the evaporation temperature. It should be noted that all these experiments were done in the same way. However, these inconsistencies may arise for several reasons. As mentioned earlier reactions are sufficiently fast that the reaction is over shortly after the bubble enters the melt. The tip of the alumina nozzle could be a bit eroded and the bubble could be different in some cases. Furthermore, there might be some buildup on the nozzle. These possibilities make it difficult to interpret the results definitively. The authors attempted to measure the temperature rise for a small number of experiments, but no measurable temperature rise was detected using a thermocouple in contact with the outside of the crucible. However, it does not exclude the possibility of a

localized temperature rise at the surface of the bubble, in fact badly eroded nozzle tips are strong evidence for such temperature rise.

Table 5.2. Calculation of Mn in the heated layer.

T_{melt} (K)	Alloy (wt%)	T_S(K)	p^s_{Mn}(atm)	Stage 1			Stage 3		
				Thickness of heated layer (μm)	Mn in heated layer ($\times 10^6$mol)	Total Mn loss per bubble (mol$\times 10^6$)	Thickness of heated layer (μm)	Mn in heated layer (mol$\times 10^6$)	Total Mn loss per bubble (mol$\times 10^6$)
1823	10-0.42	2185	0.042	0.27	2.3	1.6	0.18	1.5	1.8
	15-0.42	2110	0.041	0.36	4.6	1.7	0.26	3.4	2.0
	25-0.42	2023	0.039	0.55	12	2.5	0.48	10	2.5
	10-0.18	2185	0.043	0.34	2.9	2.4	0.33	2.8	1.7
	15-0.18	2110	0.041	0.43	5.6	2.6	0.42	5.4	2.1
	25-0.18	2023	0.039	0.73	16	4.0	0.69	15	2.3
1893	10-0.42	2296	0.076	0.15	1.3	1.8	0.16	1.4	1.7
	15-0.42	2211	0.073	0.21	2.8	2.5	0.22	2.9	1.8
	25-0.42	2115	0.07	0.35	7.7	3.7	0.37	8.0	2.0
	10-0.18	2293	0.075	0.16	1.4	2.6	0.30	2.6	1.9
	15-0.18	2208	0.073	0.26	3.4	3.1	0.35	4.5	2.2
	25-0.18	2112	0.069	0.43	9.2	5.0	0.55	12	2.5
1913	10-0.42	2326	0.088	0.09	0.8	1.8	0.10	0.9	1.7
	15-0.42	2239	0.085	0.12	1.6	2.7	0.10	1.4	1.9
	25-0.42	2141	0.081	0.31	6.8	4.0	0.33	7.2	2.1
	10-0.18	2325	0.088	0.08	0.7	2.8	0.31	2.6	1.5
	15-0.18	2237	0.085	0.03	0.3	3.5	0.29	3.8	2.1
	25-0.18	2139	0.081	0.31	7.0	5.7	0.40	8.7	2.6

Figure 5.14 shows the temperature at the surface of the bubble required for the evaporation-condensation mechanism to operate. In this mechanism, the temperature requirement only depends on the manganese concentration of alloy and temperature of the melt. Comparing with Figure 5.13, temperatures for this mechanism are lower between 55 to 270 K in stage 1, and between 28-170 K in stage 3. Alloy Fe-10Mn -0.18C at 1913 K was an exception where the required temperature for the simple evaporation mechanism was about 50 K lower than the evaporation-condensation mechanism. On balance it seems more likely that evaporation condensation operates driven by a local temperature increase at the bubble/metal interface. It is also worth noting that the mechanisms of evaporation-condensation and simple evaporation are not mutually exclusive, and it is likely that both operated in parallel.

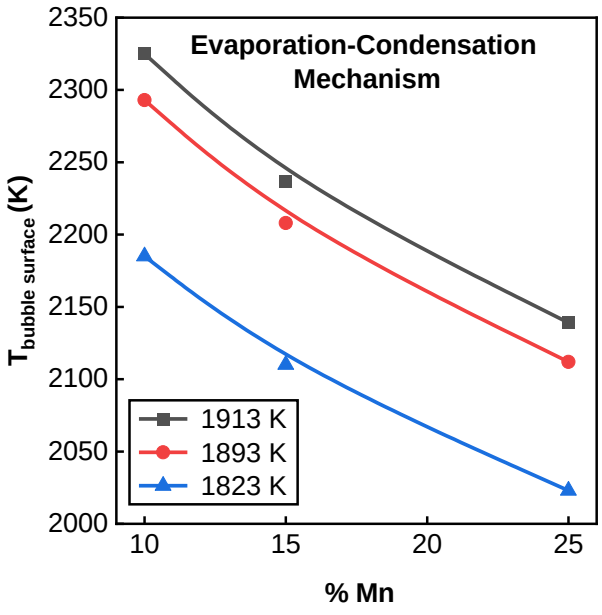

Figure 5.14. The temperature at the surface of the bubble versus Mn concentration of alloy.

The contribution of each mechanism of Mn loss is shown in Figure 5.15 and Figure 5.16 for Fe-0.18C and Fe-0.42C alloys, respectively. Mn losses are as oxide, vapor, and mist droplets inside the bubble. These different contributions were calculated by assuming all oxygen remaining after the carbon loss was accounted for, reacted with manganese, any additional losses of manganese were first attributed to evaporation and then evaporation-condensation. Based on the much greater stability of MnO and CO, it is further assumed that amount of FeO compared with MnO is negligible. As shown in Figure 5.15 (a-i), the total rate of manganese loss for alloy Fe-25Mn-0.18C and Fe-15Mn-0.18C, Fe-10Mn-0.18C in both stages 1 and 3 increases with temperature. In both stages, the contribution of oxidation loss of manganese decreased with temperature, while its loss as vapor increased. In Figure 5.15 (c), loss as oxide, vapor, and mist overlapped in stage 3. The contribution of manganese loss as liquid droplets followed the same trend as vapor, it increased with temperature. However, for alloy Fe-10Mn-0.18C in stage 3, the contribution of loss as droplets was zero (Figure 5.15 (g-i)). Although according to heat balance calculations there is more than enough Mn in the heated layer as shown in Table 5.2, the total Mn loss in stage 3 was not that high to reach that high vapor pressure the Mn vapor inside the bubble in equilibrium with mist must be at the activity of 1. Therefore, the contribution of Mn mist is zero in stage 3. Likewise, in Figure 5.16 (a-i), manganese loss as oxide decreased with temperature whereas loss as vapor increased in all alloys at both stages 1 and 3 for Fe-25Mn-0.42C alloys. The contribution of manganese loss as droplet increased with temperature in stage 1 for all alloys, however, in stage 3 it remained constant (Figure 5.16

(d) and Figure 5.16 (f)) or decreased slightly with temperature (Figure 5.16 (a) compared with Figure 5.16 (b) and (Figure 5.16 (c)).

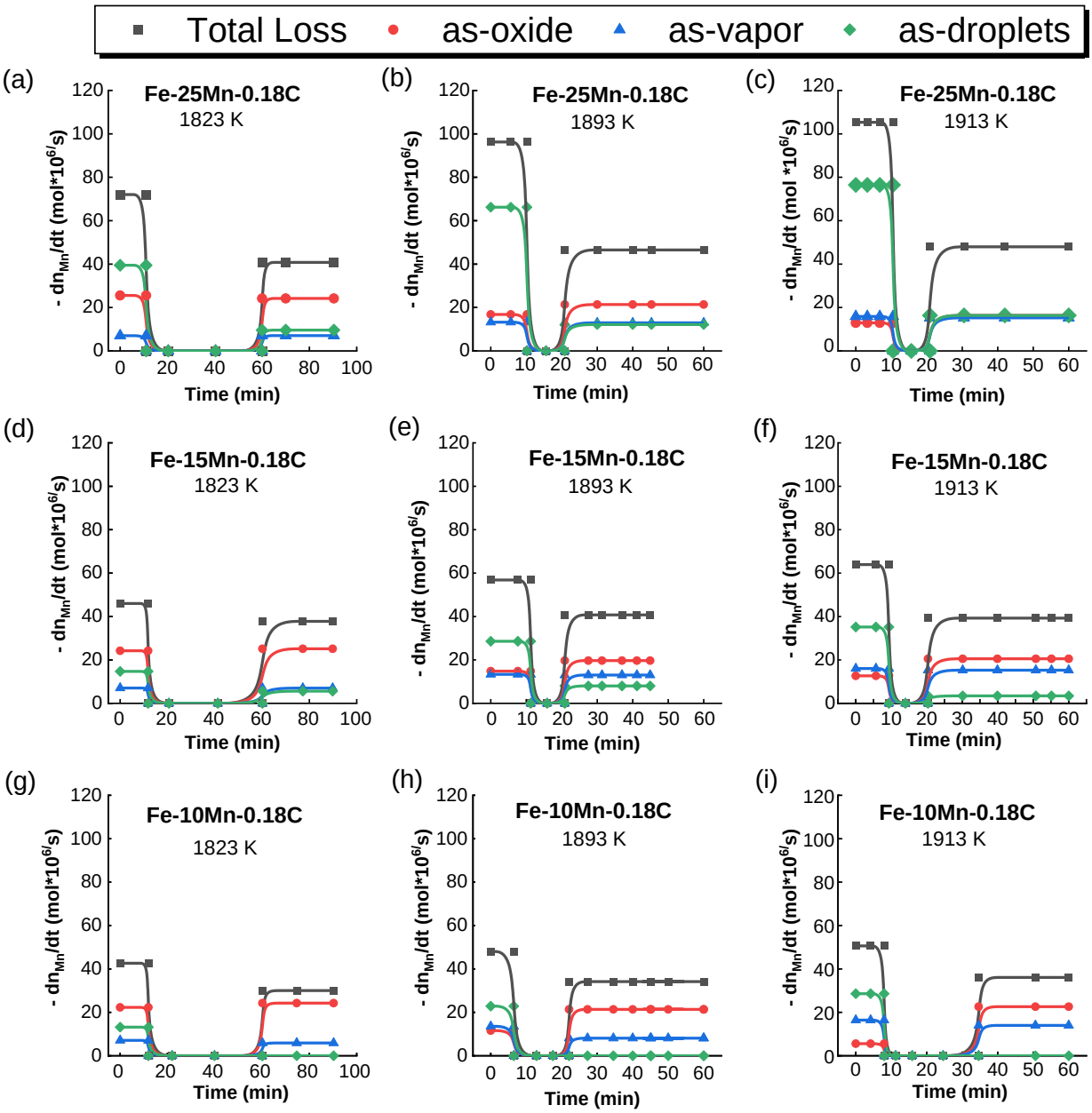

Figure 5.15 Rates of Mn losses as vapor, oxide, and liquid droplet inside the bubble for Fe-25Mn-0.18C at a)1823 K, b)1893 K, c)1913 K, for Fe-15Mn-0.18C at d)1823 K, e)1893 K, f)1913 K, and for Fe-10Mn-0.18C at g)1823 K, h)1893 K, i)1913 K.

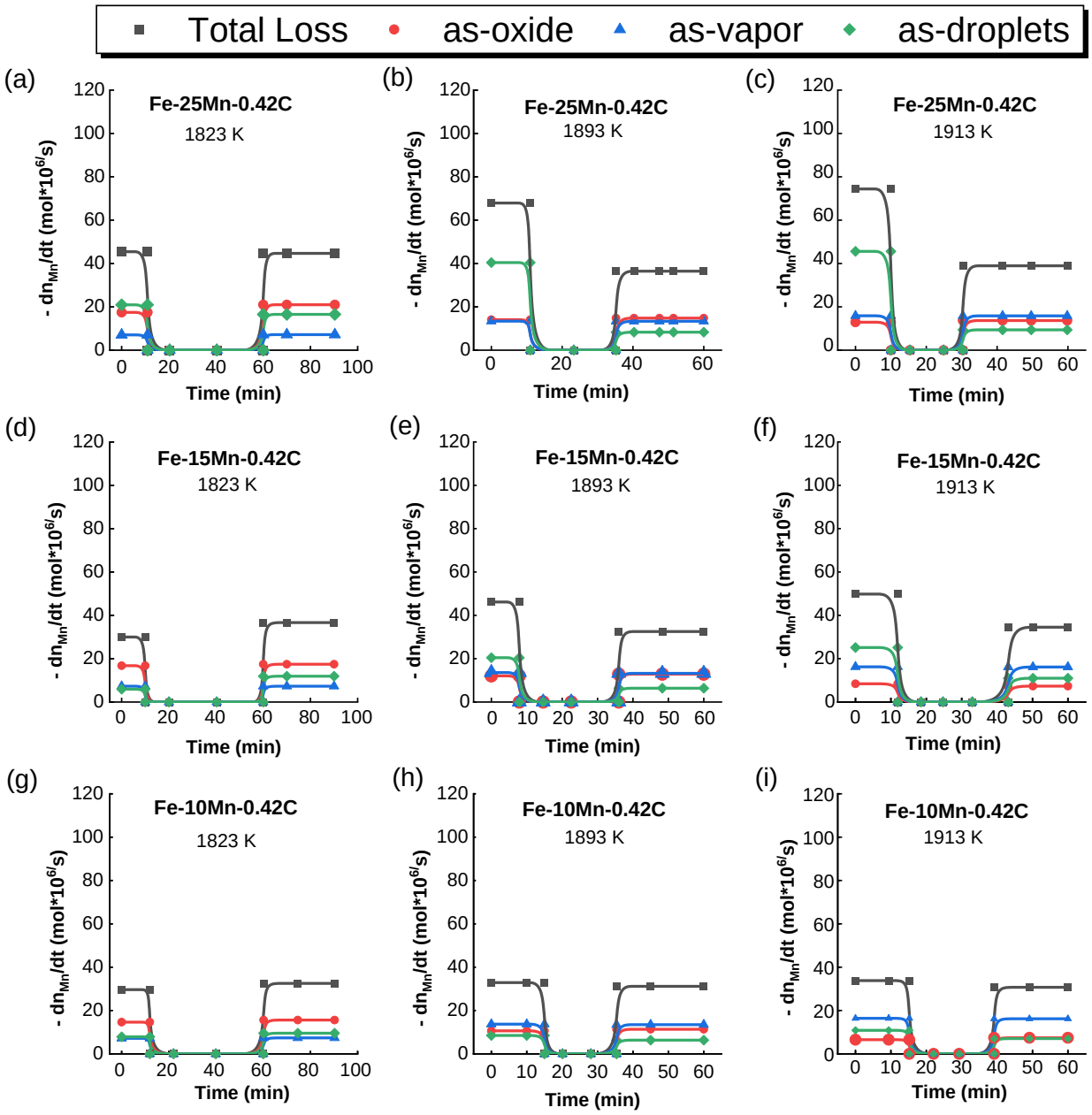

Figure 5.16. Rates of Mn losses as vapor, oxide, and liquid droplet inside the bubble for Fe-25Mn-0.42C at a)1823 K, b)1893 K, c)1913 K, for Fe-15Mn-0.42C at d)1823 K, e)1893 K, f)1913 K, and for Fe-10Mn-0.42C at g)1823 K, h)1893 K, i)1913 K.

5.5 Conclusions

In this paper, the decarburization and manganese losses from Fe-Mn-C alloys with different manganese and carbon concentrations in the temperature range of 1823 to 1913K were studied.

1. The decarburization and total manganese loss increased with increasing temperature. The rate of decarburization increased because more oxygen was partitioned to carbon oxidation than to manganese. The increase in manganese loss at higher temperatures is because of the large increase in vapor pressure leading to more loss as mist and by simple vaporization.
2. Based on the observation that changing the depth of lance submergence did not make any difference in the decarburization and manganese loss, the reactions occur well within the time the bubble is present in the melt and that prolonged time after reaction does not lead to a repartitioning of the species.
3. Comparison of thermodynamic calculations with experimental observations shows that manganese and carbon in the bubble are not in equilibrium with the melt. This is consistent with observations from a previous publication by the authors which showed that carbon and manganese oxidation occurred in proportion to the mass transfer rates of the species in the melt. When these observations are taken in combination with conclusion 2 it is also clear the bubble, having reacted, does not go through a transition towards true equilibrium.

4. Manganese loss can be explained by considering multiple mechanisms in parallel; oxide formation and vapor formation, and evaporation-condensation.

5.6 Acknowledgements

The authors acknowledge financial support from the Natural Sciences and Engineering Research Council of Canada. Additional thanks go to ArcelorMittal Dofasco, Stelco, Praxair, and Hatch Ltd. for in-kind support and technical expertise.

5.7 Appendix 5A

DETAILED CALCULATIONS OF MANGANESE VAPOR PRESSURE IN SECTION 5.4.4.1:

Each gas bubble is composed of CO, Ar, and Mn (g), and the total pressure inside each bubble, P_t, is approximately 1 atm. Hence, the vapor pressure of manganese can be calculated from Equation 5A.1 with a known amount of CO and MnO removed per bubble during each stage.

$$p_{Mn} = \frac{n_{Mn}}{n_{CO}+n_{Mn(g)}+n_{Ar}} P_t \qquad (5A.1)$$

The number of moles of each species removed by end of stages 1 and 3, the partial pressure of CO and Mn are listed in Table 5A.I and Table 5A.II. In these experiments, the total gas flow rate and gas composition were 300 Nml/min and Ar-6.7%O_2. The calculated bubble diameter according to the work of Irons *et al.* [32] was 1.48 cm at 1823 K and 1.49 cm at 1893 and 1913 K. The frequency of bubble formation was 18, 18.30, and 18.38 s^{-1} at 1823,

1893, and 1913 K, respectively. For this reason, the number of moles of argon was slightly different depending on the bubble size. The required temperature to achieve these manganese vapor pressures are calculated from Equation 5A.2 where a_{Mn} is the activity of manganese in the melt, and Tm is the melt temperature.

$$p_{Mn} = a_{Mn}.\exp\left(\frac{-33440}{T_m} - 3.02\ln T_m + 37.67\right) \qquad (5A.2)$$

It should be noted that the ΔT values are tabulated in Table 5A.I and Table 5A.II are the difference between the required temperature and the initial temperature of the melt. As indicated, the required temperature for evaporation decreases with increasing manganese concentration in the alloy. This is because of the vapor pressure and activity of manganese increase with its content in the melt.

Table 5A. I Calculation of manganese vapor pressure for Stage 1 with the assumption that excess Mn loss is caused by evaporation.

T(K)	Alloy (wt%)	Number of moles of species per bubble× 10^6					p_{CO}	$p_{Mn,excess}$	$T_{Required}$ (K)	ΔT (K)
		$n_{Mn,\ tot}$	n_{MnO}	$n_{Mn,\ exss}$	n_{CO}	n_{Ar}				
1823	10-0.42	1.6	0.8	0.8	0.7	11	0.06	0.07	2174	351
	15-0.42	1.7	0.9	0.7	0.6	11	0.05	0.06	2181	358
	25-0.42	2.5	1.0	1.6	0.2	11	0.02	0.13	2217	394
	10-0.18	2.4	1.2	1.1	0.3	11	0.02	0.09	2336	513
	15-0.18	2.6	1.3	1.2	0.2	11	0.01	0.10	2298	475
	25-0.18	4.0	1.4	2.6	0.1	11	0.01	0.19	2290	467
1893	10-0.42	1.8	0.6	1.2	0.9	10	0.07	0.10	2347	454
	15-0.42	2.5	0.7	1.9	0.8	10	0.06	0.14	2341	448
	25-0.42	3.7	0.8	2.9	0.7	10	0.05	0.21	2316	423
	10-0.18	2.6	0.6	2.0	0.8	10	0.06	0.15	2440	547
	15-0.18	3.0	0.8	2.0	0.7	10	0.05	0.17	2378	485
	25-0.18	5.3	0.9	4.3	0.6	10	0.04	0.28	2378	485
1913	10-0.42	1.8	0.36	1.5	1.2	10	0.09	0.11	2381	468
	15-0.42	2.7	0.4	2.2	1.0	10	0.08	0.17	2371	458
	25-0.42	4.0	0.7	3.3	0.8	10	0.05	0.23	2337	424
	10-0.18	2.8	0.3	2.5	1.1	10	0.08	0.18	2470	557
	15-0.18	3.5	0.7	2.8	0.9	10	0.06	0.20	2411	498
	25-0.18	5.7	0.7	5.0	0.8	10	0.05	0.31	2398	485

Table 5A. II Calculation of manganese vapor pressure for Stage 3 with the assumption that excess Mn loss is caused by evaporation.

T(K)	Alloy (wt%)	Number of moles of species per bubble × 10^6					p_{CO}	$p_{Mn,excess}$	$T_{Required}$ (K)	ΔT (K)
		$n_{Mn,\ tot}$	n_{MnO}	$n_{Mn,\ exss}$	n_{CO}	n_{Ar}				
1823	10-0.42	2.0	0.9	0.9	0.6	10	0.05	0.08	2300	477
	15-0.42	2.0	1.0	1.1	0.5	11	0.04	0.09	2244	421
	25-0.42	2.5	1.2	1.3	0.4	11	0.03	0.11	2191	368
	10-0.18	1.7	1.3	0.3	0.2	11	0.02	0.03	2128	305
	15-0.18	2.1	1.4	0.7	0.1	11	0.01	0.06	2182	359
	25-0.18	2.3	1.3	0.9	0.2	11	0.02	0.08	2140	317
1893	10-0.42	1.7	0.6	1.1	0.9	10	0.07	0.09	2325	432
	15-0.42	1.8	0.7	1.1	0.8	10	0.05	0.07	2248	355
	25-0.42	2.1	0.7	1.4	0.7	10	0.06	0.11	2195	282
	10-0.18	1.9	1.2	0.7	0.3	10	0.03	0.06	2258	365
	15-0.18	2.2	1.1	1.1	0.4	10	0.04	0.10	2227	334
	25-0.18	2.5	1.2	1.3	0.3	10	0.03	0.11	2200	307
1913	10-0.42	1.7	0.4	1.3	1.0	10	0.08	0.10	2354	441
	15-0.42	1.9	0.4	1.5	1.0	10	0.07	0.12	2305	392
	25-0.42	2.1	0.7	1.4	0.7	10	0.06	0.11	2195	282
	10-0.18	2.0	1.2	0.7	0.3	10	0.02	0.06	2270	357
	15-0.18	2.0	1.0	1.0	0.4	10	0.03	0.09	2241	328
	25-0.18	2.6	0.9	1.7	0.3	10	0.03	0.14	2238	325

5.8 Appendix 5B

DETAILED CALCULATIONS OF MANGANESE IN THE HEATED LAYER IN SECTION 5.4.4.2

To determine the flux of Mn in the gas phase by the proposed evaporation-condensation mechanism, Equation 5A.3 can be used where; k_{Mn} is the mass transfer coefficient of Mn in unit of cm/s. R is the gas constant in the unit of $\frac{cm^3 atm}{K.mol}$. T_b and T_s are the temperatures inside the bubble and at its surface, in units of K. The surface area of bubble A is 6.9cm^2 at 1823 K and 7 cm^2 at 1883 and 1913 K. $\frac{dMn_{evap}}{dt}$ is the rate of evaporation of Mn in unit of $\frac{mol}{s}$.

$$\frac{k_{Mn}}{R}\left(\frac{p_{Mn}^{mist}}{T_b}-\frac{p_{Mn}^{s}}{T_s}\right)=-\frac{dMn_{evap}}{A.dt} \qquad (5A.3)$$

The requirement for this mechanism to operate is that $\frac{p_{Mn}^{s}}{T_s}$ being higher than $\frac{p_{Mn}^{mist}}{T_b}$. The activity of Mn in the mist inside the bubble a_{Mn}^{mist} is equal to 1 and a_{Mn}^{s} is the activity of Mn in equilibrium with the liquid. Therefore, the temperature at the surface of bubble Ts can be calculated from Equation 5A.5.

$$p_{Mn}^{mist}=a_{Mn}^{mist}p_{Mn\,at\,T_b}^{0}=a_{Mn}^{mist}\exp\left(\frac{-33440}{T_b}-3.02\ln T_b+37.67\right) \qquad (5A.4)$$

$$p_{Mn}^{s}=a_{Mn}^{s}p_{Mn\,at\,T_s}^{0}=a_{Mn}^{s}\exp\left(\frac{-33440}{T_s}-3.02\ln T_s+37.67\right) \qquad (5A.5)$$

As mentioned earlier, in these experiments the reactions take place very quickly, and the actual manganese evaporation rate is unknown. For the purpose of these calculations, the authors have chosen to use the minimum value possible by assuming the reaction occurs over the total residence of the bubble (0.11 sec). For instance, for Fe-15Mn-0.42C at 1893 K, $\frac{\mathrm{dMn_{evap}}}{\mathrm{A.dt}}$ is equal to 9.6×10^{-7}mol/cm^2.s. The temperature at the surface of the bubble (Ts) is 2211 K. k_{Mn} is calculated to be 262 cm/s. Because of the assumptions behind the calculations, this value is conservative. But is consistent with the values quoted in the literature based on similar assumptions [26].

In the case of Fe-15Mn-0.42C alloy at 1893 K in stage 1, 0.27J heat is generated from MnO and CO formation. The temperature at the surface of the bubble (Ts) is 2211 K, constant pressure molar heat capacity (Cp) of liquid steel is 46 J/mol.K. Hence, 0.27J can heat 1.8×10^{-5} mole steel (1.5×10^{-4} cm^3) from 1893 to 2211 K. As the activity of Mn in this alloy is 0.15, the heated layer contains 2.8×10^{-6} moles of Mn. In stage 1 of this experiment, total Mn loss is 2.5×10^{-6} moles. Therefore, there is sufficient Mn in the heated layer to account for the excess Mn loss by the evaporation-condensation mechanism. The ratio of the volume of metal in that layer (1.5×10^{-4}) to the surface area of the bubble (7 cm^2) gives the thickness of the heated layer which is 0.21 μm.

5.9 References

1 B.C. De Cooman, O. Kwon, and K.G. Chin: *Mater. Sci. Technol.*, 2012, vol. 28, pp. 513–27.

2 O. Bouaziz, H. Zurob, B. Chehab, J.D. Embury, S. Allain, and M. Huang: *Mater. Sci. Technol.*, 2011, vol. 27, pp. 707–9.

3 L. Chen, Y. Zhao, and X. Qin: *ACTA Metall. Sin.*, 2013, vol. 26, pp. 1–15.

4 K. Chin, W. Cho, S. Kim, Y. Kim, T. Song, and T. Kim: in *The METEC and 2nd European Steel Technology and Application Days (ESTAD) conference*, Düsseldorf, 2015, pp. 65–8.

5 R. Elliott, K. Coley, S. Mostaghel, and M. Barati: *JOM*, 2018, vol. 70, pp. 691–9.

6 O. Bouaziz, S. Allain, C.P. Scott, P. Cugy, and D. Barbier: *Curr. Opin. Solid State Mater. Sci.*, 2011, vol. 15, pp. 141–68.

7 O. Grässel, L. Krüger, G. Frommeyer, and L.W. Meyer: *Int. J. Plast.*, 2000, vol. 16, pp. 1391–409.

8 R. Elliott, K. Coley, S. Mostaghel, and M. Barati: *JOM*, 2018, vol. 70, pp. 680–90.

9 L. Mujica, S. Weber, G. Hunold, and W. Theisen: *Steel Res. Int.*, 2011, vol. 82, pp. 26–31.

10 T. Furukawa, H. Huang, and O. Matsumura: *Mater. Sci. Technol. (United Kingdom)*, 1994, vol. 10, pp. 964–70.

11 D.S. Kozak and L.R. Matricardi.: *Iron Steelmak.*, 1981, vol. 8, pp. 28–31.

12 S.E. Olsen, M. Tangstad, and T. Lindstad: *Production of Manganese Ferroalloys*, 2017, pp 9.

13 M.M. Gasik: *Handbook of Ferroalloys. Theory and Technology*, Butterworth Heinemann, 2013, pp 257.

14 C.F. Redeker, H.-J. Renner, and J. Schöttler: *Cost Efficient Metallurgy for the Production of Novel Ultra-High Strength Deep Drawable Steel Gades with High Mn Contents from 10 to 25 Wt.-%*, Luxembourg:, 2008.

15 R.J. Fruehan: *Ironmak. Steelmak.*, 1976, vol. 3, pp. 153–8.

16 T. Ohno and T. Nishida: *Tetsu-to-Hagane*, 1977, vol. 63, pp. 2094–9.

17 J. Reichel and J. Szekely: *Iron Steelmak.*, 1995, vol. 22, pp. 41–8.

18 J. Wei and D. Zhu: *Metall. Mater. Trans. B*, 2002, vol. 33, pp. 111–9.

19 J.H. Wei: *J. Shanghai Univ.*, 2002, vol. 6, pp. 1–23.

20 V.-V. Visuri, M. Järvinen, A. Kärnä, P. Sulasalmi, E.-P. Heikkinen, P. Kupari, and T. Fabritius: *Metall. Mater. Trans. B*, 2017, vol. 48, pp. 1850–67.

21 B.-D. You, B.-W. Lee, and J.-J. Pak: *Met. Mater.*, 1999, vol. 5, pp. 497–502.

22 B. You, J. Han, and J. Pak: *Steel Res.*, 2000, vol. 71, pp. 22–6.

23 B.-D. You: *J. Korean Institue Met. Mater.*, 1995, vol. 33, pp. 1508–13.

24 B.-D. You, K.-Y. Park, J.-J. Pak, and J.-W. Han: *Met. Mater.*, 1999, vol. 5, pp. 395–9.

25 K. Yamamoto, T. Mimura, S. Ito, and T. Onoye: *Tetsu-to-Hagane*, 1986, vol. 72,

pp. 1034–46.

26 Y.E. Lee and L. Kolbeinsen: *ISIJ Int.*, 2005, vol. 45, pp. 1282–90.

27 E.T. Turkdogan, P. Grieveson, and L.S. Darken: *J. Am. Chem. Soc.*, 1963, vol. 67, pp. 1647–54.

28 H. Liu, J. Liu, J. Schenk, F.M. Penz, L. Sun, R. Zhang, and Z. An: *Metall. Mater. Trans. B*, 2020, vol. 51, pp. 756–62.

29 A. Rafiei, G.A. Irons, and K.S. Coley: *Steel Reseach Int.*, DOI:10.1002/srin.202000480.

30 A. Rafiei, G.A. Irons, and K.S. Coley: *Metall. Trans. B*, Under Review.

31 J. Chu, Y. Bao, X. Li, F. Gao, and M. Wang: *Steel Res. Int.*, 2020, vol. 2000333, pp. 1–9.

32 G.A. Irons and R.I.L. Guthrie: *Metall. Trans. B*, 1978, vol. 9, pp. 101–10.

Chapter 6

6 General Discussion and Conclusions

This chapter presents a summary of findings from the previous chapters in this thesis, highlighting any conclusions from each of the chapters, followed by any general statements that can be made about the work as a whole, the general conclusion that can be drawn, and any gaps in understanding leading to recommendations for future work.

Chapters 1 and 2 present background material in AOD refining of stainless steel and high carbon ferromanganese alloys. Comparing the behavior of Fe-Cr-C and Fe-Mn-C alloys show that the main parameters of the process such as temperature, blowing method, gas composition, and bath depth are similar for both cases. In these chapters, the authors reviewed fundamental kinetic and thermodynamic studies relevant to AOD processing and in particular compared kinetic studies on AOD refining of Fe-Cr-C alloys to those for the Fe-Mn-C system. Whilst there is a substantial body of literature on the iron-carbon-chromium system there is not a large body of work on the iron-carbon-manganese system. Fe-Cr-C thermodynamic studies show a clearly delineated critical point which defines the boundary between conditions where chromium is oxidized and those where carbon is oxidized. Although the critical point is less evident in kinetic studies, it still has a clear influence, and injection into deep metal baths tends to dominate refining. In the case of the Fe-Mn-C system, thermodynamics predicts a critical point but it does not appear to play as significant a role as in the chromium-based system. In addition, AOD refining of

manganese alloys has the potential of much higher losses because of the contribution from manganese vapor.

Previous researchers have shown that manganese loss by evaporation at elevated temperatures has made the refining of ferromanganese more challenging than stainless steel. In the current study, the focus has been on quantifying the oxidation and evaporation-related losses during Ar-O_2 bubbling into high manganese steels and determining the factors affecting them.

Chapter 3 addresses the role of initial carbon and manganese concentrations on the rate of decarburization and manganese losses. This chapter presents a model to explain the mechanisms of manganese losses.

Chapter 4 addresses the effect of total gas flow rate and gas composition on the decarburization and manganese losses. This chapter illustrates the effect of using higher carbon content on the manganese loss, compared with chapter 3. Chapter 4 also presents an approach to find the ratio of mass transfer coefficients of Mn to C.

Chapter 5 contributes an understanding of the effects of temperature and nozzle submergence depth on the kinetics of decarburization and manganese losses. This chapter also applies the mechanism proposed in chapter 3 to explain the manganese losses.

6.1 Key Findings and Contributions

Experimental measurements and kinetic and thermodynamic analysis have been conducted on decarburization and demanganization of Fe-Mn-C alloys during Ar-O_2 bubbling. The important findings are as follow:

1. Chapter 3 demonstrates the achievement of the first objective presented in Chapter 1. The overall rate of manganese loss was controlled by a complex combination of mechanisms.

    a) It was shown that manganese loss increased with lower C and higher Mn content in the alloy which, taken collectively with other observations in this work, is most likely due to the faster transport of Mn to the bubble surface creating a preference for MnO formation over CO.

    b) Due to the competition between carbon and manganese for oxygen, the observed rate of decarburization varied with the initial manganese concentration. This finding was contrary to thermodynamic predictions for Fe-Mn-C alloys (conducted in Chapters 4 and 5) which supports the importance of a kinetically controlled competition between manganese and carbon for oxygen.

    c) Despite evidence that reactions occurred extremely rapidly the gas bubbles did not reach complete equilibrium with the melt. In

addition, the detailed results did not support the critical carbon concept. These observations support the importance of competition between decarburization and demanganization, most likely governed by the relative rates of carbon and manganese transport in the melt.

d) The manganese loss as vapor in experiments was much higher than the prediction by thermodynamics. This was likely due to increased temperature as a result of exothermic reactions.

2. In Chapter 3, the available oxygen was not sufficient to support the observed decarburization and manganese loss entirely by oxidation. This finding was consistent with the reported literature for the oxygen refining of high carbon ferromanganese, where manganese losses were attributed to evaporation and oxidation. However, in this work, for the extra manganese loss to be supported by evaporation seems unlikely because the local temperature rise at the bubble surface would need to be at least 350 K.

    a) An evaporation-condensation mechanism was proposed to explain the loss in addition to loss as MnO and Mn (g). The local temperature rise at the surface of the bubble due to the exothermic reactions of MnO and CO formation, facilitated the evaporation of manganese at higher vapor pressure, followed by condensation to fine droplets at the lower temperature inside the bubble. This mechanism requires a

temperature difference of at least 200 K between the bubble surface and interior.

b) This mechanism was supported both thermodynamically and kinetically, while it seems more likely than simple evaporation the latter mechanism cannot be entirely discounted. It has been shown that the heat generated from exothermic reactions can heat up a layer immediately adjacent to the surface of the bubble from 0.27 to 0.64 microns in thickness, which would contain sufficient Mn at a higher temperature to transfer to the interior of the bubble at lower temperature and justify the extra Mn loss. Furthermore, the calculated mass transfer coefficients for manganese in the gas phase (192 cm/s) based on a simple assumption is in the range of literature values. It is also noteworthy that higher levels of MnO formation resulted in higher losses as vapor and mist which is to be expected from the much greater heat formation of MnO compared with CO.

3. Chapter 4 demonstrates the achievement of the second objective presented in Chapter 1. The overall rates of reactions were controlled by the oxygen supply rate. However, the competition between Mn and C was controlled by their mass transport in the liquid metal.

    - It was shown that dilution of oxygen with argon increased the efficiency of oxygen for decarburization which is consistent with the

accepted mechanism behind AOD refining. However, the thermodynamically predicted cessation of manganese loss at higher levels of argon dilution did not occur. Therefore, the bubble and melt do not come into complete thermodynamic equilibrium with respect to Mn and C which is consistent with the results from Chapter 3 where no specific critical carbon content was observed.

4. In Chapter 4, unlike the results in Chapter 3, after accounting for CO and MnO formation there was excess oxygen. For this reason, manganese loss by evaporation was assumed to be negligible.

    a) Based on mass balance and thermodynamic calculations, it was shown that oxygen was distributed amongst MnO, FeO, CO, and CO_2 the proportions in which the distribution occurred were calculated in Chapter 4.
    b) Using an approach where carbon and manganese oxidation occurred in proportion to the mass transfer rates of the species in the melt, the ratio of mass transfer coefficients of Mn/C were estimated. By applying these mass transfer coefficient ratios and assuming the mass transfer coefficient of carbon is 0.035 cm/s, the reaction time for decarburization or demanganization is estimated to 0.001 sec. This shows that reactions were sufficiently fast that they only occurred over a small fraction of the bubble's life. However, given

the rapid kinetics, one might expect that the contents of each bubble would approach equilibrium with the melt over the remainder of the bubble lifetime, however, this did not occur. The author does not have a definitive explanation for this observation.

5. In Chapter 4, for the 1% C alloy, Mn loss occurred almost entirely as MnO dust rather than as a combination of MnO and mechanisms involving vapor as seen in Chapter 3 for lower carbon alloys. The absence of evaporation-related mechanisms appears to be related to the higher carbon content decreasing the amount of MnO formed thereby decreasing the heat generated and therefore decreasing the amount of vapor that could be produced
6. Chapter 5 coincides with objective 3. The likely mechanisms of manganese loss are oxide formation, vapor formation, and evaporation-condensation, similar to Chapter 3.
    a) It was demonstrated that increasing temperature led to the higher manganese loss as a mist and by simple vaporization due to the increased vapor pressure and less manganese loss by oxidation.
    b) It was found that the rate of decarburization increased with increasing temperature because of more partitioning of oxygen to carbon than manganese.
    c) Comparison of thermodynamic calculations with experimental observations showed that manganese and carbon in the bubble do

not equilibrate with the melt. This finding agreed with observations from Chapters 3 and 4.

7. In Chapter 5, the amount of fume generated increased with the initial manganese content of the alloy because of the increase in the vapor pressure of manganese and the faster transport of Mn in the melt. This observation was in agreement with the reported laboratory work in the literature for processing of high manganese steels under vacuum.

    a) The measured ratio of Mn/Fe concentration in fume increased with increasing initial manganese and decreasing carbon contents of the alloy and decreasing temperature.
    b) The qualitative trend of the measured ratio of Mn/Fe in the fume was consistent with the trend of equilibrium pressures of Mn/Fe. However, from experimental data, the quantitative Mn/Fe ratios were lower than predicted by vapor pressures. The slopes of lines for Mn/Fe in fume versus initial manganese content were almost identical for all alloy compositions which would be consistent with a controlling role for mass transport of Mn in the metal. Furthermore, the rates increased with decreasing initial carbon content which would suggest competition for oxygen between manganese and carbon.

8. Results from Chapter 5 demonstrate that the variations of depth of lance submergence did not make any changes to the rate of decarburization or demanganization. Whilst this observation is consistent with the idea that relative rates of manganese and carbon loss are driven by their relative transport kinetics, rather than which is most thermodynamically favorable, it leaves some doubt regarding why reactions that could occur in a fraction of the lifetime of a bubble, could not revert to equilibrium over the remainder of the bubble lifetime. The author is not able to offer a definitive explanation for this apparent discrepancy, however, it seems that manganese oxide fume need not be in contact with the bubble surface and therefore would not be readily available for reduction back into the melt.

6.2 Future work

In the current work, the decarburization occurred as it was expected based on the argon dilution effect in the AOD process. However, manganese did not follow the pattern expected from thermodynamics. At one level this observation is consistent with behavior observed for chromium oxidation, in that over short bubble residence times the competition for oxygen tended to be controlled by the relative rates of transport in the metal. However, changes to the residence time of bubbles made no difference to the relative manganese and carbon loss. The author has proposed a mechanism where the MnO was in a form that was not readily accessible to the surface of the bubble and could therefore not be reduced back into the melt by carbon. Despite attempts to test this hypothesis by changing the immersion depth of the nozzle, the bath was too shallow to claim definitively that MnO did not behave

in the same way as chromium oxide in AOD converters. It would be worthwhile conducting additional experiments in a significantly deeper bath to assess the manganese reversion into the melt.

The evaporation-condensation mechanism proposed to explain the extra manganese losses, could not be fully verified because of the difficulty in measuring the localized bubble surface temperature it would be worthwhile trying to devise an experiment where the surface temperature could be measured for sample by jetting on to the top surface of the melt. Therefore, this is not a definitive answer to the manganese loss.

The middle stage of manganese loss is not well understood although it is observed consistently across several studies. What makes the demanganization reaction ceased why it starts again is not at all clear. One possibility is a change in melt temperature with time. The author's measurements of the outer wall of the crucible detected no significant temperature increase but extremely careful monitoring of the melt temperature directly may yield more definitive results.

A topic of further interest, which was not addressed in the current work is the effect of slag on manganese loss. Therefore, it would be worth running a number of the experiments presented in the current work in the presence of synthetic slag and also bubbling only argon to study the gas/bubble/metal reaction.

7 References

1 R. Elliott, K. Coley, S. Mostaghel, and M. Barati: *JOM*, 2018, vol. 70, pp. 680–90.

2 B.C. De Cooman, O. Kwon, and K.G. Chin: *Mater. Sci. Technol.*, 2012, vol. 28, pp. 513–27.

3 O. Bouaziz, H. Zurob, B. Chehab, J.D. Embury, S. Allain, and M. Huang: *Mater. Sci. Technol.*, 2011, vol. 27, pp. 707–9.

4 Z.H. Cai, H. Ding, X. Xue, J. Jiang, Q.B. Xin, and R.D.K. Misra: *Scr. Mater.*, 2013, vol. 68, pp. 865–8.

5 H. Aydin, E. Essadiqi, I.H. Jung, and S. Yue: *Mater. Sci. Eng. A*, 2013, vol. 564, pp. 501–8.

6 O. Bouaziz, S. Allain, C.P. Scott, P. Cugy, and D. Barbier: *Curr. Opin. Solid State Mater. Sci.*, 2011, vol. 15, pp. 141–68.

7 A. Grajcar, R. Kuziak, and W. Zalecki: *Arch. Civ. Mech. Eng.*, 2012, vol. 12, pp. 334–41.

8 B. C. De Cooman, K. Chin, and J. Kim: in *New Trends and Developments in Automotive System Engineering*, 2011, pp. 101–28.

9 M. Kuzmina, D. Ponge, and D. Raabe: *Acta Mater.*, 2015, vol. 86, pp. 182–92.

10 K. Radwański, A. Wrozyna, and R. Kuziak: *Mater. Sci. Eng. A*, 2015, vol. 639, pp. 567–74.

11 C. F. Redeker, H.-J. Renner, and J. Schöttler: *Cost Efficient Metallurgy for the Production of Novel Ultra-High Strength Deep Drawable Steel Grades with High Mn Contents from 10 to 25 Wt.-%*, Luxembourg, 2008.

12 T. Germershausen, J. Bader, J. Reichel, U. Gerike, and S.M.S.S. Ag: in *The thirteenth International Ferroalloys Congress Efficient technologies in ferroalloy industry*, Almaty, Kazakhstan, 2013, pp. 335–46.

13 W.A. Krivsky: *Metall. Trans.*, 1973, vol. 4, pp. 1439–47.

14 S. Seetharaman, A. Mclean, R.I.L. Guthrie, and S. Seetharaman: *Treatise on Process Metallurgy, Vol.2: Process Phenomena*, vol. 2, 2014.

15 G.J.W. Kor, T. Timken, and C. Retired: The AISE Steel Foundation, Pittsburgh, PA, 1998, pp. 661–713.

16 R.J. Fruehan: *The Making, Shaping and Treating of Steel*, The AISE Steel Foundation, 1998.

17 R. Figueira and J. Szekely: *Metall. Trans. B*, 1985, vol. 16B, pp. 67–75.

18 I. Andersson, A. Tilliander, L.T.I. Jonsson, and P.G. Jo: 2013, vol. 40, pp. 551–8.

19 B. Deo and V. Srivastava: *Mater. Manuf. Process.*, 2003, vol. 18, pp. 401–8.

20 C. Schade and R. Causton: *Adv. POWDER Metall. Part. Mater. 2*, 2003, vol. 2, pp. 1–13.

21 C. Spinolal, C. Galvez-femaindezl, J. Mufjoz-perez, J. Jerrer, J.M. Bonelo, and J.

Vizoso: in *ndustrial Technology, ICIT ,IEEE International Conference on.*, vol. 4, 2006, pp. 1794–9.

22 V.-V. Visuri, M. Järvinen, A. Kärnä, P. Sulasalmi, E.-P. Heikkinen, P. Kupari, and T. Fabritius: *Metall. Mater. Trans. B*, 2017, vol. 48, pp. 1850–67.

23 J.-H. Wei, H.-L. Zhu, G.-M. Shi, J.-H. Shu, Q.-Y. Jiang, and H.-B. Chi: *Steel Res. Int.*, 2007, vol. 78, pp. 305–10.

24 J. Wei and D. Zhu: *Metall. Mater. Trans. B*, 2002, vol. 33, pp. 111–9.

25 C. Wuppermann, A. Rückert, H. Pfeifer, and H.J. Odenthal: *ISIJ Int.*, 2013, vol. 53, pp. 441–9.

26 R.J. Fruehan: *Met. Trans. B*, 1975, vol. 6, pp. 573–8.

27 E.-P. Heikkinen and T. Fabritius: *Recent Res. Metall. Eng. Extr. to Forming. InTech*, 2012, vol. 186, pp. 65–88.

28 A. Ghosh: *Secondary Steelmaking Principles and Applications*, CRC Press LLC, 2001.

29 E.T. Turkdogan: *Fundamentals Of Steelmaking*, Institute of Materials, London, 2010.

30 M. Järvinen, V. Visuri, E. Heikkinen, A. Kärnä, and P. Sulasalmi: *ISIJ Int.*, 2016, vol. 241, pp. 1–10.

31 R.J. Fruehan: *Ironmak. Steelmak.*, 1976, vol. 3, pp. 153–8.

32 E.T. Turkdogan: *Can. Metall. Q.*, 2001, vol. 40, pp. 255–307.

33 S. Seetharaman: *Treatise on Process Metallurgy, Vol.3: Industrial Processes*, vol. 3, 1st edn., Elsevier, 2014.

34 F.D. Richardson and W.E. Dennis: *J. Iron Steel Inst.*, 1953, vol. 175, pp. 257–63.

35 V. Visuri, M. Jarvinen, P. Sulasalmi, E. Heikkinen, P. Kupari, and T. Fabritius: *Metall. Mater. Trans. B*, 2017, vol. 48B, pp. 1868–84.

36 M. Jarvinen, S. Pisila, A. Karna, T. Ikaheimonen, P. Kupari, and T. Fabritius: *Steel Res. Int.*, 2011, vol. 82, pp. 638–49.

37 T. Fabritius, P. Kurkinen, P. Mure, and J. Ha: *Ironmak. Steelmak.*, 2005, vol. 32, pp. 113–9.

38 K.J. Barker, A.H. Chan, R.J. Choulet, and B. V. Patil: *The Making, Shaping and Treating of Steel, Steelmaking and Refining Volume*, The AISE Steel Foundation, Pittsburgh, PA, 1998.

39 H.S. Song, S.M. Byun, D. Min, S.K. Yoont, and S.Y. Ahnt: in *Proceedings of the 1st International Chromium Steel and Alloys Congress*, vol. 2, Johannesburg, 1992, pp. 89–96.

40 D.R. Swinbourne, T.S. Kho, B. Blanpain, S. Arnout, and D.E. Langberg: *Miner. Process. Extr. Metall.*, 2012, vol. 121, pp. 23–31.

41 R.I.L. Guthrie, M. Isac, and Z. Lin: *Ironmak. Steelmak.*, 2005, vol. 32, pp. 465–72.

42 V. Visuri, M. Järvinen, J. Savolainen, P. Sulasalmi, E. Heikkinen, and T. Fabritius: *ISIJ Int.*, 2013, vol. 53, pp. 613–21.

43 E.B. Pretorius and R.C. Nunnington: *Ironmak. Steelmak.*, 2002, vol. 29, pp. 133–9.

44 Lyall Franklin Barnhardt: Doctoral Thesis, Massachusette Institute of Technology, 1965.

45 G.W. Healy and and D.C. Hilty.: *J. Met.*, 1957, vol. 9, pp. 695–707.

46 P.T. Jones: Doctoral Thesis, Katholieke Universiteit Leuven, 2001.

47 J.H. Park, I. Jung, and S. Lee: *Met. Mater. Int.*, 2009, vol. 15, pp. 677–81.

48 R.J. Fruehan: *Ironmak. Steelmak.*, 1976, vol. 3, pp. 33–7.

49 Y. Niiri, K. Ito, and K. Sano: *Tetsu-to-Hagane*, 1969, vol. 55, pp. 437–45.

50 T. Ohno and T. Nishida: *Tetsu-to-Hagane*, 1977, vol. 63, pp. 2094–9.

51 J.M. Saccomano, R.J. Choulet, and J.D. Ellis: *J. Met.*, 1969, vol. 21, pp. 59–64.

52 Y. Kobayashi and S. Maruhashi: *Tetsu-to-Hagané*, 1977, vol. 63, pp. 2100–9.

53 R. Tsujino, K. Kato, S. Kitamura, H. Morishige, R. Nakao, R. Hisatomi, H. Takano, and H. Hirata: *Advances in Stainless Steelmaking Technology*, 1994.

54 L.B. Pankratz: *Thermodynamic Propertiesof Elements and Oxides*, US Bureau of Mines Bulletin 672, US Dept. of Interior, 1982.

55 S.E. Olsen, M. Tangstad, and T. Lindstad: *Production of Manganese Ferroalloys*,

Tapir academic press, Trondheim, 2007.

56 D.S. Kozak and L.R. Matricardi.: *Iron Steelmak.*, 1981, vol. 8, pp. 28–31.

57 W. Dresler: *Can. Metall. Q.*, 1989, vol. 28, pp. 109–15.

58 W. Huang: *Metall. Trans. A*, 1990, vol. 21, pp. 2115–23.

59 D. Djurovic, B. Hallstedt, J. Von Appen, and R. Dronskowski: *Calphad Comput. Coupling Phase Diagrams Thermochem.*, 2011, vol. 35, pp. 479–91.

60 M.S. Kim and Y.B. Kang: *J. Phase Equilibria Diffus.*, 2015, vol. 36, pp. 453–70.

61 Y.E. Lee: *Metall. Mater. Trans. B*, 1998, vol. 29, pp. 397–403.

62 V.H. Schenck and F. Neumann: *Arch. für das Eisenhüttenwes.*, 1958, vol. 86, p. 1958.

63 Y.E. Lee and J.H. Downing: *Can. Metall. Q.*, 1980, vol. 19, pp. 315–22.

64 W. Dresler: in *Steelmaking Conference Proceedings*, 1989, pp. 13–20.

65 G.W. Healy: *Iron Steelmak.*, 1987, vol. 14, pp. 51–9.

66 G. Sigworth and J.F. Elliott: *Met. Sci.*, 1974, vol. 8, pp. 298–310.

67 H. R, Desai PD, and W.D. Hawkings DT, Gleiser M, Kelley KK: *Natl. Stand. Ref. Data Syst.*

68 J. Chipman: *AIME MET SOC TRANS*, 1967, vol. 239, pp. 1332–6.

69 R. Ni, Z. Ma, and S. Wei: *Steel Res.*, 1990, vol. 61, pp. 113–6.

70 H. Enokido, A. Moro-Oka, and E. Ichise: *Tetsu-to-Hagane*, 1995, vol. 81, pp. 619–24.

71 M. Tangstad: *Manganese Ferroalloys Technology*, Elsevier, Trondheim, 2013.

72 B. You, J. Han, and J. Pak: *Steel Res.*, 2000, vol. 71, pp. 22–6.

73 B.-D. You, K.-Y. Park, J.-J. Pak, and J.-W. Han: *Met. Mater.*, 1999, vol. 5, pp. 395–9.

74 B.-D. You, B.-W. Lee, and J.-J. Pak: *Met. Mater.*, 1999, vol. 5, pp. 497–502.

75 B.-D. You: *J. Korean Institue Met. Mater.*, 1995, vol. 33, pp. 1508–13.

76 K. Yamamoto, T. Mimura, S. Ito, and T. Onoye: *Tetsu-to-Hagane*, 1986, vol. 72, pp. 1034–46.

77 Y.E. Lee and L. Kolbeinsen: *ISIJ Int.*, 2005, vol. 45, pp. 1282–90.

78 B. Deo and R. Boom: *Fundamentals of Steelmaking Metallurgy*, Prentice Hall International Limited, UK, 1993.

79 N.A. Molloy: *J. iron steel Inst.*, 1970, vol. 208, p. 943.

80 M. Lee, V. Whitney, and N. Molloy: *Scand. J. Metall.*, 2001, vol. 30, pp. 330–6.

81 M. Alam, J. Naser, G. Brooks, and A. Fontana: *ISIJ Int.*, 2012, vol. 52, pp. 1026–35.

82 E.T. Turkdogan, P. Grieveson, and L.S. Darken: *J. Am. Chem. Soc.*, 1963, vol. 67, pp. 1647–54.

83 J. Nell and I. Nolet: in *The Twelfth International Ferroalloys Congress Sustainable Future*, Helsinki, Finland, 2010, pp. 579–88.

84 H. Liu, J. Liu, J. Schenk, F.M. Penz, L. Sun, R. Zhang, and Z. An: *Metall. Mater. Trans. B*, 2020, vol. 51, pp. 756–62.

85 J.-H. Wei and D.-P. Zhu: *Metall. Mater. Trans. B*, 2002, vol. 33, pp. 111–9.

86 J. Wei and D. Zhu: *Metall. Mater. Trans. B*, 2002, vol. 33B, pp. 121–7.

87 O. Velychko, D. Yunshen, Y. Mianovska, L. Kamkina, R. Ankuninov, О.Г. Величко, Д. Юньшен, Я.В. Мяновська, Л.В. Камкіна, and Р.В. Анкудінов: 2020, pp. 30–5.

End